Doctoral dissertation
(博士学位論文)

Crystallization Kinetics of Amorphous Silicate and Alumina Dust in Protoplanetary Disks

(原始惑星系円盤における非晶質ケイ酸塩およびアルミナダストの結晶化速度論)

Presented by
Kodai Kobayashi
(小林　航大)

Department of Natural History Sciences
Graduate School of Science
Hokkaido University
(北海道大学大学院理学院
自然史科学専攻)

March, 2023
(令和 5 年 3 月)

Contents

Abstract

Infrared spectroscopic observations and laboratory experiments of dust analogues have indicated that crystalline/amorphous silicates, amorphous/transition alumina (Al_2O_3), and a relatively small amount of corundum are present around oxygen-rich AGB stars (Waters et al., 1996; Takigawa et al., 2015, 2019). In the diffuse interstellar medium, silicate dust is considered to be almost amorphous (Kemper et al., 2004) while both crystalline and amorphous silicates are dominant in protoplanetary disks (Bouwman et al., 2001). On the other hand, alumina grains found in primitive chondrites consist of abundant corundum and a small amount of amorphous/transition alumina (e.g., Nittler et al., 2008) although it is necessary to carefully consider that amorphous and transition alumina grains are readily dissolved during acid treatments of meteorites (Takigawa et al., 2014). These astronomical observations and mineralogical evidences of silicate and alumina grains in chondrites imply that amorphous silicate and amorphous/transition alumina dusts would transform into crystalline dusts through thermal processes in protoplanetary disks. More detailed observations for disks around young stars have shown that more abundant crystalline silicate exists in the inner warm regions (van Boekel et al., 2004), and relative abundance of enstatite to forsterite decreases with distance from stars (Bouwman et al., 2008). Therefore, the distributions of crystallinity and dominant phases for silicate and alumina dusts could reflect on physical conditions such as temperatures and ambient gas pressures in the disks. These physical conditions for the thermal evolution in the disks would contribute to an understanding of material evolutions for planetary formation in the early solar system.

Crystallization of amorphous silicates has been investigated experimentally to understand the dust evolution in protoplanetary disks (e.g., Brucato et al., 2002). It has been shown that crystallization of amorphous forsterite (Mg_2SiO_4) is promoted by water vapor which could be present in the disks (Yamamoto & Tachibana, 2018), but the effect of ambient gas atmosphere (e.g., H_2, H_2O, and their pressures) on crystallization of amorphous enstatite ($MgSiO_3$), which has the Mg/Si ratio close to the solar ratio, has not yet been fully understood. Some phase transition experiments from transition alumina (γ-alumina) to α-alumina have been also discussed in a field of ceramic science (e.g., Wilson & Mc Connell, 1980), however, the activation energy and transition rate for γ-α transformation have taken different values (~200–600 kJ/mol; e.g., McArdle & Messing, 1993), and crystallization kinetics of amorphous alumina have not yet been almost performed. In this thesis, I conducted crystallization experiments of

amorphous enstatite under various ambient gas pressures and crystallization/phase transition experiments of alumina dusts to obtain kinetic data of silicate and alumina dusts for thermal annealing in protoplanetary disks.

The activation energy for crystallization of amorphous enstatite was determined to be ranged from 727 (in air) to 951 kJ/mol (in vacuum), and the presence of water vapor decreased the activation energy as in the case of crystallization of amorphous forsterite (Yamamoto & Tachibana, 2018). The crystallization rate became large with decreasing total pressures, and crystallization at P_{H2O} of 0.3 Pa occurred the fastest at the all ambient gas conditions. Thus, the ambient gas pressure has influence on crystallization of amorphous enstatite at the experimental temperature range, however, its effect remains minimal in protoplanetary disks due to very high activation energy for crystallization of amorphous enstatite. Therefore, crystalline enstatite dust could be a good thermo-recorder at the temperature above ~950–1000 K in the inner regions of evolving disks. Because crystallization of amorphous forsterite under various water vapor pressures occurs at the temperature above ~700–850 K (Yamamoto & Tachibana, 2018), the dust distribution of crystalline enstatite and forsterite through thermal annealing could cause the decrease of relative abundance of enstatite to forsterite with lager radii of disks. (Bouwman et al., 2008).

The phase transition from amorphous alumina into α-alumina occurred through transition alumina (γ-alumina) as reported in previous studies (e.g., Yamaguchi et al., 1976). The activation energies for crystallization of amorphous alumina and γ-α phase transition were estimated to be 314 and 427 kJ/mol, respectively. Crystallization and phase transition temperatures of alumina dusts in accretion disks indicate that amorphous alumina and γ-alumina could widely survive at the temperatures below ~750–850 K and at the temperature range of 850–1000 K, respectively, which could support the possible presence of the acid-soluble alumina phase in pristine chondrites (Takigawa et al., 2014). In comparison to oxygen isotopic exchanges of alumina grains derived from oxygen diffusion data (Nabatame et al., 2003), it was also found that presolar amorphous and γ-alumina dust incorporated in the disks would almost transform into γ-alumina and α-alumina, respectively, subsequently to their oxygen isotopic exchanges. This could support that much more solar corundum has been observed than presolar corundum in primitive chondrites (e.g., Takigawa et al., 2014). On the other hand, presolar α-alumina could survive at temperatures above ~1100 K and at certain regions where α-viscosity is close to $\sim 10^{-2}$, which might correspond to a small amount of presolar corundum grains observed in chondrites (e.g., Stroud et al., 2004; Nittler et al., 2008).

1
General Introduction

Silicate dust is the most dominant solid dust in the Galaxy. Refractory oxide dust is less abundant than silicate dust, but could have recorded high-temperature dust forming processes. These dusts are freshly formed by condensation of SiO and AlO gases around evolved stars such as asymptotic branch giant (AGB) stars (Takigawa et al., 2017), which are major sources of various oxide dusts in the interstellar medium because they experience mass loss at very high rates and their envelopes are extremely cool (Dell'Agli et al., 2014). Presolar silicate and oxide grains observed in chondrites are mainly originated from AGB stars and Supernovae (e.g., Choi et al., 1998, Nittler et al., 2008, Nguyen et al., 2010, Leitner et al., 2012a), indicating direct evidence of the formation of these dusts around the evolved stars.

Infrared spectroscopic observations of oxygen-rich evolved stars have shown broad features at 10 and 18 μm which are attributed to amorphous silicates, and narrow features at the range of 10–70 μm originating from crystalline olivine and pyroxene (e.g., Waters et al., 1996). On the other hand, infrared dust emissions with a broad feature with its peak at ~11–12 μm and a relatively sharp peak at ~13 μm (Fig. 1.1) have been observed around some oxygen-rich AGB stars. These dust emissions are not explained by silicate dusts, and amorphous alumina or transition alumina as γ-alumina can be plausible candidates for the former emission, while corundum (α-alumina) explains the latter sharp emission (Sloan et al., 2003; Takigawa et al., 2015, 2019). Such alumina-rich evolved stars are not rare in spite of lesser abundance of Al than Si (solar Al/Si ratio of 0.08; Lodders 2003). A recent ALMA observation has shown that alumina dusts are formed at the regions close to the stellar surface, and their effective formation and growth accelerates the mass loss wind at temperatures higher than silicate dust condensation, which results in less effective formation of silicate dust (Takigawa et al., 2017).

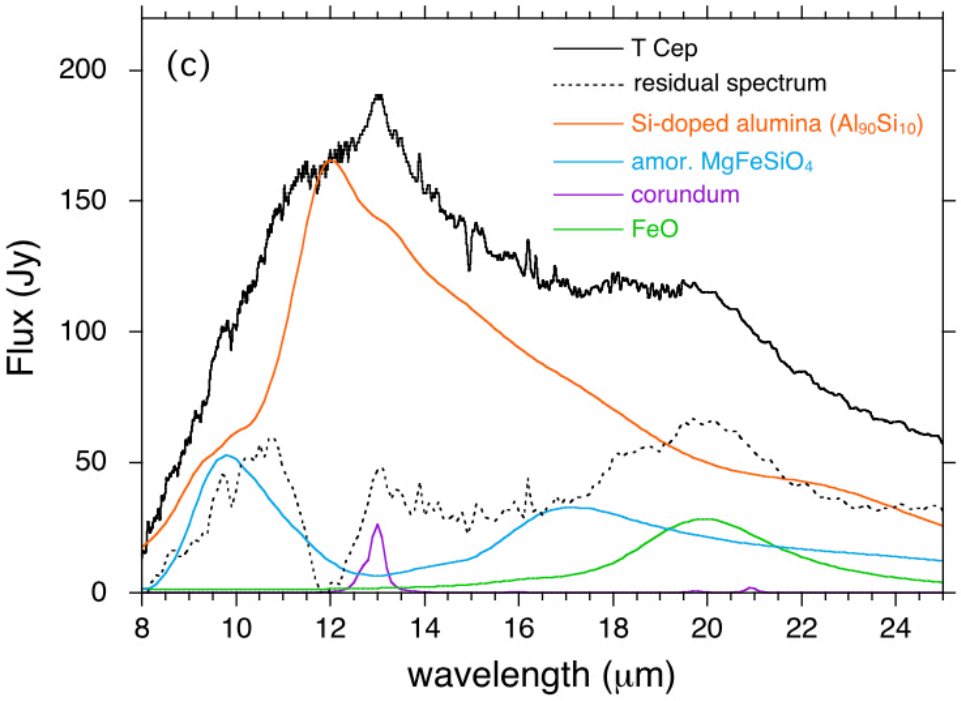

Fig. 1.1 Comparison of the spectrum of T Cep (black line) with the calculated absorption coefficient of the transition alumina containing ~10 % of Si (orange line) obtained from condensation experiments in vacuum (Takigawa et al., 2019) and the spectra for amorphous $MgFeSiO_4$ (blue line; Dorschner et al., 1995), corundum (purple line; Takigawa et al., 2015), and FeO (green line; Henning et al., 1995). This Figure taken from Takigawa et al. (2019).

In the interstellar medium (ISM), silicate dust is present in an almost amorphous state because the interstellar absorption band shows a broad and smooth feature at 10 μm and is well reproduced by those of amorphous silicates (Kemper et al., 2004). Even though crystalline silicate dust is ejected from evolved stars, they are likely to be destructed by supernova explosion shock waves and/or by irradiation of cosmic rays (e.g., Demyk et al., 2001).

In protoplanetary disks, both amorphous and crystalline silicates are observed from infrared spectra of the inner and outer disk region (van Boekel et al., 2004), and the fraction of crystalline silicate to amorphous silicate is higher in the inner part of disks (1–2 au) than in the outer regions (2–20 au). The dust emissions of crystalline silicate show that both enstatite and forsterite are present in the inner warm disks (~1 au) while forsterite is dominant in outer cold regions (5–15 au) (Bouwman et al., 2008). Such spatial distributions of crystalline silicate dust indicate the contribution of thermal annealing of interstellar amorphous silicate dusts in protoplanetary disks (e.g., Henning, 2010).

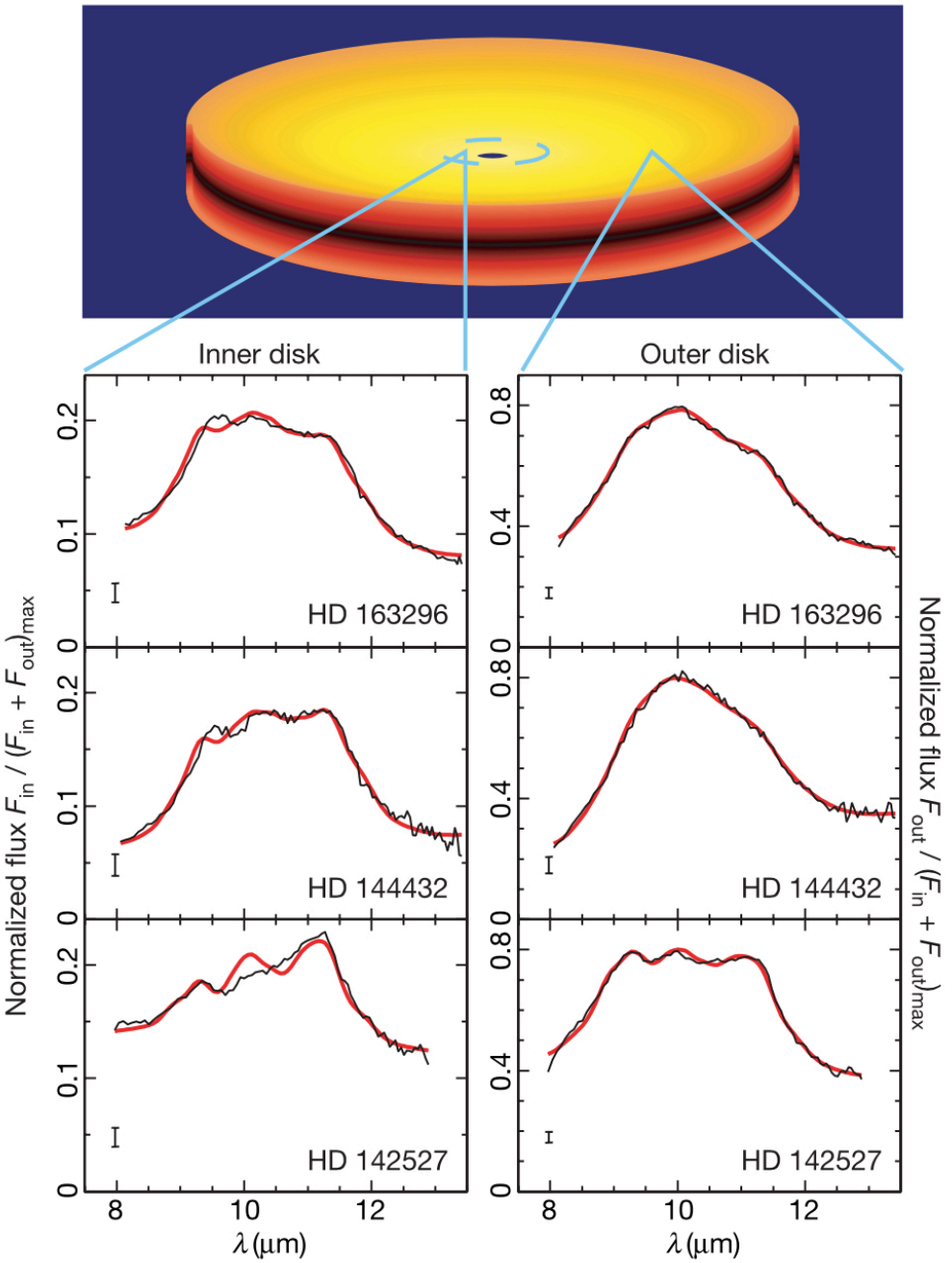

Fig. 1.2 Infrared spectra of the inner (1–2 au) and outer (2–20 au) disk regions of three Herbig Ae stars (Black lines). Also shown are the best-fit model spectra for the inner- and outer-disk regions (red lines) derived from the laboratory spectra of crystalline olivine and pyroxene (Chihara et al., 2001), a laboratory spectrum of an IDP consisting of hydrated silicates (Sandford & Walker, 1985), and the interstellar medium silicate spectrum (Kemper et al., 2004). The regions that dominate the inner- and outer-disk spectra are indicated in the schematic representation of a protoplanetary disk at the top of the figure. This Figure taken from van Boekel et al. (2004).

Silicate and alumina dust candidates, once presented in the early solar system, have been identified in extraterrestrial materials. The matrices of chondrites, undifferentiated meteorites, are mainly composed of both amorphous and crystalline silicates with metallic Fe, Ni, sulfides (Scotto, 2007). Fine-grained amorphous silicate particles with a typical size of 10 nm–5 μm is preserved in the matrix of pristine chondrites (Abreu & Brearley, 2010). Micrometer-sized grains of presolar corundum (α-Al_2O_3) is also found in primitive chondrite matrices (Nittler et al., 1997; Choi et al., 1998). Although small quantities of amorphous and transition alumina are observed in primitive meteorites (Stroud et al., 2004; Takigawa et al., 2014), both presolar and solar alumina grains found in chondrites are corundum (α-alumina) in most cases. The abundances of presolar silicate (~100–200 ppm; Floss & Haenecour, 2016) and alumina grains (~0.2–30 ppm; Nguyen et al., 2007) in primitive chondrites are much lower than solar grains with the same chemical compositions, which indicates that these presolar grains could be destructed through thermal processes in protoplanetary disks (Floss & Stadermann, 2012; Floss & Haenecour, 2016).

Because astronomical observations indicate that crystallization of amorphous dusts occurs through thermal annealing in protoplanetary disks as described above, these silicate and alumina grains within pristine chondrites should put constraints on the thermal evolution of dust in the early solar system. Many experimental studies on crystallization of amorphous silicate have already been investigated especially in the field of astronomy (e.g., Hallenbeck et al., 1998) to discuss the observed infrared features of crystalline silicates (e.g., Henning, 2010), However, there have been limited studies focusing on crystallization behaviors of amorphous silicate and alumina dust in protoplanetary disks except for the recent work by Yamamoto & Tachibana (2018), who discuss the effect of water vapor on crystallization of amorphous silicate with forsterite stoichiometry (Mg_2SiO_4). In this thesis, I focus on crystallization kinetics of amorphous silicate with enstatite stoichiometry ($MgSiO_3$) and amorphous alumina to discuss their crystallization processes in protoplanetary disks, with the aim of providing experimental data that can be compared with dust distributions of silicates obtained from infrared spectroscopic observations, and amorphous/crystalline silicate and alumina grains with origins of the extrasolar/solar system found in the matrices of pristine chondrites.

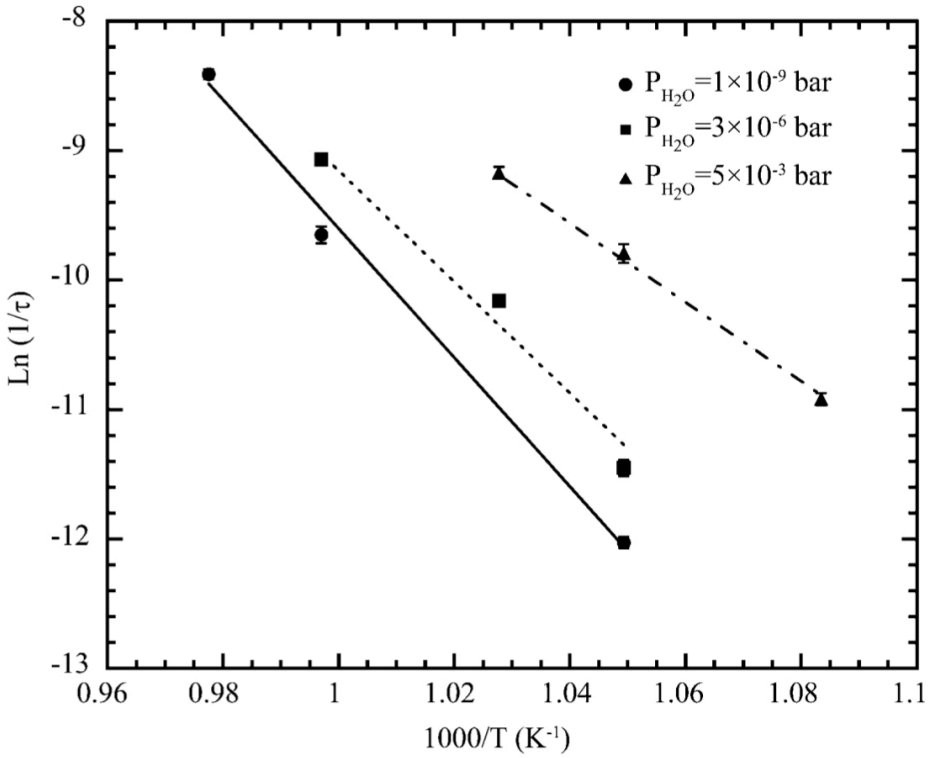

Fig. 1.3 Arrhenius plots of the reciprocal time constants ($1/\tau$) for crystallization of amorphous forsterite at P_{H2O} of 1×10^{-9}, 3×10^{-6}, and 5×10^{-3} bar. This Figure taken from Yamamoto & Tachibana (2018).

In Chapter 2, I describe crystallization experiments of amorphous silicate dust with enstatite composition (hereafter amorphous enstatite) under various atmospheres and discuss the effects of ambient gases on its crystallization kinetics and mechanisms. In Chapter 3, the results of crystallization from amorphous alumina dust and phase transition from γ-alumina to α-alumina dust are summarized. I discuss experimentally obtained kinetics for the crystallization and phase transition comparing with previous work in the field of ceramic science (e.g., Wilson & Mc Connell, 1980). In chapter 4, I apply the experimental results on amorphous enstatite and amorphous alumina to their crystallization in accreting protoplanetary disks and around evolved stars. I discuss a role of crystalline enstatite dust as a temperature sensor of protoplanetary disks and temperature distributions of alumina dusts in protoplanetary disks, which could help to understand thermal annealing processes in the circumstellar environments. Chapter 5 summarizes the thesis with future perspectives.

2
Crystallization Temperature of Amorphous Silicate Dust with Enstatite Composition as Thermo-Recorder of Protoplanetary Disks

2.1 Introduction

Silicate dust is one of the main constituents of protoplanetary disks, within which various physical and chemical processes lead to the formation of a variety of planetary systems. Both crystalline and amorphous silicate dust are present in protoplanetary disks. The former dust is detected in the inner warm parts of disks while amorphous dust is dominant in outer cold regions (van Boekel et al., 2004). Therefore, the crystalline silicate dust is likely to be a product of thermal annealing and accompanying crystallization of amorphous silicate dust which is a heritage from the interstellar medium (Kemper et al., 2004). It is also found that more enstatite is observed than forsterite in the inner regions of disks (Bouwman et al., 2008), which could help to understand temperatures in protoplanetary disks.

Murata et al. (2009) carried out crystallization experiments of amorphous magnesium silicate with Mg/Si ratio of 1.07, synthesized by the sol-gel method, to determine crystallization kinetics of amorphous silicate with the solar Mg/Si ratio in air at 1023–1073 K. They obtained the crystallization rate with the activation energy of 1.12×10^5 K. Because of its large activation energy for crystallization, they concluded that crystallization of amorphous magnesian silicate with the enstatite-like composition is kinetically inhibited in the outer part of protoplanetary disks, which is consistent with the observation of crystalline silicate dust (Bouwman et al., 2008). Imai (2012) performed similar crystallization experiments of amorphous magnesium silicate with enstatite composition, synthesized by the induction thermal plasma method (e.g., Kim et al., 2017; Takigawa et al., 2019; Matsuno et al., 2021) and obtained the activation energy of 8.6×10^4 K for crystallization in air at 1053–1123 K. Roskosz et al. (2011) found that forsterite dominantly crystallized from sol-gel synthesized amorphous silicate with enstatite composition below a glass transition temperature (~1040 K) determined for the synthesized enstatite glass. Considering the *Spitzer* observations that more enstatite is present in the inner region while forsterite dominates in the outer region, the mineralogical zoning observed in proroplanetary disks could reflect the sharp change for dominant crystalline phase from forsterite to enstatite through the glass transition temperature. Jäger et al. (2003) showed that the presence of hydroxyl group in amorphous structure significantly lowered the activation energy for crystallization. Yamamoto & Tachibana (2018) conducted crystallization experiments of amorphous forsterite in the presence of water

vapor and found that water vapor diffusing into amorphous structure promoted the crystallization of amorphous forsterite.

As I introduced previous studies above, because crystallization behavior of amorphous silicate depends on its structure, chemical composition, and ambient conditions, laboratory studies have shown different thermal evolutions of amorphous silicates and given hints for constraints on the disk conditions. Most previous experiments on crystallization of amorphous silicate have been conducted under 1 atmosphere or high vacuum pressures. Since hydrogen gas and water vapor are considered to be abundantly present in protoplanetary disks, it is necessary to investigate the effect of ambient disk gases on crystallization of amorphous silicate in protoplanetary disks. However, crystallization of amorphous silicates, except for amorphous forsterite, under disk conditions has not yet been fully understood. The aim of this section is to determine crystallization kinetics of amorphous enstatite under different ambient gases. I focused on the effect of disk gases (H_2O and H_2 gas) and total pressure on the crystallization, and considered that solar Mg/Si composition was almost 1.

2.2 Experiments

2.2.1 Annealing experiments

Sub-micron-sized amorphous silicate particles with enstatite ($MgSiO_3$) stoichiometry were used as a starting material, which were synthesized by an induced thermal plasma method and kindly provided by A. Tsuchiyama. The amorphous silicate particles with enstatite stoichiometry (hereafter amorphous enstatite) were found to be spherical in shape with a typical grain size of ~100 nm based on the field-emission scanning electron microscopy (FE-SEM), and measured with transmission electron microscopy (TEM) and X-ray powder diffraction (XRD) analyses as described below in detail. More detail characteristics of the starting material are given in the result section.

Annealing experiments were carried out under different ambient gas conditions; 1) in air, 2) in vacuum (~10^{-4} Pa), 3) in water vapor with pressure of 0.3 Pa, 4) in hydrogen gas with pressure of 5 Pa, 5) in a mixed H_2-H_2O gas ($H_2O/H_2 = 10^{-3}$) with pressure of 5 Pa, and 6) in very high water vapor pressure of 0.18 MPa. Because crystallization of amorphous enstatite has significantly large temperature dependence (i.e., large activation energy for crystallization) (Murata et al., 2009; Imai, 2012), the temperature in furnaces used in these experiments described below in details was carefully calibrated against NaCl and KBr to investigate the effect of ambient gas conditions on crystallization kinetics of amorphous enstatite.

A time series of annealing experiments in air (condition 1) was conducted at 1053–1123 K for 1–672 h (Table 2.1). I also conducted an annealing experiment in air at 993 K for 240h. This experimental condition is the same as that in Roskosz et al. (2011) for an amorphous silicate with enstatite composition synthesized by a sol-gel method. ~25 mg of amorphous enstatite powder, placed in a platinum dish, was annealed in an electric furnace (Thermolyne FB1314M). After heating for the desired duration, the sample was taken out from the furnace and rapidly cooled in air.

Annealing experiments at low pressures (conditions 2–5) were conducted for ~25 mg of the starting material in a platinum dish using a gold-mirror vacuum furnace (Thermo-Riko GFA430VN) equipped with a pumping system (HiCube 80 Eco, Pfeiffer Vacuum) and a gas supply line for H_2 and H_2-H_2O mixture (e.g., Yamamoto & Tachibana, 2018; Yamamoto et al., 2018, 2020). Irrespective of ambient gas conditions, the sample was heated up to a desired temperature for 30 min and kept at the temperature for a desired duration. The sample was then cooled down to room temperature in 30 min.

In the experiments in vacuum (condition 2), the sample was heated in a pressure range of (1–5) × 10^{-4} Pa, typically (2–3) × 10^{-4} Pa, without using a gas flow system. The heating temperature ranged from 1053 to 1093 K and heating duration from 1 to 228 h (Table 2.1). A dominant gas species in the furnace at ~10^{-4} Pa was found to be water vapor by gas analysis with a quadrupole mass spectrometer (MKS e-Vision+), which is consistent with the result reported by Yamamoto & Tachibana (2018). Annealing at the total pressure of (2–3) × 10^{-4} Pa thus corresponds to that under water vapor pressure (P_{H2O}) of (2–3) × 10^{-4} Pa.

For experiments at P_{H2O} of 0.3 Pa (condition 3), the water vapor was continuously supplied through the gas supply line from water ice kept at –20°C in the freezer (Yamamoto & Tachibana, 2018; Yamamoto et al., 2018, 2020, 2021, 2022). The furnace and the gas line were evacuated together with the pumping system down to (5–6) ×10^{-2} Pa, and the water vapor pressure was adjusted at 0.3 Pa prior to heating using a needle valve (that controls a flow rate of water vapor from water ice) and a butterfly valve attached to the pumping system (that controls an evacuation rate of water vapor). The water vapor pressure was kept constant at 0.3 Pa by a balance between gas flow and evacuation rates. The sample was heated at 1053–1093 K for 0.5–168 h under this condition (Table 2.1).

Experiments at hydrogen pressure (P_{H2}) of 5 Pa (condition 4) were conducted under continuous flow of hydrogen gas (99.99% purity) through the gas supply line. Hydrogen gas was supplied from a hydrogen gas cylinder and the flow rate was controlled by a needle valve. The

P_{H2} was adjusted by the balance between the gas flow and evacuation rates controlled by the butterfly valve. The hydrogen gas was introduced into the furnace at background pressure below ~10^{-4} Pa and the hydrogen gas pressure was adjusted at 5 Pa prior to heating. The sample was heated at 1073–1113 K for 0.5–72 h under this condition (Table 2.1).

For experiments at 5 Pa of H_2-H_2O gas mixture ($H_2O/H_2 = 10^{-3}$), deionized pure water in a one-sided silicate glass tube was put in a stainless-steel container. The stainless container was connected to a hydrogen gas flow line. Hydrogen gas (99.99% purity) was supplied through the stainless-steel container. Water in the container was frozen at –18°C in a freezer. The H_2O/H_2 ratio of 10^{-3} was determined by the ratios of a saturated water vapor pressure of 1.25×10^2 Pa at –18.0°C (Feistel & Wagner, 2007) and a supply pressure of hydrogen gas (1.25×10^5 Pa). The total pressure of 5 Pa in the furnace was kept constant by adjusting the gas supply and evacuation rates. Heating temperature ranged from 1073 to1113 K and duration from 0.5 to 48 h.

Annealing experiments were also conducted at P_{H2O} of 0.18 MPa (condition 6) to investigate the clear effect of water vapor pressure on the crystallization behavior of amorphous enstatite. The experiments were conducted in a closed system with sealed silica glass tubes (Kuroda et al., 2018; Kuroda & Tachibana, 2019). Amorphous enstatite powder of ~15 mg, put in a one-side silica glass tube (4 and 6 mm in inner and outer diameter), was placed inside a silica glass tube with its inner diameter of 8 mm, outer diameter of 10 mm, and length of ~11 mm. Deionized pure water, put in another one-sided inner silica glass tube (4 and 6 mm in inner and outer diameter), was also placed inside the outer silica glass tube as a water vapor source. The outer silica glass was sealed in vacuum to minimize the effect of atmospheric water vapor. Deionized pure water of ~2.2 μl at the experimental temperatures should produce and keep P_{H2O} of 0.18 MPa. The sealed silica glass tube was heated at 973 and 993 K for 3–336 h in an electric furnace (Thermolyne FB1314M). After heating, the glass tube was taken out from the furnace and cooled down to the room temperature in air.

Table 2.1 Crystallization degrees (x), parameters for intensity adjustment (y), crystallization time constants (τ) and the Avrami parameters (n) obtained from the fitting of infrared spectra and time evolution of the crystallization degrees. Errors represent 1σ standard error of the mean.

Ambient gas (Pa)	Temperature (K)	Duration (h)	x	y	τ (h)	n
Air (P_{H2O} ~10^2)	1123	1	0.363	1.00	1.39 ± 0.01	2.45 ± 0.09
		1.5	0.694	1.00		
		2	0.920	1.00		
		3	0.983	1.00		
		5	1.000	1.00		
	1093	3	0.199	1.00	8.89 ± 0.66	2.31 ± 0.57
		5	0.279	1.00		
		7	0.375	1.00		
		9	0.547	1.00		
		12	1.000	1.00		
		24	1.000	1.00		
		48	1.000	1.00		
	1073	6	0.000	1.00	26.09 ± 1.23	2.39 ± 0.34
		12	0.113	1.00		
		18	0.395	1.00		
		24	0.529	1.00		
		48	0.995	1.00		
		96	1.000	1.00		
	1053	120	0.057	1.00	296.11 ± 17.23	2.17± 0.35
		168	0.122	1.00		
		192	0.317	1.00		
		216	0.495	1.00		
		240	0.580	1.00		
		336	0.692	1.00		
		432	0.866	1.00		
		504	0.906	1.00		
		672	1.000	1.00		
Vacuum (P_{H2O} ~10^{-4})	1093	1	0.166	0.83	2.39 ± 0.23	1.52 ± 0.37
		2	0.646	0.72		
		3	0.678	0.84		
		6	1.000	0.92		
		12	1.000	1.01		
		24	1.000	1.00		
	1073	6	0.152	0.88	15.36 ± 0.63	2.57 ± 0.38
		12	0.363	0.88		
		18	0.808	0.92		
		24	0.953	0.96		
		36	1.000	1.00		
	1053	24	0.033	0.95	127.23 ± 1.89	2.65 ± 0.13
		48	0.072	0.86		
		72	0.224	0.83		
		96	0.365	0.86		
		132	0.654	0.93		
		168	0.869	1.01		
		192	0.990	1.01		
		288	1.000	1.00		

$P_{H2O} = 0.3$	1093	0.5	0.088	0.93	2.18 ± 0.03	1.56 ± 0.06
		2	0.591	0.73		
		3	0.796	0.82		
		6	0.998	0.93		
		12	1.000	1.00		
	1073	4	0.189	0.90	9.81 ± 0.30	1.68 ± 0.13
		8	0.512	0.90		
		12	0.762	0.68		
		18	0.942	0.86		
		24	0.934	1.05		
		36	1.000	1.00		
	1053	24	0.128	0.89	64.60 ± 1.97	2.11 ± 0.23
		48	0.378	0.99		
		60	0.550	0.78		
		72	0.784	0.82		
		96	0.869	1.05		
		132	0.937	0.98		
		144	0.979	0.97		
		168	1.000	1.00		
$P_{H2} = 5$	1113	0.5	0.510	0.87	0.69 ± 0.04	1.19 ± 0.13
		1	0.749	0.94		
		1.5	0.948	1.00		
		2	0.991	1.01		
		6	1.000	1.00		
	1093	1	0.112	0.97	3.79 ± 0.23	1.29 ± 0.14
		2	0.374	0.77		
		3	0.550	0.66		
		6	0.823	0.97		
		12	0.934	1.05		
		24	1.000	1.00		
	1073	6	0.133	0.94	20.19 ± 2.79	1.81 ± 0.69
		12	0.396	0.78		
		18	0.348	0.91		
		24	0.926	0.95		
		36	0.879	0.97		
		72	1.000	1.00		
$P_{total} = 5$ ($P_{H2O}/P_{H2} \sim 10^{-3}$)	1113	0.5	0.470	0.80	0.64 ± 0.01	1.82 ± 0.04
		1	0.891	0.84		
		1.5	1.000	0.93		
		2	1.000	0.95		
		6	1.000	1.00		
	1093	1.5	0.376	0.83	2.75 ± 0.15	1.40 ± 0.17
		3	0.623	0.77		
		4.5	0.899	0.84		
		6	0.963	0.97		
		12	1.000	1.00		
	1073	12	0.226	0.87	23.70 ± 1.29	2.83 ± 0.60
		18	0.296	0.89		
		24	0.658	0.78		
		36	1.000	0.91		
		48	1.000	1.00		

2.2.2 Analytical procedures

The size distribution of the starting material was determined with a laser diffraction/scattering particle size distribution analyzer (Horiba LA-960V2) at Horiba Instruments Inc. The starting material was dispersed in ethanol using an ultrasonic homogenizer (Nissei Corp. US-600AT, 600 W, 19.5 kHz) for 10 min in order to eliminate particle agglomeration. The homogenization duration of 10 min was chosen as that long enough to find a consistent size distribution irrespective of the dispersion time. The analysis was performed three times under the same sample preparation and analytical methods to ensure reproducibility.

Run products and the starting material were analyzed with Fourier transform infrared spectroscopy (FT-IR; JASCO FT-IR 4200), X-ray powder diffraction (XRD; Rigaku RINT–2100), field emission scanning electron microscopy (FE-SEM; JEOL JSM-7000F) and transmission electron microscopy (TEM; JEOL-2100F). For FT-IR analysis, run products were grinded for 15 minutes in an agate mortar to reduce the size/aggregation effects on infrared spectra, where larger grains tend to show less sharp, weaker absorption peaks (Koike et al., 2010). The samples heated in air showed no apparent effect of aggregation after 15-min grinding, whereas the aggregation effect could not be fully avoided for those heated in low pressures. A sample (~0.4 mg) and ground KBr powder were mixed in an agate mortar with a weight ratio of 1:500, and the mixed powder (0.2 g) was pressed into a pellet (Yamamoto & Tachibana, 2018). Infrared spectra in the wavenumber range of 370–7800 cm^{-1} were obtained with a spectral resolution of 4 cm^{-1}. For XRD analysis, the sample powder was placed on a non-reflective silicon sample folder. The measurements with a scan angle (2θ) of 15–80°, scan step of 0.01°, and scan speed of 1.0°/min were made with Cu Kα radiation (λ=1.54178Å). For FE-SEM and TEM analyses, the sample was dispersed in ethanol and dripped onto carbon tape and a carbon grid covered with copper for FE-SEM and TEM, respectively. Electron beam probes with 7–15 kV and 0.3 nA, 200 kV and 1.0 nA were employed for FE-SEM and TEM analysis, respectively.

2.3 Results

2.3.1 Grain size and shapes

The size distribution of the starting material, which was determined assuming a perfect spherical shape, has a single peak ranging from ~40 nm and 300nm with a mode grain diameter of 72 nm when evaluated by number of particles. The mode diameter is 123 nm for evaluation by volume. The spherical assumption was confirmed to be valid by SEM and TEM observations of particles (Fig. 2.1b). Both the size distribution and the mode grain diameter are similar to those

reported for amorphous forsterite (Mg_2SiO_4) nano-particles synthesized by the same method (~10–200 nm in size range, 80 nm in average diameter) (Koike et al., 2010; Imai, 2012; Yamamoto et al., 2018; Signorile et al., 2020).

While the starting material has a spherical shape with 40–300 nm in diameter, the samples heated in air have marginally rounded shape with ~1 μm in size. On the other hand, the samples heated at P_{H2O} of 0.3 Pa and $P_{tot.}$ of 5 Pa of H_2-H_2O gas mixture have blocky shapes with > 1 μm in size. The observation of the samples heated at 1073 K for short and long durations (12–36 h) in vacuum and at P_{H2} of 5 Pa clearly shows blocky grains formed through aggregation of the starting material. The loosely aggregated grains at all ambient gas conditions for short durations (8–18 h) indicate that sintering of the starting material proceeded simultaneously with crystallization of amorphous enstatite. I also found that longer heating in low pressures made the samples blockier in shape and larger than those heated in air, implying the presence of pressure effect (Fig. 2.1a). The size distributions for the grains milled for 15 min after the heating at low pressures does not significantly change from those before grinding (Fig. 2.1b). In spite of 15 min-grinding, the grains heated in vacuum and at P_{H2O} of 0.3 Pa remain blocky shapes and are mostly > 1 μm in size, however, typical grains milled for 15 min after the heating in air have rounded shape with < 1 μm in size.

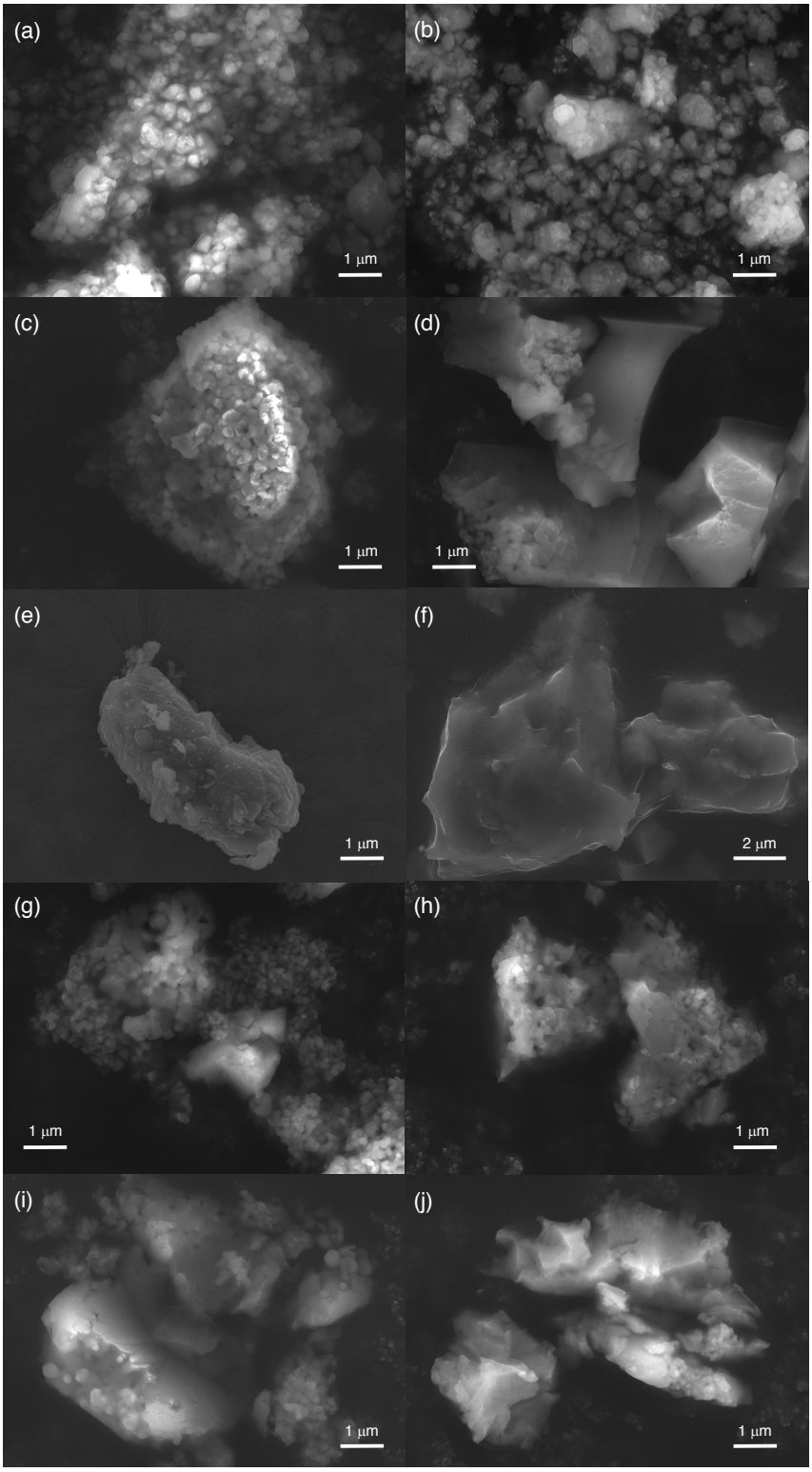

Fig. 2.1a SEM images of the samples heated at 1073 K and in air (P_{H2O} ~10^2 Pa) for 18 h (a) and 48 h (b), in vacuum (P_{H2O} ~10^{-4} Pa) for 12 h (c) and 24 h (d), at P_{H2O} of 0.3 Pa for 8 h (e) and 24 h (f), at P_{H2} of 5 Pa for 18 h (g) and 36 h (h), and at $P_{tot.}$ of 5 Pa (P_{H2O}/P_{H2} ~10^{-3}) for 18 h (i) and 36 h (j).

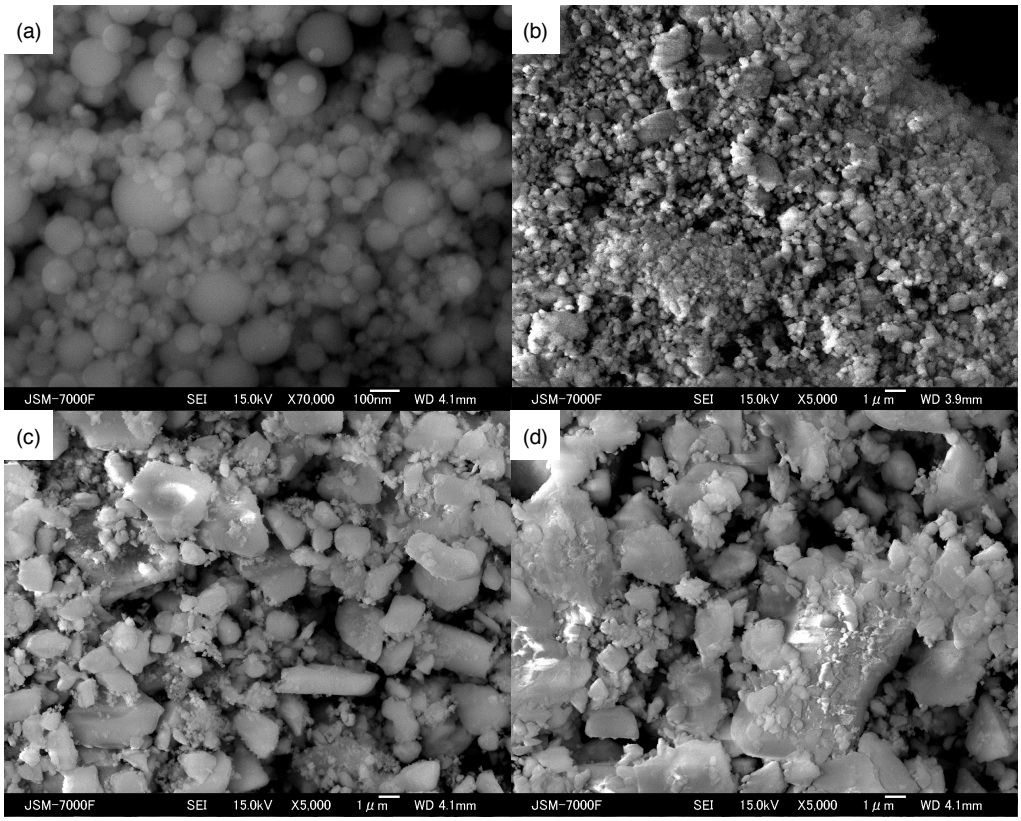

Fig. 2.1b SEM images of the starting material (a) and the samples milled for 15 minutes after the heating at 1073 K for 18 h in air (P_{H2O} ~10^2 Pa) (b), in vacuum (P_{H2O} ~10^{-4} Pa) (c) and at P_{H2O} of 0.3 Pa (d).

2.3.2 XRD profiles and TEM observation

An XRD profile of the starting material shows a halo pattern at ~20–40° with its peak at 26° in 2θ, characteristic of amorphous silicates originating from its disordered structure (Fig. 2.2a). Absence of any sharp peaks indicates that there is no crystallite phase in the starting material. Because enstatite has a lower Mg/Si atomic ratio (Mg/Si =1) compared to forsterite (Mg/Si =2), enstatite can form amorphous state easier than amorphous forsterite, resulting in the absence of pre-existing crystalline nuclei even though the same sample preparation method (Koike et al., 2010; Imai, 2012; Yamamoto & Tachibana, 2018). XRD profiles of the samples heated at 1093 K in air, in vacuum, at P_{H2O} of 0.3 Pa, at P_{H2} of 5 Pa and $P_{tot.}$ of 5 Pa of H_2-H_2O gas mixture for heating duration longer than 12 h show clear peaks of crystalline clino-/ortho-enstatite at ~20.1, 27.2, 28.1 and 31.1° accompanied by small peaks that represent crystalline forsterite at ~22.7, 25.4 and 39.5° in 2θ (Fig. 2.2a). Time evolution of XRD patterns for the sample heated at 1093 K in air shows that enstatite initially crystallizes from amorphous enstatite and

crystallization of forsterite is not observed for short heating durations (Fig. 2.2b). However, small peaks of forsterite appear as the crystallization proceeds. This clearly shows that the starting material transformed into mainly crystalline enstatite with a small amount of crystalline forsterite. Crystallization of forsterite is likely due to a slightly higher Mg/Si ratio from enstatite stoichiometry. XRD profiles of the samples heated at P_{H2O} of 0.18 MPa showed a slightly different crystallization behavior of amorphous enstatite in air. For the samples heated at 993 K, XRD peaks at 2θ of ~32.3, 40.0 and 52° originating only from forsterite were first recognized for 3 h. Those peaks grew and additional peaks that correspond to forsterite peaks at ~22.7, 25.4, 35.7 and 36.5 emerged for 6 h. While the peaks of forsterite became smaller or disappeared by further heating, some peaks at 2θ of ~20.1, 27.2, 28.1 and 31.1° attributed to crystalline enstatite appeared for 9 h. The shapes and positions of peaks for the 240 h-heated sample were similar to those for the longest duration under other ambient conditions, indicating that most of the starting material eventually transformed into enstatite under P_{H2O} of 0.18 MPa.

Figure 2.3 shows the grains of samples heated at 1073 K in air for 18h and in vacuum for 12h, which are not completely crystallized for the estimation with FT-IR analyses, in order to investigate the crystallization of amorphous enstatite at a particle level. Most of the heated grains have a look that crystalline parts exist in places with sintering between particles, as shown in both samples heated in air and vacuum. Electron diffraction patterns obtained from typical crystalline grains mainly showed many diffraction spots on a halo ring originating from the amorphous feature, which indicates that most grains would be partially crystallized. Furthermore, it was directly found that some grains heated in air had polycrystals in each particle from the electron diffraction patterns and their dark field images. These observations imply that partially crystallized samples do not consist of the mixtures of completely amorphous and crystallized grains, but rather the assemblage of which an individual particle gradually crystallized. While it was difficult to clearly determine crystalline phases due to small grain size of submicron order and containing polycrystals in many cases, electron diffraction patterns for some heated grains and lattice spacing of crystalline phases observed with high resolution images indicated that main crystalline phases were both clino-enstatite and ortho-enstatite.

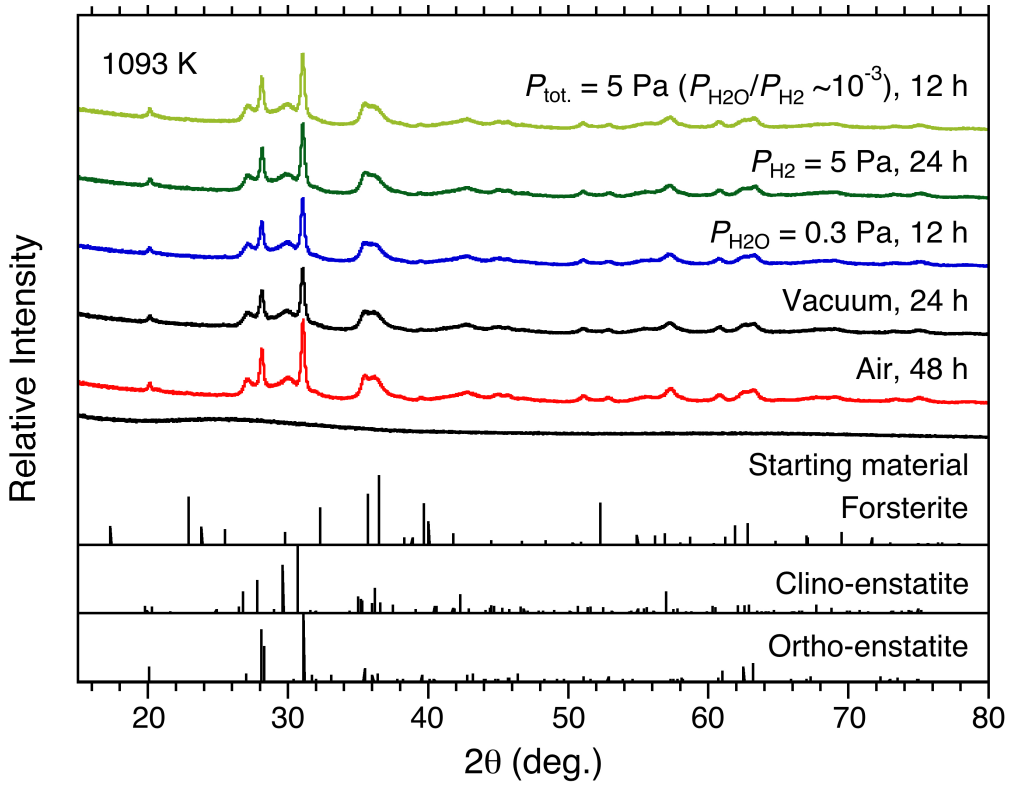

Fig. 2.2a XRD patterns of the starting material and the samples heated at 1093 K in air (P_{H2O} ~10^{2} Pa), in vacuum (P_{H2O} ~10^{-4} Pa), at P_{H2O} of 0.3 Pa, at P_{H2} of 5 Pa and at $P_{tot.}$ of 5 Pa (P_{H2O}/P_{H2} ~10^{-3}) for sufficiently long durations to crystallize completely. Typical peaks of clino/ortho-enstatite and forsterite are also given for references.

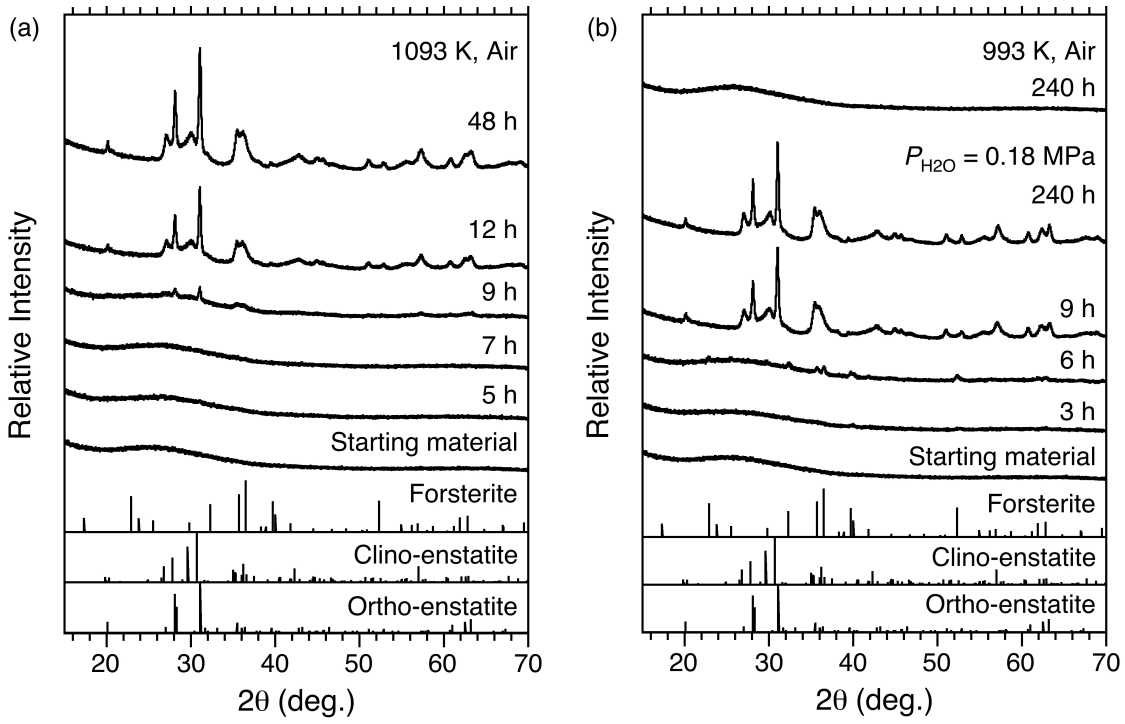

Fig. 2.2b Time evolutions for XRD patterns of the samples heated at 1093 K in air (P_{H2O} ~10^2 Pa) and at 993 K under P_{H2O} of 0.18 MPa for different durations (a~b). A XRD pattern of the sample heated at 993 K in air for 240 h (b). Typical peaks of clino/ortho-enstatite and forsterite are also given for references.

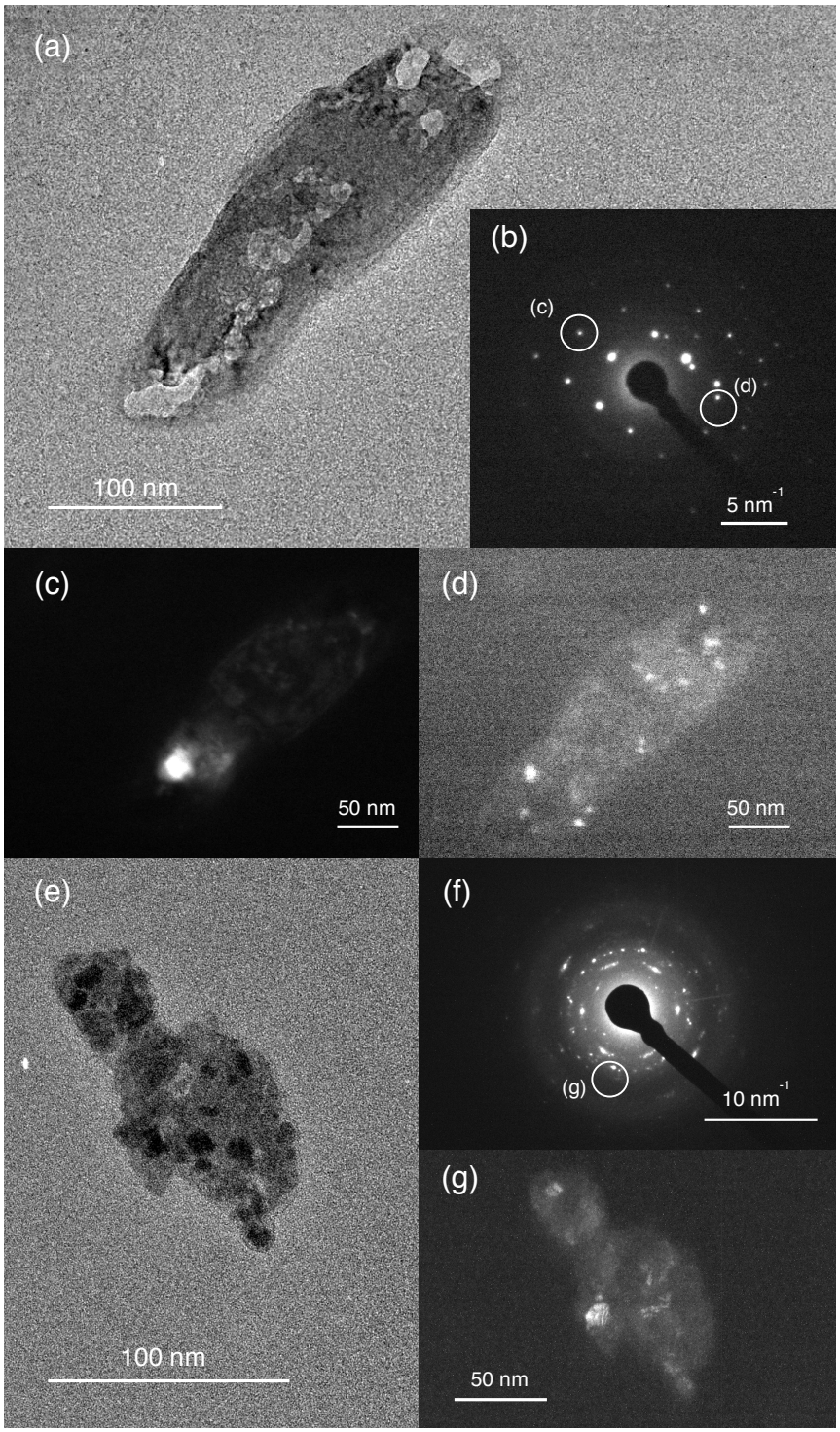

Fig. 2.3 TEM observations of the samples heated at 1073 K in air for 18 h (a~d) and in vacuum for 12 h (e~g). Bright field images of the grains heated in air and vacuum and their electron diffraction patterns are shown in (a, e) and (b, f), respectively. Bright areas of dark field images (c, d, g) represent crystalline parts corresponding with a diffraction spot (white circle) in the diffraction patterns (b, f).

2.3.3 Infrared spectral features and its time evolution

Infrared spectra of the starting material and the samples heated at 1093 K in air, in vacuum, at P_{H2O} of 0.3, at P_{H2} of 5 Pa, and $P_{tot.}$ of 5 Pa (P_{H2O}/P_{H2} ~10^{-3}), and the samples heated at 973 and 993 K under P_{H2O} of 0.18 MPa are shown in Fig. 2.4a, b. A spectrum of the starting material showed a broad and smooth absorption feature at ~10 μm and 18 μm, which is typical for amorphous silicates originating from the Si-O stretching vibration and the O-Si-O bending vibration modes, respectively. With the heating, the 10 and 18 μm peaks of the starting material gradually split into discrete peaks at ~9.3, 9.9, 10.6, 11.1, 11.6, 13.6, 13.8, 14.5, 15.5, 18.2, 19.5, 20.6, 21.7, and 23.2 μm, all of which are characteristic of crystalline enstatite (Chihara et al., 2002; Imai, 2012), at all experimental conditions except for P_{H2O} of 0.18 MPa (Fig. 2.4a). On the contrary to infrared spectral peaks of crystalline forsterite (Koike et al., 2010), no significant effect of the sample size and shape on the peak positions of crystalline enstatite was observed under these conditions. These peaks become shaper and stronger for further heating, and eventually remain unchanged with heating time. I found that the spectral peaks of the samples heated in air appeared to be shaper than those under lower pressures conditions (Fig. 2.4c). The peak sharpness of the samples heated in air increased with decreasing heating temperatures. In contrast, the spectral shapes of the samples heated at lower pressures seemed to be irrespective of the heating temperatures. Twin peaks at ~9.3 μm were observed only for the samples heated at the lowest temperature of 1053 K in air. These twin sharp peaks at ~10 μm were only observed for the enstatite and forsterite samples with spherical shape (Imai, 2012; Koike et al., 2010).

As observed in XRD patterns, infrared spectral features of the samples heated at P_{H2O} of 0.18 MPa are quite different with those heated under other ambient conditions (Fig. 2.4b). With heating for 24 h at 973 K and 3 h at 993 K, three spectral features/peaks at ~8, 9.3, and 22 μm appeared from the original halo peak at ~10 and 18μm of amorphous enstatite. This shoulder at ~8 μm and a peak shift of the amorphous feature from ~9.8 to 9.3 μm can be attributed to a presence of SiO_2 glass. After the heating for 96 h at 973 K and 9 h at 993 K, although a relative intensity of the peaks at ~9.3 to 10.6 μm for those samples was slightly high, spectral features became similar to those of the samples heated under other ambient gas conditions, which is consistent with XRD data as described above, suggesting that amorphous enstatite eventually transformed into mainly crystalline enstatite under P_{H2O} of 0.18 MPa.

Although I confirmed that crystallization of amorphous enstatite occured even at lower temperature of 993 K under P_{H2O} of 0.18 MPa as described above, crystallization of amorphous enstatite did not proceed at the same temperature in air for a long heating duration of 240 h (Fig.

2.4b). This is inconsistent with the results reported by Roskosz et al. (2011) where only forsterite crystallized from the sol-gel synthesis amorphous enstatite.

Time evolution of infrared spectra showed that the spectra of the samples heated in air changed more slowly than those under lower pressures at all experimental temperatures (Fig. 2.4a, c). For instance, the spectral change at 1053 K and P_{H2O} of 0.3 Pa occurred for the heating durations from 2 to 6 days, while that in air occurred the most slowly for the durations from 7 to 21 days. The heating timescales required for amorphous enstatite to completely transform into crystalline enstatite were 28 days in air, 12 days in vacuum (P_{H2O} of ~10^{-4} Pa), and 7 days at P_{H2O} of 0.3 Pa, respectively. Time evolutions of the infrared spectra under pure and H_2O-mixed hydrogen gas at 1073 and 1093 K were almost identical to those in vacuum. Spectral evolutions for the samples heated at P_{H2O} of 0.18 MPa indicated that the crystallization under water vapor with very high pressure occurred much faster than those in air and at low pressures.

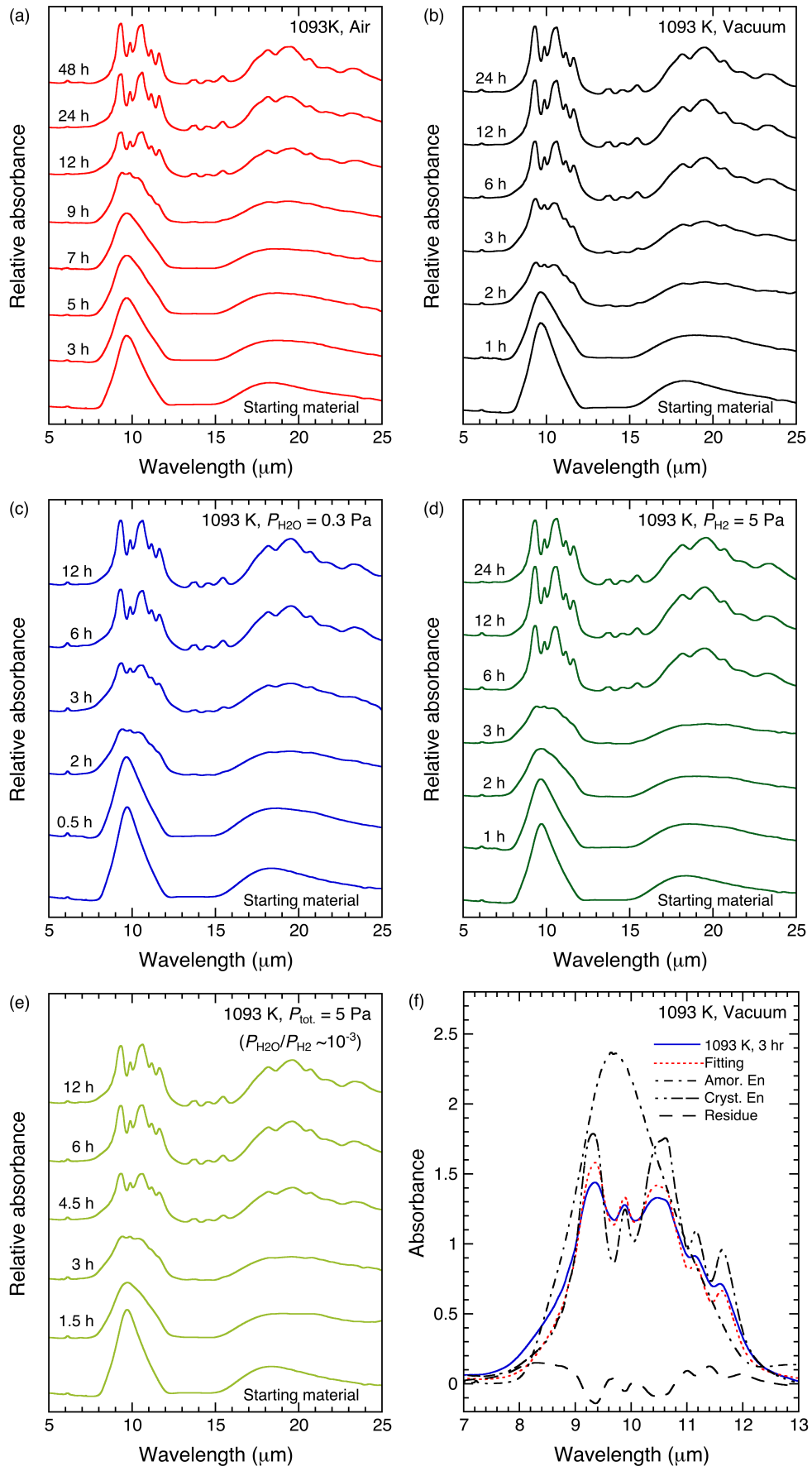
(a)
1093K, Air
48 h
24 h
12 h
9 h
7 h
5 h
3 h
Starting material
Relative absorbance
Wavelength (μm)
(b)
1093 K, Vacuum
24 h
12 h
6 h
3 h
2 h
1 h
Starting material
Relative absorbance
Wavelength (μm)
(c)
1093 K, P_{H2O} = 0.3 Pa
12 h
6 h
3 h
2 h
0.5 h
Starting material
Relative absorbance
Wavelength (μm)
(d)
1093 K, P_{H2} = 5 Pa
24 h
12 h
6 h
3 h
2 h
1 h
Starting material
Relative absorbance
Wavelength (μm)
(e)
1093 K, $P_{tot.}$ = 5 Pa
(P_{H2O}/P_{H2} ~10^{-3})
12 h
6 h
4.5 h
3 h
1.5 h
Starting material
Relative absorbance
Wavelength (μm)
(f)
1093 K, Vacuum
1093 K, 3 hr
Fitting
Amor. En
Cryst. En
Residue
Absorbance
Wavelength (μm)

Fig. 2.4a Infrared spectra of the starting material and the samples heated at 1093 K and in air (P_{H2O} ~10^2 Pa), in vacuum (P_{H2O} ~10^{-4} Pa), at P_{H2O} of 0.3 Pa, at P_{H2} of 5 Pa, and at $P_{tot.}$ of 5 Pa (P_{H2O}/P_{H2} ~10^{-3}) for different durations (a~e). Infrared spectral fitting of a heated sample with least squares method (f). Solid line, dot-dashed line, and dot-dot-dashed line represent the spectra of a sample heated at 1093 K in vacuum for 3 h, amorphous enstatite, and crystalline enstatite, respectively. Dotted line and dashed line show a fitted spectrum and the residue of the fitting.

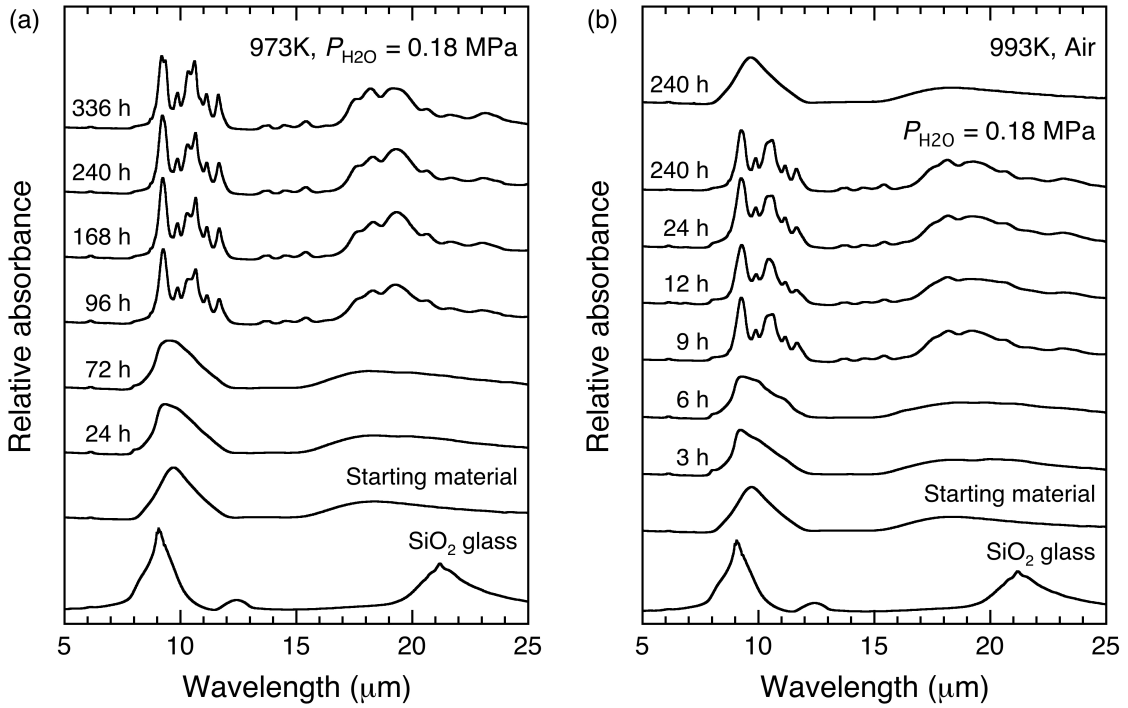

Fig. 2.4b Infrared spectra of the starting material, the samples heated at 973 (a) and 993 K (b) under P_{H2O} of 0.18 Pa for different durations, and the sample heated at 993 K in air for 240 h (b) together with a spectrum of SiO_2 glass for a reference.

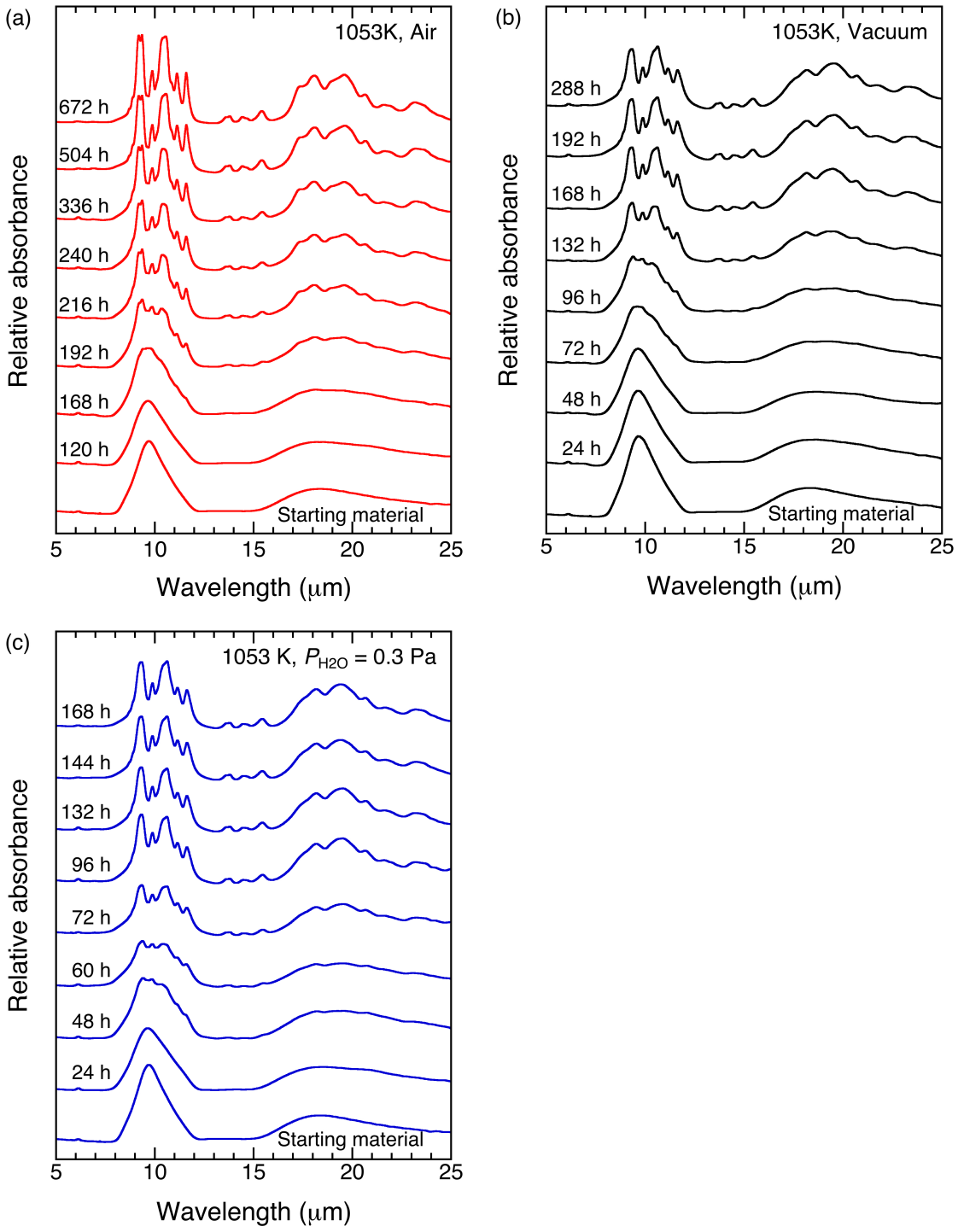

Fig. 2.4c Infrared spectra of the starting material and the samples heated at 1053 K in air (P_{H2O} ~10^{2} Pa), in vacuum (P_{H2O} ~10^{-4} Pa) and at P_{H2O} of 0.3 Pa for different durations (a~c).

2.4 Discussion

2.4.1 Crystallization kinetics of amorphous enstatite

Quantitative evaluation of degree of crystallization of amorphous enstatite (x) was made based on infrared spectral fitting in a range of 7–13 μm. I assumed that all the spectra could be expressed by the linear combination of the spectra of amorphous enstatite and crystalline enstatite. The absorbance of a partially crystallized sample (*Abs*) at each wavelength, can be expressed as;

$$Abs = y\left[Abs_{\text{amor.En}} \cdot (1 - x) + Abs_{\text{cryst.En}} \cdot x\right] \quad (1)$$

where $Abs_{\text{amor.En}}$ and $Abs_{\text{cryst.En}}$ are the absorbance of amorphous enstatite and crystalline enstatite, respectively. This evaluation method using infrared spectra was found to be valid based on the X -ray diffraction analysis reported by Imai (2012). I disregarded the presence of and forsterite, because the amount of forsterite is considered to be small from the XRD profile. Considering the XRD analytical result showing that no crystalline phases were present in the starting material, it is reasonable to consider that the degree of crystallization of the starting material would be zero. Because I confirmed by experiments under all conditions except for P_{H2O} of 0.18 MPa that enstatite was a dominant phase crystallized from the amorphous silicate with enstatite stoichiometry, it is inconceivable that crystallization ceases leaving residual amorphous phase. In this case, the samples heated for longer duration and showing no further infrared spectroscopic change would completely transform into crystalline enstatite. Therefore, I used infrared spectra of the samples heated for the longest duration at each T-P condition to estimate $Abs_{\text{cryst.En}}$. In crystallization experiments at low pressures (in vacuum, at P_{H2O} of 0.3 Pa and under hydrogen-gas), the drastic change of grain size and shape was observed, and its effect on infrared spectra before the onset of crystallization could not be eliminated by 15-min grinding in an agate mortar, so that I introduced a parameter y to adjust the intensity of infrared spectra of the samples heated in vacuum, at P_{H2O} of 0.3 Pa, and under hydrogen-gas. As mentioned above, the peak shift in infrared spectrum with changes in dust size and shape was not observed, and thus the peak intensity was only adjusted for fitting the obtained infrared spectra. The y was in the range of 0.65–1. Figure 2.4a (f) shows an example of spectral fitting of the samples heated for 3 h at 1093 K and in vacuum. The observed spectrum of the heated sample can be reproduced by fitted spectra derived from equation (1). The value of y was 0.84 for fitting of this sample.

Time evolution of the crystallization degree has been formulated using Johnson–Mehl–Avrami (JMA) equation (Johnson & Mehl, 1939; Avrami, 1939),

$$x = 1 - \exp[-(t/\tau)^n] \quad (2)$$

where x is the crystallization degree, t is the heating duration, τ is the time constant of the crystallization (time required for x, to reach ~0.63), n is the Avrami parameter which describes the crystallization mechanism involving nucleation and crystal growth. Figure 2.5 shows the best fitted curves obtained by the least-squares method using equation (2) under various ambient gases. Fitting results using equation (2) are listed in Table 2.1. All the curves under various ambient conditions showed a sigmoidal shape evolution path that reflects the delay of nucleation at the earliest stage of crystallization (Murata et al., 2009; Imai, 2012). This is consistent with the XRD result showing that the starting material is completely amorphous with the absence of crystalline nuclei.

Figure 2.6 shows the temperature dependence of the reciprocal time constant ($1/\tau$) for crystallization. The activation energies and frequency factors under various ambient gas pressures were determined from Arrhenius plots of reciprocal time constant for crystallization using the Arrhenius relation;

$$1/\tau = \nu_0 \exp(-E_a/RT) \quad (3)$$

where ν_0 is the frequency factor which is related with the number of collisions of molecules involving the nucleation and crystal growth, E_a is the activation energy including the kinetic barrier required for the nucleation and crystal growth depending on the crystallization mechanism. Crystallization in air proceeded with the slowest rate in range of experimental temperatures compared with lower pressure conditions. It was found that crystallization rate tended to increase with decreasing total pressure although the rate at P_{H2O} of 0.3 Pa is larger than that at P_{H2O} of (2–3) $\times 10^{-4}$ Pa.

The activation energies for crystallization in air, at P_{H2O} of 0.3 Pa, at $P_{tot.}$ of 5 Pa (P_{H2O} = ~5 $\times 10^{-3}$ Pa) and at P_{H2O} of (2–3) $\times 10^{-4}$ Pa were obtained to be 727 ± 89, 811 ± 41, 897 ± 91, and 951 ± 25 kJ/mol, respectively (Table 2.2). Imai (2012) reported an activation energy for crystallization of the same starting material in air as ~715 kJ/mol, which is very close to the value from the experiments in air in the present study (727 ± 89 kJ/mol). Because P_{H2O} in uncontrolled air is likely to be on the order of 10^2–10^3 Pa, the activation energy decreases proportionally with increasing the water vapor pressure of common logarithmic scale (Fig. 2.7). Although quantitative evaluation of crystallization rate for amorphous enstatite at P_{H2O} of 0.18 MPa could not be made due to crystallization of non-negligible amounts of forsterite, it was found that the crystallization rate was indeed faster than that in air. This pressure dependence is consistent with a previous result for crystallization of amorphous forsterite (Yamamoto & Tachibana, 2018). The solubility of water molecules is roughly proportional to square root of P_{H2O} (e.g., Sieverts, 1929; Newcombe

et al., 2017), and thus the pressure dependence of the activation energy indicates that water vapor lowers the kinetic barrier for crystallization of amorphous enstatite. The structure of amorphous enstatite is established by a partly polymerized SiO_4 framework with MgO_4 polyhedral that are corner-shared with SiO_4 unit (Wilding et al., 2004). At the presence of water vapor, water molecules diffusing into amorphous structure cut the existing cation-oxygen bonds in silicates and oxides, which could promote the mobility of network-forming cations (Si, Mg) into newly ordered silicate networks (Yamamoto & Tachibana, 2018). Under the P_{H2O} of 0.18 MPa condition, water vapor with a very high pressure might induce amorphous enstatite to behave like the enstatite-melt which firstly produces forsterite for the phase diagram in the MgO-SiO_2 system. Because SiO_2 glass and forsterite were observed as an initial phase of crystallization from amorphous silicate with enstatite composition with infrared spectra and XRD profiles, the amorphous silicate network would be remarkably modified by abundant water molecules, which brought about forsterite-crystallization. Therefore, crystallization of enstatite rapidly proceeded with nucleation of forsterite at temperatures where nucleation of enstatite does not occur. The activation energy under P_{H2} of 5 Pa was found to be 838 ± 14 kJ/mol, which are intermediate values between those at P_{H2O} of $(2–3) \times 10^{-4}$ and 0.3 Pa. Note that the obtained activation energies under all ambient conditions should contain the activation barrier for nucleation as well as that for crystal growth because of the absence of crystalline nuclei in the starting material. Therefore, the activation energies in the present study are much larger than that for crystallization of amorphous forsterite with pre-existing crystalline nuclei (~254–414 kJ/mol; Yamamoto & Tachibana, 2018).

Natural logarithm of frequency factors in air, at P_{H2O} of 0.3 Pa, at P_{H2O} of $(2–3) \times 10^{-4}$ Pa, P_{H2} of 5 Pa and $P_{tot.}$ of 5 Pa (P_{H2}/P_{H2O} ~10^{-3}) were estimated to be 69.5, 80.3, 95.6, 82.7 and 89.3 s^{-1}, respectively. The obtained frequency factors at different ambient gas pressures have a clear dependence on their own activation energies as in the case of the Yamamoto & Tachibana (2018), which indicates that both the frequency factor and activation energy reflect on the same crystallization behavior and mechanism under each ambient gas pressure. Some previous experiments used a mean vibration frequency of the lattice in magnesium silicates ($2.0–2.5 \times 10^{13}$ s^{-1}) as a reciprocal frequency factor (e.g., Fabian et al., 2000; Brucato et al., 2002; Djouadi et al., 2005), but I suggest that the frequency factor varies with ambient gas conditions (i.e., crystallization mechanism as discussed below in detail).

Table 2.2 Activation energies and natural logarithms of the pre-exponential factors for the crystallization rate of amorphous enstatite. Errors represent 1σ standard error of the mean.

Ambient gas (Pa)	activation energy (kJ mol^{-1})	ln ν_0 (s^{-1})
Air (P_{H2O} ~10^{2})	727.0 ± 89.4	69.5 ± 9.9
Vacuum (P_{H2O} ~10^{-4})	951.2 ± 24.9	95.6 ± 2.8
P_{H2O} = 0.3	811.1 ± 41.3	80.3 ± 5.0
P_{H2} = 5	838.3 ± 13.6	82.7 ± 1.5
P_{total} = 5 (P_{H2O}/P_{H2} ~10^{-3})	896.6 ± 90.6	89.3 ± 10.0

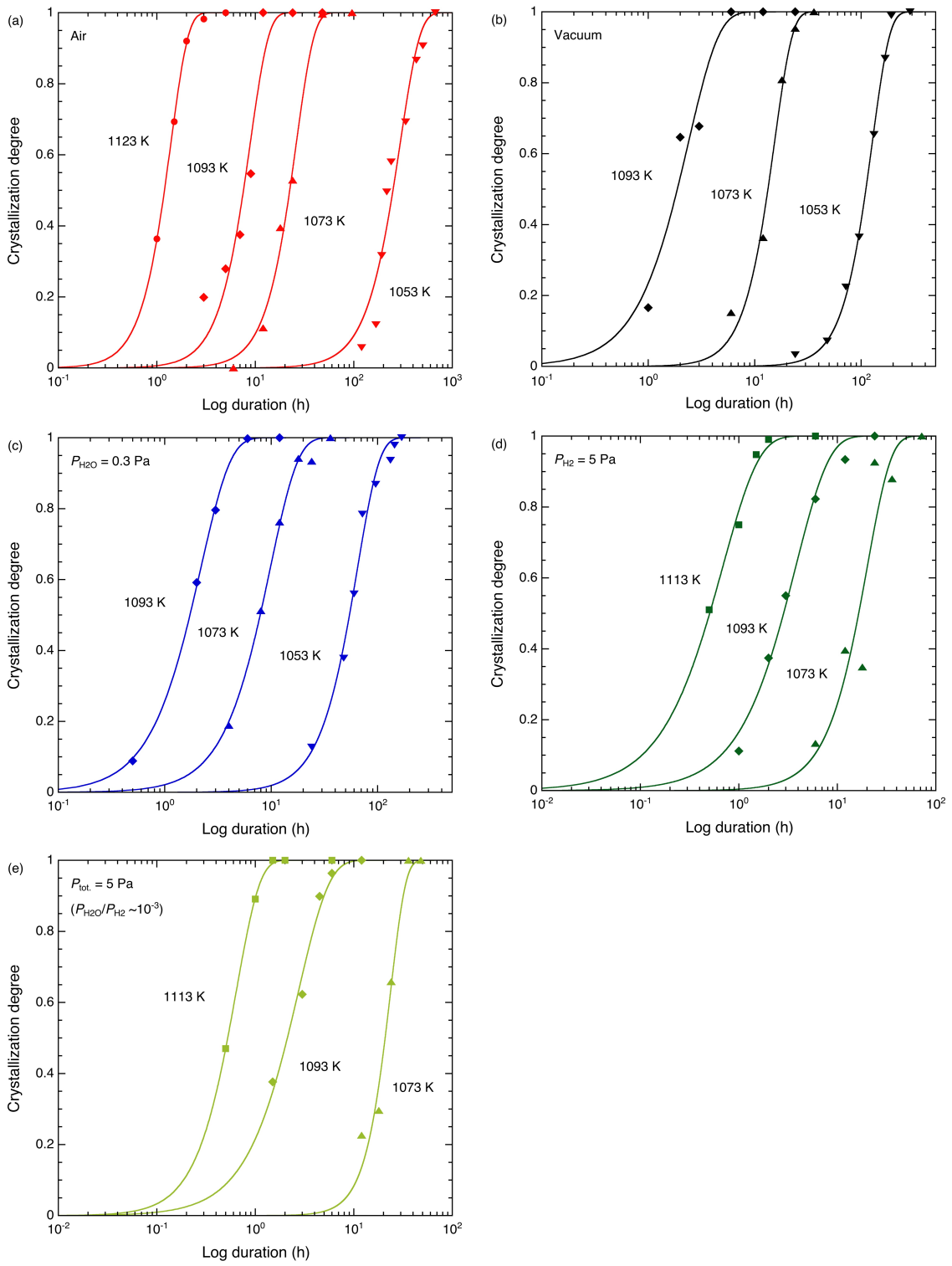

Fig. 2.5 Time evolution of crystallization degree estimated from the spectral fitting of the samples heated in air (P_{H2O} ~10^{2} Pa), in vacuum (P_{H2O} ~10^{-4} Pa), at P_{H2O} of 0.3 Pa, at P_{H2} of 5 Pa, and at P_{total} of 5 Pa (P_{H2O}/P_{H2} ~10^{-3}) for different temperatures with JMA equation (a~e).

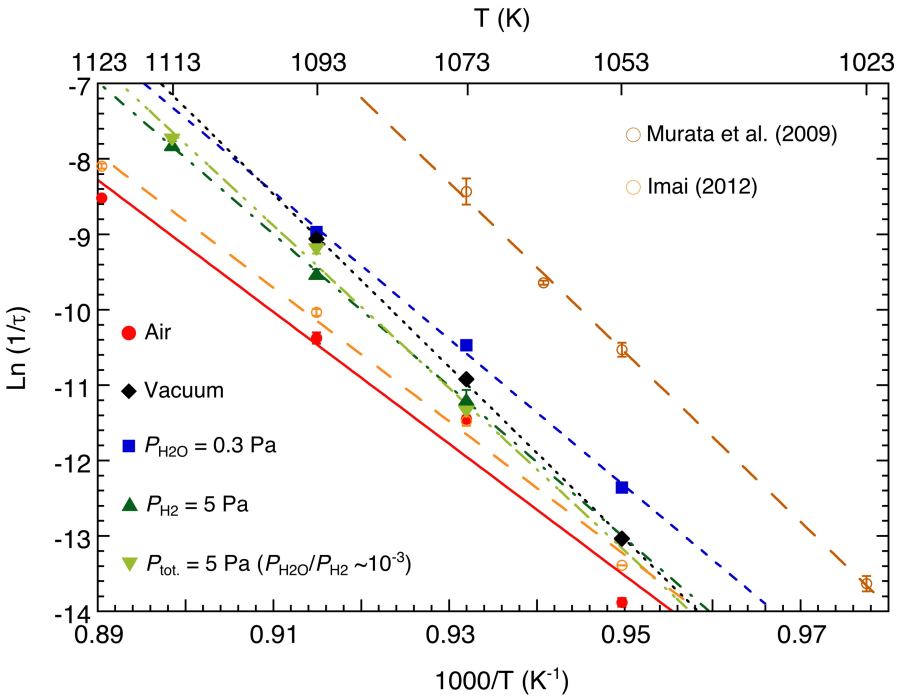

Fig. 2.6 Arrhenius plots of reciprocal time constant for crystallization of amorphous enstatite in air (P_{H2O} ~10^{2} Pa), in vacuum (P_{H2O} ~10^{-4} Pa), at P_{H2O} of 0.3 Pa, at P_{H2} of 5 Pa, and at $P_{tot.}$ of 5 Pa (P_{H2O}/P_{H2} ~10^{-3}). The lines of Arrhenius plots for crystallization of amorphous enstatite in previous studies are also shown as comparison.

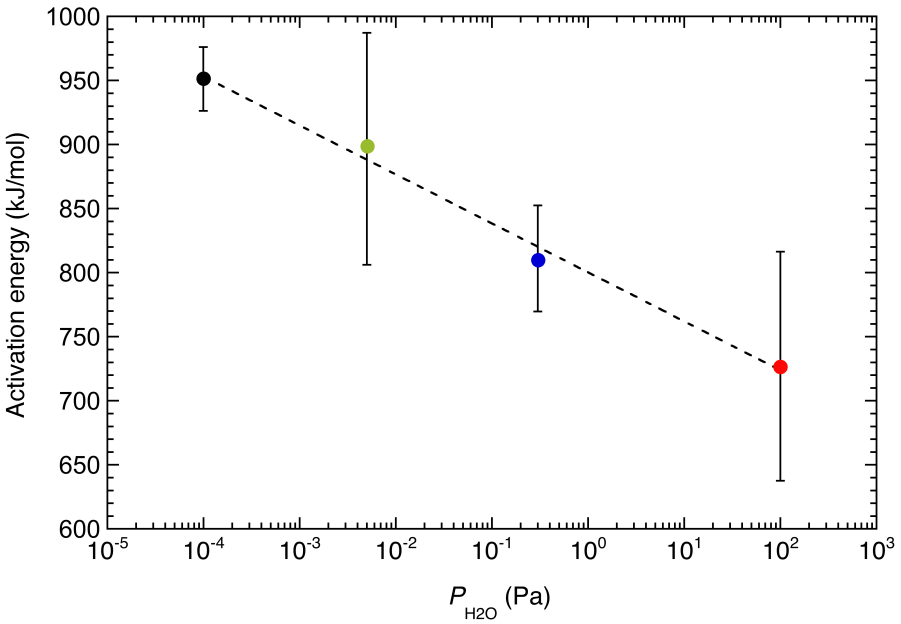

Fig. 2.7 Water vapor pressure dependence of the activation energies for the crystallization in air (P_{H2O} ~10^{2} Pa), in vacuum (P_{H2O} ~10^{-4} Pa), at P_{H2O} of 0.3 Pa, and $P_{tot.}$ of 5 Pa (P_{H2O} ~5×10^{-3}).

2.4.2 Crystallization mechanisms of amorphous enstatite

The mechanism of crystallization of amorphous silicates would be reflected as the Avrami exponent *n* in the JMA equation as mentioned above. In the present experiments, the three-dimensional crystal growth is plausible process considering the spherical shape starting material. I also note that the delay of nucleation should be reflected as the Avrami exponent *n* under all ambient conditions. The value of Avrami exponent *n* in air was ~2.2–2.5 and close to 2.5, implying that three-dimensional diffusion-controlled growth with homogeneous nucleation is a dominant mechanism (Jackson, 2004). This result is consistent with previous results of crystallization experiments of amorphous silicate with enstatite composition (n = 2.6 in Murata et al., 2009 and n = 2. 1–3.4 in Imai, 2012). The homogeneous nucleation is likely to take place from everywhere in the interior of grains and the crystal growth proceeds from the constant number of nuclei. While it was difficult to find the grains where the nucleation occurred from the interior by TEM analysis, I could observe some grains that contain many crystallites with different orientations, which implies the crystallization occurred not from a particular region but from several areas in a grain.

The values of *n* at P_{H2O} of (2–3) × 10^{-4} Pa, P_{H2O} of 0.3 Pa, P_{H2} of 5 Pa, and $P_{tot.}$ of 5 Pa (P_{H2}/P_{H2O} ~10^{-3}) are ~1.5–2.7, ~1.5–2.0, 1.0–2.0, and 1.4–2.8, respectively, and those values are typically smaller than those obtained in air. The JMA equation with n = 1.5 suggests that three-dimensional diffusion-controlled growth with heterogeneous nucleation is a suitable mechanism (Christian, 2002). Therefore, the smaller values of *n* compared with those in air could be explained by the increased contribution of nucleation and growth of crystalline enstatite from the grain surface. Nucleation and crystallization from the grain surface is likely to be attributed to evaporation of Si, Mg and O, which are amorphous constituent elements, from grain surface during annealing under low total pressure conditions (Rietmeijer et al., 1986). If this is the case, the modification of amorphous structures at the surface of the grain due to the evaporation would cause heterogeneous nucleation of crystalline enstatite at the grain surface. Intense aggregation of the samples heated under lower pressures conditions also supports the evaporation of elements from the grain surface because mass transport due to evaporation and condensation is a dominant sintering mechanism (Walker, 1955). Because the evaporation would accelerate the nucleation rate of crystalline enstatite, this interpretation could explain the fact that crystallization rate tends to become faster with decreasing total pressure of ambient gases. The fastest crystallization rate at P_{H2O} of 0.3 Pa can be interpreted as the result of accelerating of crystallization reaction due to both evaporation at the grain surface and diffusion of water molecules in the amorphous structure.

3
Crystallization and Phase Transition of Alumina Dusts in Protoplanetary Disks

3.1 Introduction

Although the abundance of alumina grains found in primitive meteorites is smaller than that of silicate grains, both solar and presolar alumina grains have been observed in primitive chondrites (e.g., Stroud et al., 2004; Takigawa et al., 2014). Oxygen isotopic compositions of presolar alumina imply that most grains originated from evolved stars such as red giants and AGB stars (Nittler et al., 1997, 2008). While primitive chondrites include a small amount of amorphous and poorly crystalline alumina grains, corundum is extremely dominant among alumina grains observed in chondrites (Takigawa et al., 2014). However, it was found that amorphous and transition alumina could be dissolved during acid treatments of chondrites (Takigawa et al., 2014), more alumina grains except for corundum can be present as protoplanetary dusts than the amount of these grains observed in meteorites. If it was the case, amorphous and crystalline alumina could survive or experience the heating events in the formation process of solar system as in the case of silicate dust.

Phase transition of aluminas (Al_2O_3) has been studied experimentally in the field of ceramic science. Crystalline alumina has several polymorphs largely divided into α-alumina and transition alumina. Alpha (α-) alumina is a thermodynamically stable phase of natural crystalline alumina, and transition alumina could be classified by the structures of precursor hydroxide; χ and κ-alumina made from Gibbsite, γ, δ and θ-alumina made from boehmite, and η and θ-alumina made from bayerite (Santos et al., 2000). Although alumina gel synthesized by sol-gel method is considered to transform into α-alumina through transition alumina such as γ, η and θ-alumina (Nishio & Fujiki, 1994; Ono & Masuo, 2004), crystallization kinetics of amorphous alumina has been not fully understood because amorphous and transition alumina are loosely compiled due to their complex classifications.

On the other hand, experimental studies on kinetics of phase transition from γ-alumina to α-alumina have been carried out a lot previously. Yamaguchi et al. (1976) conducted phase transition experiments of γ-alumina heated at 1173 K for 15 minutes with ~0.01 μm in size from alumina gel synthesized by the sol-gel method to determine the transition kinetics from γ-alumina to α-alumina through θ-alumina in air at 1353–1493 K. They obtained the transition rate with the activation energy of ~481 kJ/mol. Macêdo et al. (2007) performed the similar transition

experiments of γ-alumina xerogel heated at 572 K for 25 minutes from alumina gel, and obtained the activation energy of ~201 kJ/mol for the transformation into α-alumina without any intermediate phases such as θ or δ-alumina in air at 1023–1173 K. They consider that their low activation energy is caused by the high surface area (420 m^2/g) of γ-alumina. Isothermal transformation kinetics of γ-alumina gel obtained by calcining boehmite gel powders at 773 K for 12 h was also determined in McArdle & Messing (1993), the activation energy was evaluated to be ~578 kJ/mol for γ-α transformation via θ-alumina in air at 1373–1498 K. These studies show a wide range of activation energies of ~200–600 kJ/mol for the transformation from γ alumina to α-alumina. Moreover, crystallization and phase transition behaviors of alumina dusts in protoplanetary disks have not yet been understood, whereas the kinetics of phase transition from γ-alumina has been studied to investigate characteristics of aluminas (Al_2O_3) as material science. In this section, I determined crystallization and phase transition kinetics of alumina dusts to constrain the distribution of alumina dusts in protoplanetary disks.

3.2 Experiments

3.2.1 Annealing experiments

Micron-sized amorphous alumina particles, which were produced by drying a sol-gel synthesis alumina gel, were used as a starting material. The alumina gel was the same as that synthesized in Takigawa et al. (2014). The alumina gel was dried under different heating conditions (473–773 K for 2–48 h) (Table 3.1), and weight changes and phase identification of the dried samples were examined with an ultra-microbalance (Mettler Toledo XP2U) with a precision of ± 0.1 μg and X-ray diffraction analysis (XRD; Rigaku RINT–2100), respectively. Because α-alumina is nominally anhydrous mineral, annealing experiments of amorphous aluminas heated under different dry conditions were also performed at 1373 K for 12 h in air, under which amorphous alumina would almost completely transformed into α-alumina (McArdle & Messing, 1993), to investigate the amount of residual materials such as ethyl acetate, ethanol solvent and water in the amorphous alumina (Table 3.1). An appropriate heating condition of the alumina gel to produce amorphous alumina with a minimum amount of residual volatile materials without crystallization was examined by the results of both heating experiments as described above. The amorphous alumina particles were observed by a scanning electron microscope (SEM; JCM-7000 NeoScope).

Crystallization and phase transition experiments in air were conducted using ~10 mg of amorphous alumina powder, placed in a platinum dish, in electric furnaces (NITTO NHK-

170AF; AS-ONE HPM-ON). The temperature in the furnaces was calibrated against the melting points of Au (1336 K), NaCl (1073 K) and KBr (1003 K). After heating for the desired duration, the samples were taken out from the furnaces and rapidly cooled in air.

A time series of annealing experiments for crystallization from amorphous alumina into transition alumina were conducted at 943, 973, and 1023 K for 10 min–336 h (Table 3.2, 3.3a). The weight loss of some samples was also measured to investigate the effect of residual materials in the amorphous alumina on its phase transition kinetics.

The other time series of annealing experiments for crystallization from amorphous alumina into α-alumina was also conducted at 1223–1323 K for 1–672 h in air (Table 3.3b). In these experiments, the amorphous alumina was also used as the starting material. Annealing experiments at 1173 K for 6 h and at 1373 K for 12 and 24 h were also carried out to produce reference materials of transition alumina and α-alumina for XRD analysis. In order to assess the validity of the extrapolation of experimentally-determined phase transformation kinetics to lower temperatures and to compare the present results with those in previous studies, I performed additional annealing experiments at 1173 K for 120 and 912 h.

Table 3.1 Weight losses of amorphous alumina samples dried from the alumina gel at 473–773 K for 2–48 h in air, and additional weight losses of each amorphous alumina by heating at 1373 K for 12 h in air.

Drying conditions	Weight loss from alumina gel to amorphous alumina (wt%)	Weight loss by heating in air at 1373 K for 12 h (wt%)
473 K 48h	56	18
573 K 48h	65	8.3
673 K 12h	66	3.3
773 K 12h	67	1.3
773 K 2h	67	5.2

Table 3.2 Weight losses of amorphous alumina samples heated at 943–1023 K in air during amorphous alumina - transition alumina phase transition.

Temperature (K)	Duration (h)	Weight loss (wt%)
1023	0.17	5.1
	1	5.2
	48	5.0
973	0.5	5.1
	6	5.0
	96	5.1
943	1	5.2
	12	5.1
	336	5.2

Table 3.3a Crystallization degree from amorphous alumina into γ-alumina (x) evaluated based on the peak area of XRD profiles, time constants (τ) and the Avrami parameters (n) obtained by the fitting of temporal changes of x. Errors represent 1σ standard error of the mean.

Temperature (K)	Duration (h)	x	τ (h)	n
1023	2	0.39	4.75 ± 0.28	0.86 ± 0.08
	4	0.55		
	6	0.72		
	12	0.91		
	24	0.94		
973	12	0.39	27.2 ± 2.60	1.02 ± 0.19
	24	0.53		
	36	0.70		
	48	0.91		
	72	0.91		
943	24	0.33	110.9 ± 3.49	0.96 ± 0.06
	48	0.38		
	72	0.47		
	96	0.61		
	120	0.66		
	144	0.68		
	192	0.80		
	240	0.90		
	288	0.95		

Table 3.3b Degree of phase transition from γ-alumina to α-alumina (x) evaluated based on the peak area of XRD profiles, time constants (τ), and the Avrami parameters (n) obtained by the fitting of temporal changes of x. Errors represent 1σ standard error of the mean.

Temperature (K)	Duration (h)	x	τ (h)	n
1323	1	0.05	6.15 ± 0.61	1.33 ± 0.24
	3	0.28		
	6	0.70		
	12	0.83		
	24	0.99		
	48	0.98		
1273	1	0.02	26.5 ± 3.96	0.88 ± 0.15
	6	0.19		
	24	0.68		
	60	0.83		
	120	0.92		
	192	0.94		
1223	6	0.02	146.8 ± 17.0	0.80 ± 0.11
	24	0.15		
	72	0.51		
	120	0.59		
	240	0.71		
	312	0.89		
	480	0.85		
	672	0.99		
1173	120	0.27	–	–
	912	0.72		

3.2.2 Analytical procedures

The weight of the starting material and run products was measured with an ultra-microbalance (Mettler Toledo XP2U) with a precision of ± 0.1 μg before and after the heating experiments. The starting material and run products were analyzed with Fourier transform infrared spectroscopy (FT-IR; JASCO FT-IR 4200), X-ray powder diffraction (XRD; Rigaku RINT–2100), and a scanning electron microscope (SEM; JEOL JCM-7000 NeoScope). For FT-IR analysis, a sample (~0.4 mg) and ground KBr powder were mixed in an agate mortar with a weight ratio of 1:500, and the mixed powder (0.2 g) was pressed into a pellet (10 mm in diameter) (Yamamoto & Tachibana, 2018). Infrared spectra in the wavenumber range of 370–7800 cm^{-1} were obtained with a spectral resolution of 2 cm^{-1}. For XRD analysis, the powdery sample was placed into a hole (3 mm in diameter) on a non-reflective silicon sample folder (Yamamoto & Tachibana, 2018). The measurements with a scan angle in 2θ of 10–80°, scan step of 0.01°, and scan speed of 1.0° min^{-1} were made with Cu Kα radiation (λ = 1.54178 Å). Instead of using an internal standard for calibrate the X-ray intensity of the XRD profiles, I confirmed the background X-ray intensity every time. I adjusted the intensity of the XRD profiles of the run products using a newly obtained XRD pattern of the samples heated at 1173 K for 6h for crystallization from amorphous alumina into γ-alumina and the samples heated at 1373 K for 12 h for phase transition from γ-alumina into α-alumina, respectively, as discussed below, as standard substances when the background X-ray intensity differs from that of a previous one. The sample was dispersed onto carbon tape placed on a washer for the SEM analysis. Electron beam probes with 15 kV was employed.

3.3 Results

3.3.1 Characteristics of the Starting material

Table 3.1 shows the weight losses from the alumina gel to amorphous alumina dried at 473−773 K for 2−48 h in air and additional weight losses of the resulting materials at 1373 K for 12 h in air. The weight losses of the all dried samples at 473–773 K increased with increasing heating duration and then reached values in the range of 56–67 wt% (Table 3.1 and Fig. 3.1). Additional small amounts of weight losses at 1373 K through crystallization of α-alumina were also observed. These results suggest that dehydration-decarbonization that occured at 573–773 K would be almost complete and small amounts of relatively refractory materials still exist in the amorphous alumina. More dehydrated-decarbonated alumina is likely to be produced through a higher temperature dry procedure, but a small fraction of the resulting amorphous alumina

transformed into transition alumina at higher temperatures as shown in Fig. 3.2. While a XRD pattern of the alumina gel has many peaks at the range of ~10–75° in 2θ, all of these peaks disappeared after the drying treatments at 473–773 K for 2–48 h in air. XRD patterns of the samples dried at 673 and 773 K for 12 h showed small peaks at 2θ of ~38, 46 and 67° originating from γ-alumina. On the other hand, XRD profiles of the samples heated at 473 and 573 K for 48 h and at 773 K for 2 h showed only halo patterns at ~20–38°, 38–50° and 50–80° in 2θ, characteristic of amorphous alumina originating from its disordered structure (Takigawa et al., 2014). Considering XRD profiles of the dried samples and weight losses by heating in air at 1373 K for 12 h, the amorphous alumina dried in air at 773 K for 2 h in air was the most suitable material for the starting material in the present study.

Infrared spectra of the alumina gel, the starting material and the sample heated in air at 1173 K for 12 h are shown in Fig. 3.3. The spectrum of the alumina gel showed large peaks at ~1480 and 1600 cm^{-1} originating from carbonates and water, respectively, a broad peak at ~3400 cm^{-1} corresponding to adsorbed water molecules, and a relatively sharp peak at ~3680 cm^{-1} which would be attributed to Si-OH stretching vibration (Kebukawa et al., 2019). A sharp peak at ~3680 cm^{-1} was not observed in the starting material and the sample heated in air at 1173 K for 12 h, which is suggestive of the lack of structural OH in the starting material that would significantly affect the crystallization kinetics of amorphous alumina (Jäger et al., 2003; Yamamoto & Tachibana, 2018).

The starting material has irregular/blocky shapes with a size ranging from a few to 50 μm in diameter with the typical grain size of smaller than ~10 μm (Fig. 3.4). The observations of relatively large grains showed that small particles of the starting material stuck together fluffily on the grain surface.

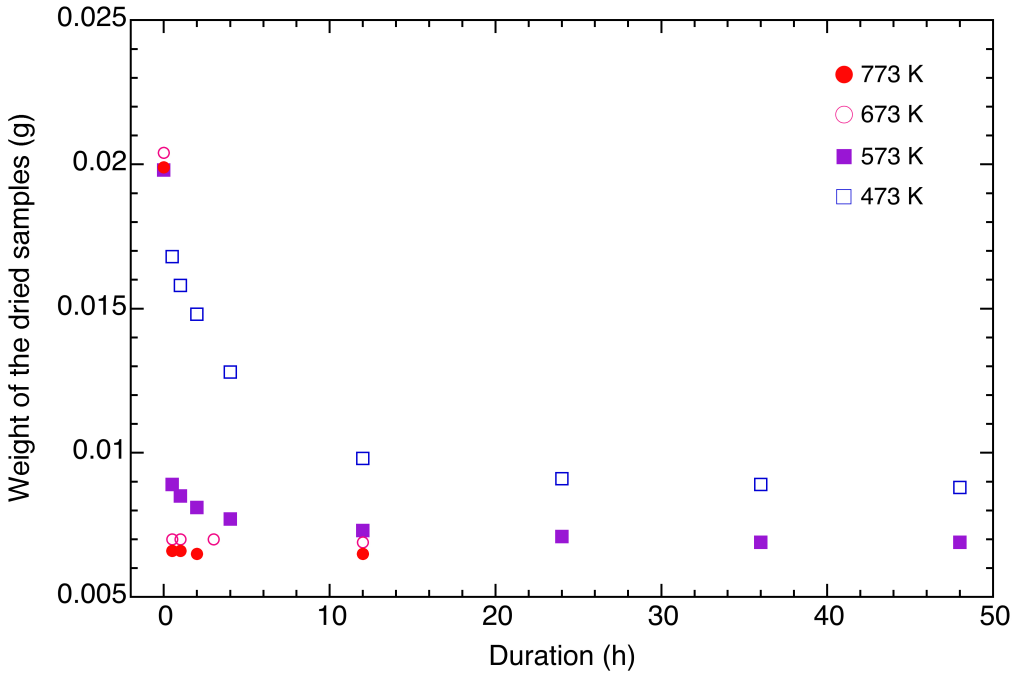

Fig. 3.1 Temporal change for the weight of the samples dried from the alumina gel to amorphous alumina in air at 473–773 K for 0.5–48 h.

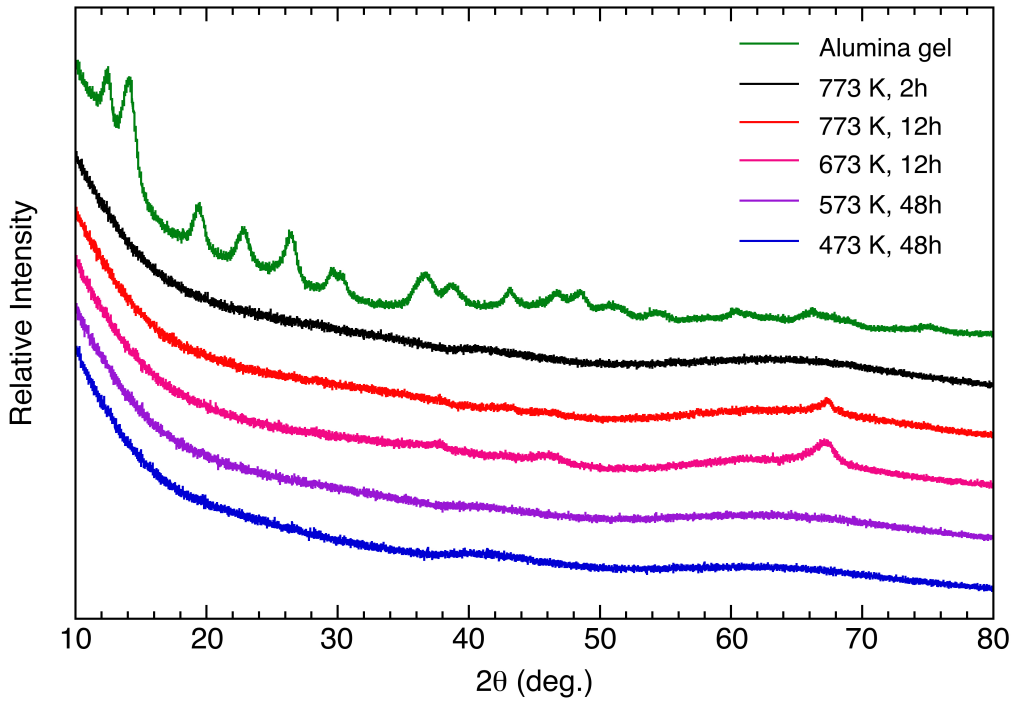

Fig. 3.2 XRD patterns of the alumina gel and the samples dried in air at 473–773 K for 2–48 h.

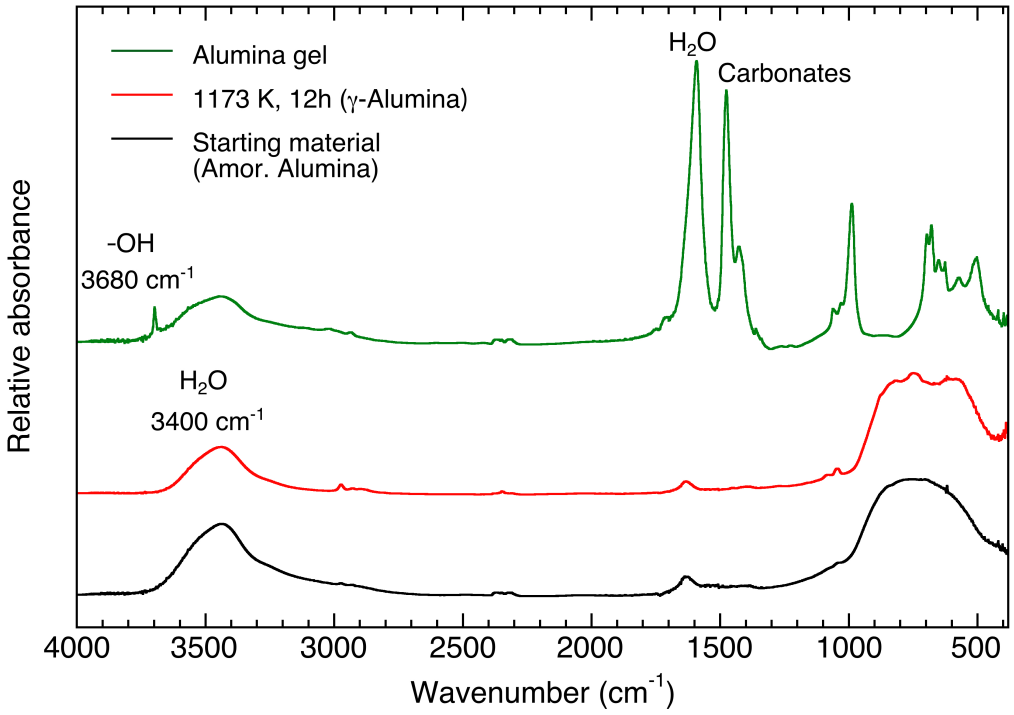

Fig. 3.3 Infrared spectra of the alumina gel, the starting material, and the samples heated in air at 1173 K for 12 h.

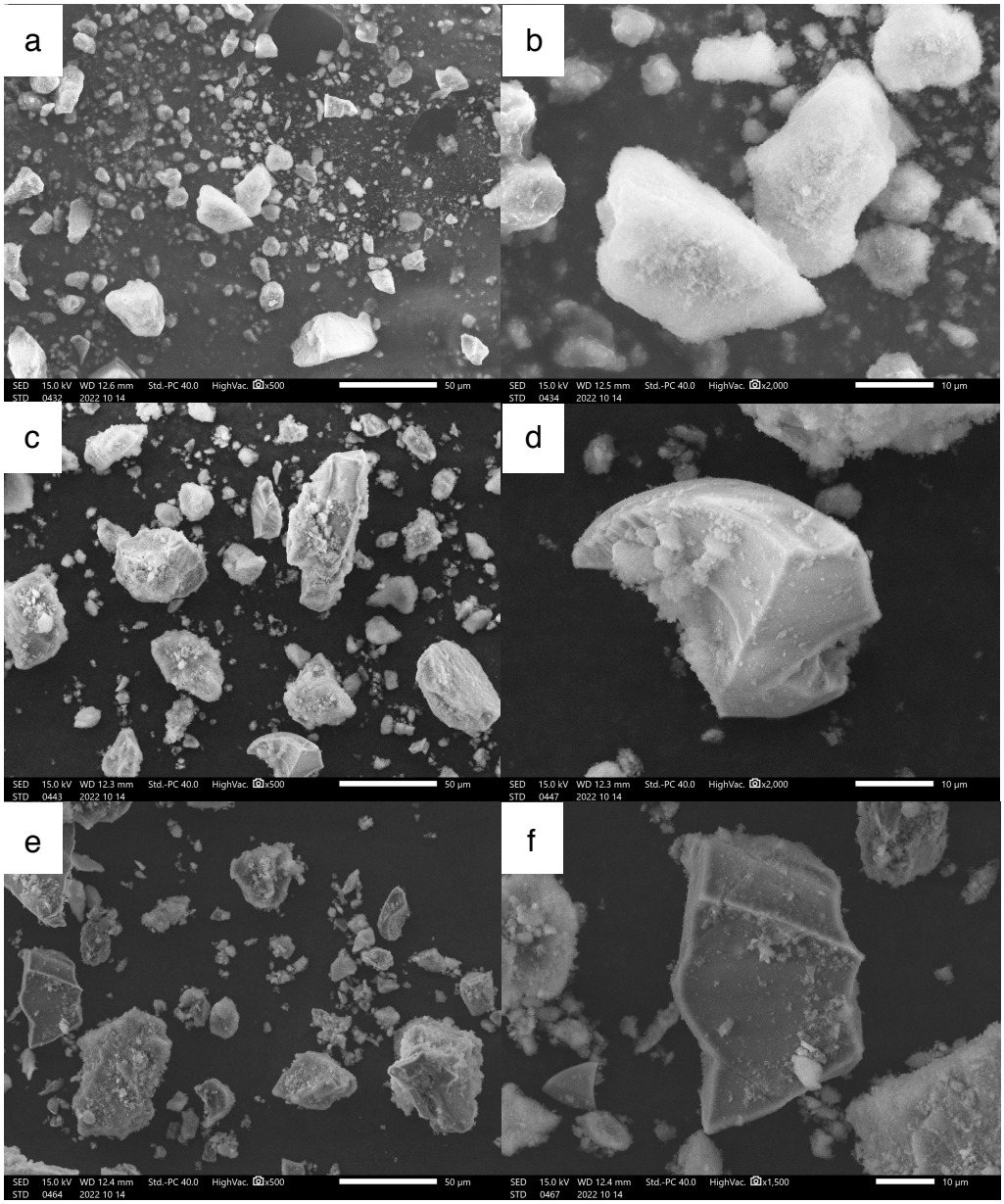

Fig. 3.4 SEM images of the amorphous alumina (a, b) and the samples heated in air at 1023 K for 24 h (c, d) and at 1323 K for 24 h (e, f).

3.3.2 Run products

3.3.2a 943, 973, 1023, and 1173 K

An XRD profile of the sample heated at 1173 K for 6 h showed some peaks of γ-alumina at 32.7, 37.6, 39.6, 45.8, 60.9 and 67.0° in 2θ (Fig. 3.5). It was found that other transition alumina phases such as δ and θ-alumina were not observed by the heating at 943–1173 K. By further heating, sharp peaks at 25.6, 35.2, 37.8, 43.4, 52.6, 57.5, 61.3, 66.5, 68.2, 76.9 and 77.2 in 2θ gradually appeared for 120–912 h, in contrast to the broad peaks of γ–alumina, which

gradually disappeared.

Figure 3.7 shows XRD patterns of the samples heated at 943, 973, and 1023 K for various heating durations. Those for the samples heated for the shortest duration at each temperature are shown in Fig. 3.6. XRD patterns of the samples heated for the shortest duration showed dominantly amorphous halo at 20–38° in 2θ with weak peaks of γ-alumina. The weight losses of the samples heated for the shortest duration reached at ~5 wt%, and further changes in weight losses for longer duration were not observed. These results suggest that evaporation of volatile materials in the starting material would be almost completed during the very early stage of crystallization at 943, 973, and 1023 K. Under all conditions, peaks at 61 and 67° in 2θ originating from γ-alumina gradually appeared with heating duration from the original halo pattern of the amorphous alumina. I observed no further change in the intensity of the peaks at 61 and 67° in 2θ after 240 h-, 48 h-, and 12 h-heating at 943, 973, and 1023 K, respectively. Furthermore, the intensities and shapes of the XRD peaks of the heated for the longest duration at each temperature resemble with those of the samples heated at 1173 K for 6 h.

The surface of the almost completely crystallized sample (1023 K, 24 h) showed more clear and pointed shapes than the starting material (Fig. 3.4). The sample mainly have more aggregated particles with the size range of 10–50 μm.

3.3.2b 1223, 1273, 1323, and 1373 K

The sample heated at 1373 K for 12 h showed a XRD peaks of α-alumina. Further change in the XRD pattern by heating for longer than 12 h was not observed (Fig. 3.5).

The changes in the XRD profiles of the samples heated at 1223, 1273, and 1323 K for 10 min–672 h are shown in Fig. 3.7. For instance, at 1223 K, only some broad peaks of γ-alumina were detected for 10 min–6 h, and small peaks of α-alumina appeared after 24 h-heating. The broad peaks of γ-alumina gradually disappeared by further heating, and eventually only sharp peaks of α-alumina were only detected. Similar time evolutions of the XRD peaks were also observed at 1273 and 1323 K. These results indicate that amorphous alumina transformed into α-alumina through the formation of γ-Alumina.

Similar to the observational results at 1023 K, the sample heated at 1323 K for 24 h, which is almost completely crystallized sample as discussed below, has clear and pointed shaped surface (Fig. 3.4). The range of the grain size is typically 10–50 μm in diameter.

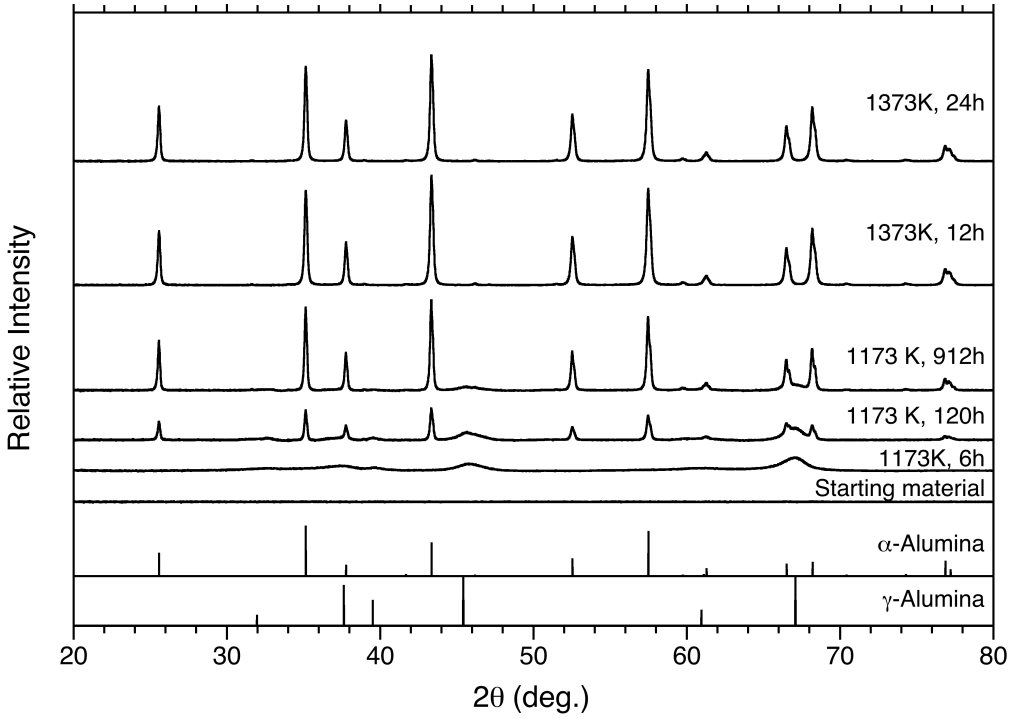

Fig. 3.5 XRD patterns of the staring material and the samples heated at 1173 for different durations and at 1373 K for 12h and 24 h.

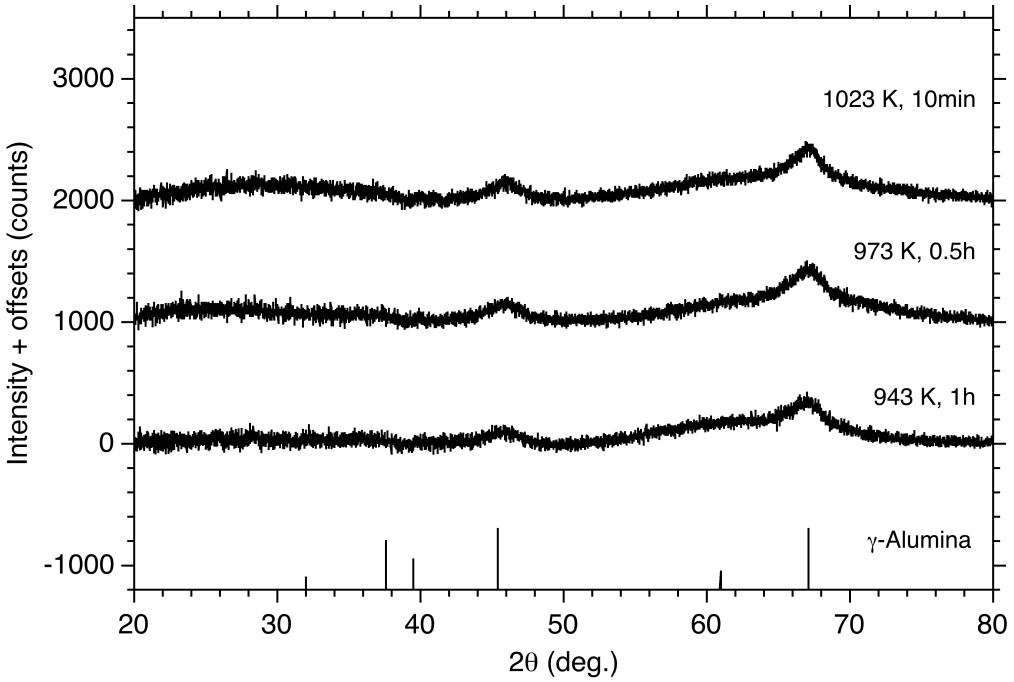

Fig. 3.6 XRD profiles of the samples heated at 943–1023 K for the shortest durations (10 min–1 h).

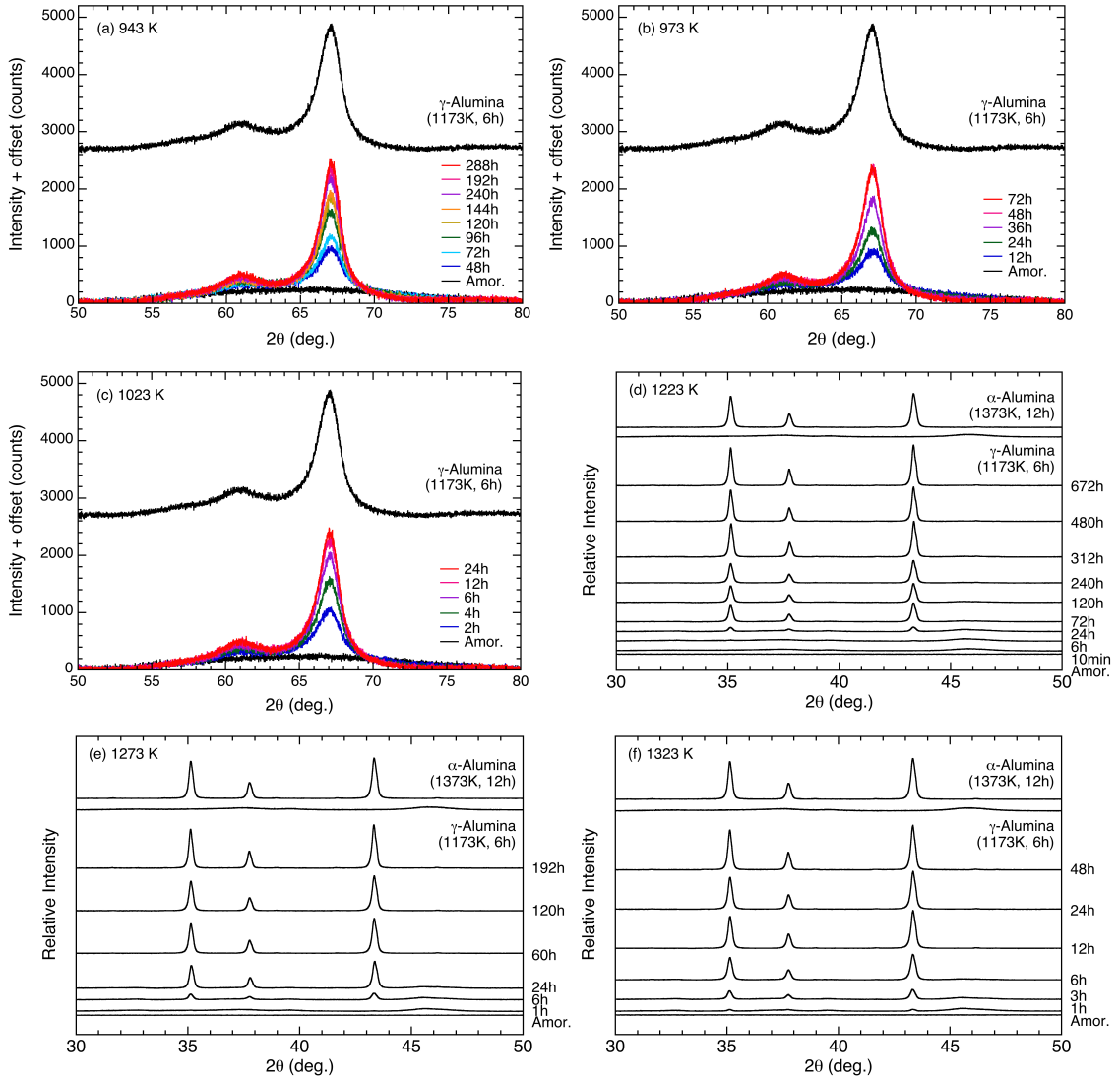

Fig. 3.7 Time evolution of XRD patterns of the samples heated in air at 943–1323 K for different durations (a~f). XRD profiles of the samples heated at 1223–1323 K (d, e, f) are arbitrarily shifted in the vertical direction for clearly. XRD patterns of the samples heated at 1173 K for 6 h and at 1373 K for 12 h are shown as references of γ-alumina and α-alumina, respectively.

3.4 Discussion

3.4.1 Crystallization degree from amorphous alumina at 943, 973, and 1023 K

I confirmed that γ-alumina was only a phase transformed from amorphous alumina at 943, 973, and 1023 K among a series of transition alumina. It was also found that amorphous alumina transformed into γ-alumina before the appearance of α-alumina at temperatures higher than 1173 K. Therefore, I discussed crystallization from amorphous alumina into γ-alumina here. Quantitative evaluation of crystallization degree from amorphous alumina into γ-alumina ($x_{\mathrm{amor.}\gamma}$)

was made using the XRD patterns of the samples in a range of 50–80° in 2θ where the evolution of XRD profiles associated with the crystallization was observed. The XRD pattern of the starting material lacks relatively sharp peaks attributed to transition alumina and α-alumina, and thus it can be regarded as totally amorphous alumina (i.e., $x = 0$). Because XRD patterns of the samples heated for longer durations at each temperature showed no further change and resembled with that of the sample heated at 1173 K for 6 h as mentioned above, I treated the XRD profiles of the samples heated for the longest durations as almost totally transformed γ-alumina. In order to acquire a calibration curve that can be used for evaluation of the crystallization degree, the starting material and the sample heated at 1173K for 6 h were mixed with the appropriate mass ratios of 0.25, 0.5 and 0.75. The relation between peak areas at 50–80° in 2θ of the XRD patterns and the mixing ratios showed a good linear correlation. Because both alumina phases have the same molecular weight, the estimated calibration curve can be used to estimate the crystallization degree for the experimental products (Fig. 3.8).

3.4.2 Degree of phase transition from γ-alumina at 1223, 1273, and 1323 K

Crystallization from amorphous alumina into α-alumina occurred through the formation of γ-alumina at 1223, 1273, and 1323 K. However, the timescale of amorphous-γ phase transition was much smaller than the timescale of γ-α phase transition, and thus it is reasonable to be considered that these time series of XRD profiles for the samples heated at 1223–1323 K are regarded as the phase transition from γ-alumina to α-alumina. The evaluation of the degree of γ-α phase transition ($x_{\gamma\text{-}\alpha}$) was also made with the same way as that for the case of amorphous-γ phase transition. As mentioned above, I found that the XRD pattern of the sample heated at 1373 K for 12 h indicated the formation of α-alumina, and further heating did not result in the change in the XRD pattern (Fig. 3.5). Therefore, I used the XRD patterns of the samples heated at 1173 K for 6 h and at 1373 K for 12 h as γ-alumina and α-alumina references, respectively. Linear relation between a peak area in a range of 43–44° in 2θ and for the mixed samples of γ and α-alumina was obtained as a calibration curve (Fig. 3.8).

The values of $x_{\gamma-\alpha}$ at 1173, 1223, 1273, and 1323 K are summarized in Table 3.3b and the temporal changes of $x_{\gamma-\alpha}$ at 1223, 1273, and 1323 K are shown in Fig. 3.9. γ-α phase transition also begins to occur at the initial stage of heating procedure as in the case of crystallization of amorphous alumina. The degree of phase transition ($x_{\gamma-\alpha}$) at 1173 K for the samples heated for 120 and 912 h were estimated 0.27 and 0.72, respectively, suggesting that an e-folding timescale of the phase transition at 1173 K would be between 120 h and 912 h.

3.4.3 Kinetics of crystallization and phase transition of aluminas

Time evolution of the crystallization and phase transition degree has been formulated using Johnson–Mehl–Avrami equation (Johnson & Mehl, 1939; Avrami, 1939),

$$x = 1 - \exp\left[-(t/\tau)^n\right] \quad (2)$$

where x is the crystallization and/or phase transition degree, t is heating duration, τ is the time constant for the crystallization and/or phase transition (time required for x ~0.63), n is the Avrami parameter which describes the mechanism of the crystallization and/or phase transition involving nucleation and crystal growth. Best fitted curves obtained by the least-squares method using Eq. 2 are shown as solid curves in Fig. 3.8, and the obtained parameters of τ and n are listed in Table 3.3a and 3.3b. The τ for γ-α phase transition at 1173 K could not be estimated accurately due to the lack of temporal change at this temperature, but it would be between 120 h and 912 h and be close to 912 h. The estimated Avrami exponents n at each temperature were close to 1 for both crystallization of amorphous alumina and transformation from γ-alumina to α-alumina, implying that the crystal growth initiated at heterogeneous nucleation is a dominant mechanism (Christian, 2002). The average of Avrami exponents for γ-α phase transition in the present study is consistent with that in Yamaguchi et al. (1976). Because crystallization from amorphous alumina without any crystalline nuclei and γ-α phase transition would require the nucleation from disordered structures and a rearrangement from a face-centered cubic lattice (γ-alumina) to a hexagonal close packed structure (α-alumina) (Levin & Brandon, 1998), respectively, the value of n should be larger than 1 for the case of crystallization associated with nucleation and γ-α phase transition. Kaito et al. (2007) reported that the energy released by graphitization of the deposited carbonaceous layer could induce a growth of forsterite nano-crystallites without heating. I thus considered that residual water molecules and/or organic compounds in the starting material synthesized by sol-gel method might be likely to help the nucleation of γ-alumina and α-alumina at the initial stage of the crystallization and phase transition. Note that water molecules and organic compounds evaporate at the very early stage of crystallization based on the weight losses of the samples as mentioned above (Table 3.2), suggesting that subsequent crystal growth after the formation of crystalline nuclei would not be accelerated by the residual materials in the starting material.

Figure 3.10 shows the temperature dependence of the reciprocal time constant ($1/\tau$) for crystallization of amorphous alumina and γ-α phase transition. The obtained temperature dependences showed a good agreement with Arrhenius relation, from which activation energies and frequency factors were determined;

$$1/\tau = \nu_0 \exp(-E_a/RT) \quad (3)$$

where ν_0 is the frequency factor which is related with the number of collisions of molecules involving the nucleation and crystal growth, E_a is the activation energy including the kinetic barrier required for the nucleation and crystal growth depending on the crystallization mechanism. The activation energies for crystallization from amorphous alumina and γ-α phase transition were obtained to be 314 ± 18 and 427 ± 10 kJ/mol, respectively. The natural logarithm of frequency factors for the crystallization and the γ-α phase transition were also estimated to be 27.2 ± 2.27 and 28.8 ± 0.95, respectively. The relation of these two Arrhenius lines shows that crystallization rate of amorphous alumina is larger than phase transition rate of γ-alumina at every temperature, which indicates that amorphous alumina transforms into α-alumina through γ-alumina in all temperature conditions. It was also found that crystallization from amorphous alumina in air occurred at the close rate of crystallization from amorphous forsterite at P_{H2O} of 0.3 Pa (Yamamoto & Tachibana, 2018). The γ-α transition rates in the present study differ from those obtained in Macêdo et al. (2007) who reported much faster transition rates at lower temperatures and lower activation energy for γ-α phase transition. Because the degrees of γ-α phase transition at 1173 K for 120 and 912 h are consistent with its time evolution derived using the JMA equation from the values of $n = 1$ and τ obtained from the extrapolation of Arrhenius plots for the γ-α phase transition, the Arrhenius line can be extrapolated to a lower temperature of 1173 K, which can directly compare a rate constant of ~850 h for the phase transition at 1173 K with that of ~17 h reported in Macêdo et al. (2007). Although the high surface area of γ-alumina might explain the much faster transition rates and the lower activation energy as argued by Macêdo et al. (2007), the lower temperature-short duration drying procedure of alumina gel in Macêdo et al. (2007) (573 K for 25 min) compared with this study (773 K for 2 h) would cause the formation of the starting material with much amount of water molecules, which could also promote the γ-α phase transition and decrease the activation energy of the reaction. While the activation energy of 481 kJ/mol for γ-α phase transition reported in Yamaguchi et al. (1976) is different from that of 578 kJ/mol in McArdle & Messing (1993), their transition rates of τ take similar values at ~1350–1500 K. The Arrhenius plots for γ-α phase transition at 1223–1323 K in the present study represent transition rates at a temperature range lower than those in previous studies. Because the extrapolated line of Arrhenius plots to higher temperatures fitted well on their Arrhenius plots, I could obtain the Arrhenius line which is consistent with the transition rates reported in Yamaguchi et al. (1976) and McArdle & Messing (1993), and aligns three different data for the γ-α transition rates at each temperature.

Table 3.4 Activation energies and natural logarithms of the pre-exponential factors for crystallization and transition rate of aluminas.

crystallization/phase transition	activation energy (kJ mol^{-1})	ln ν_0 (s^{-1})
Amorphous →γ -Alumina	314 ± 18	27.2 ± 2.27
γ →α -Alumina	427 ± 10	28.8 ± 0.95

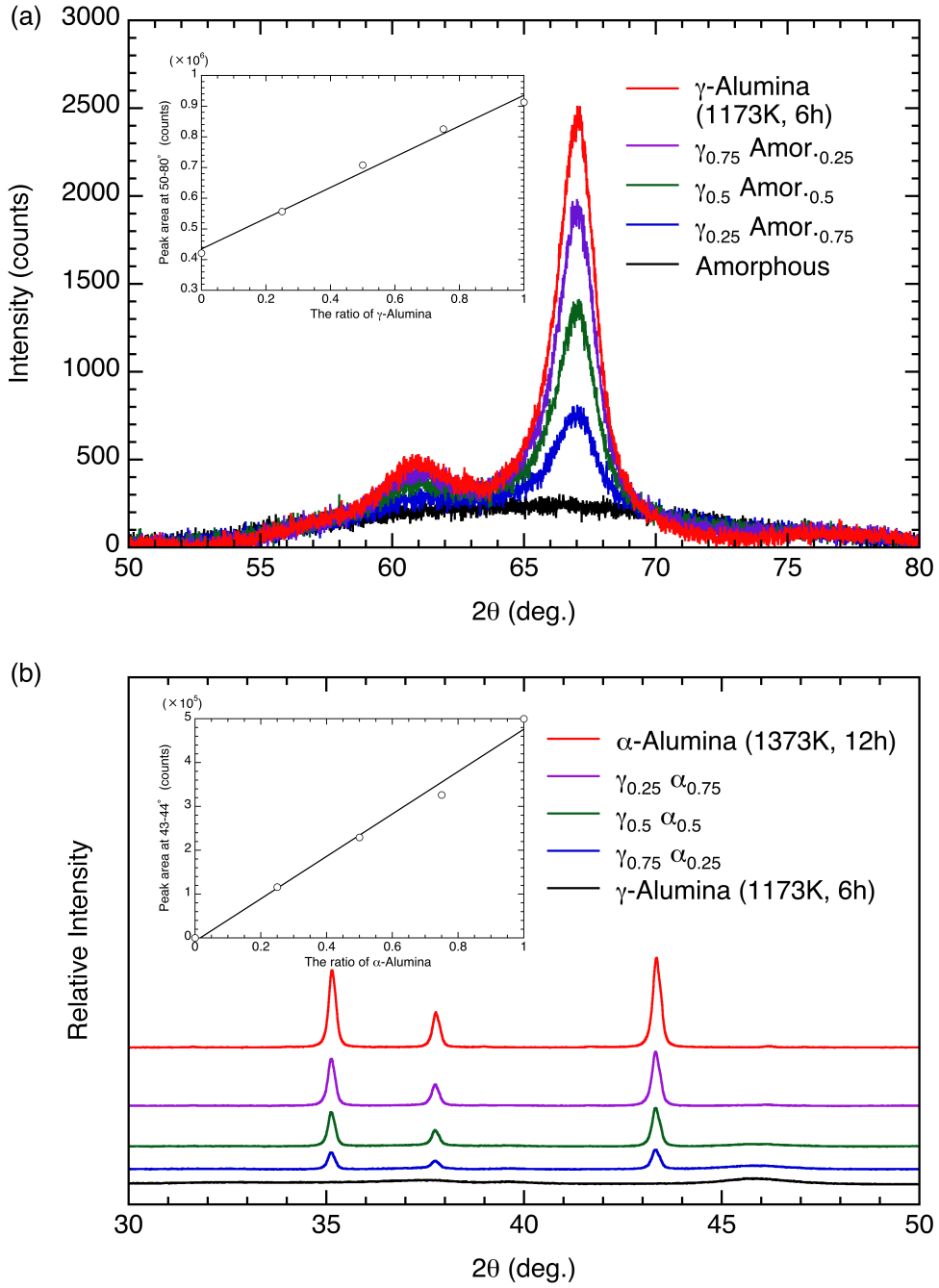

Fig. 3.8 (a) XRD patterns of γ-alumina, amorphous alumina, and mixed patterns of γ-alumina and amorphous alumina with the mass ratios of 0.25, 0.5, and 0.75. An inset is the relation between peak areas at 50–80° in 2θ of the XRD patterns and the mixing ratios. (b) XRD patterns of α-alumina, γ-alumina, and mixed patterns of α-alumina and γ-alumina references with the mass ratios of 0.25, 0.5, and 0.75. An inset shows the relation between peak areas of α-alumina at the range of 43–44° in 2θ and the mixing ratios.

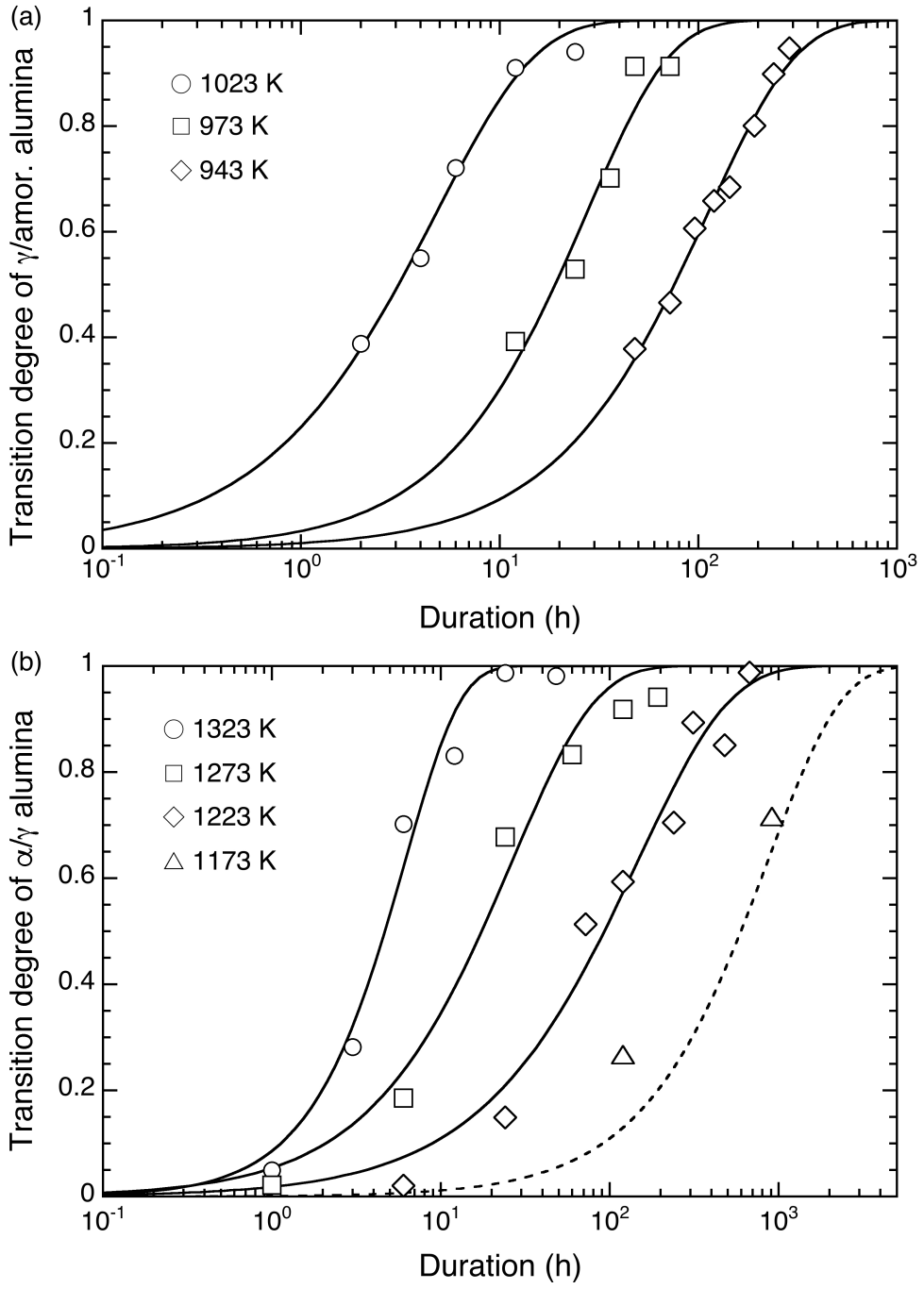

Fig. 3.9 Time evolution for crystallization degree from amorphous alumina into γ-alumina at 943, 973, and 1023 K (a), and the degree of γ-α phase transition at 1223, 1273, and 1323 K (b). Reaction degrees are estimated based on the relation between the peak areas in the XRD profiles and the mixing ratios as show in Fig. 3.8. The solid curves represent the best-fitted profiles calculated with JMA equation. Triangle symbols represent the degree of γ-α phase transition at 1173 K, and the dotted curve was derived using the JMA equation from the values of n=1 and τ obtained from the extrapolation of Arrhenius plots for the γ-α phase transition.

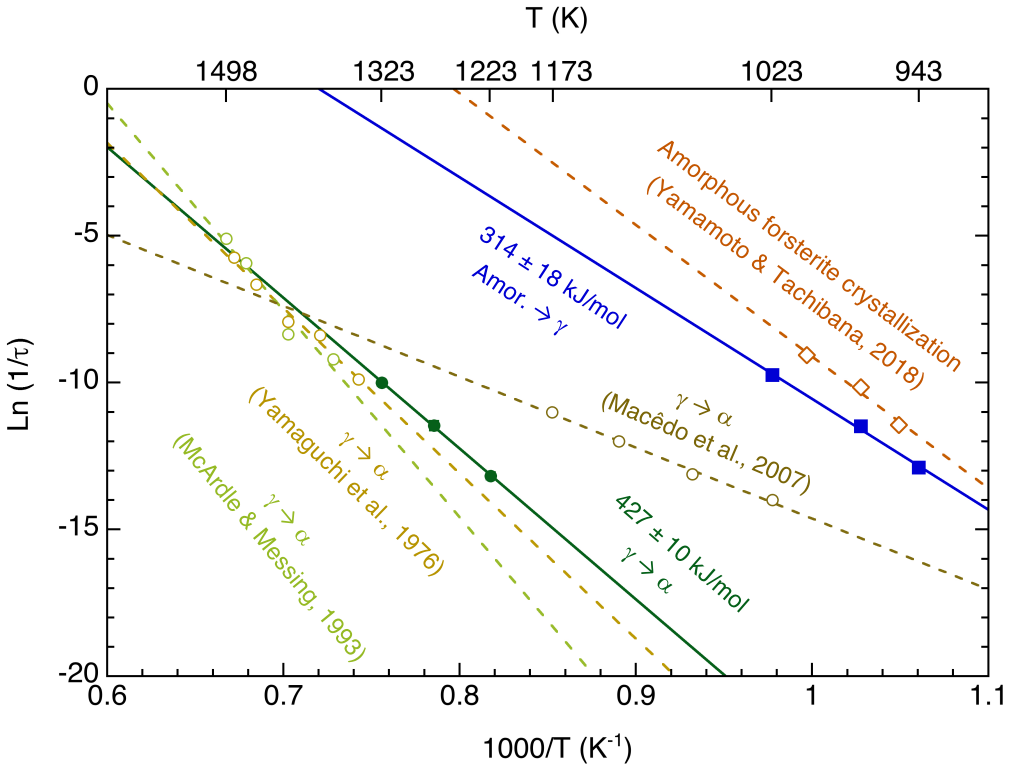

Fig. 3.10 The Arrhenius plots of the reciprocal time constant for crystallization from amorphous alumina (blue line) and γ-α phase transition (green line) in air. The Arrhenius relations for γ-α phase transition in previous studies and for crystallization of amorphous silicate with forsterite composition are shown as comparison. The errors of Ln ($1/\tau$) for the crystallization of amorphous alumina and the γ-α phase transition are within the Arrhenius plots.

4
Thermal Annealing of Amorphous Silicate and Amorphous/Transition Alumina Dusts in Circumstellar Environments

In this section, I applied crystallization and phase transition kinetics of amorphous enstatite and amorphous/γ-alumina dusts obtained in previous sections on in-situ annealing for the timescale of protoplanetary disks to investigate the effect of ambient gases on the crystallization of amorphous enstatite and temperature distributions for silicate and alumina dusts in protoplanetary disks.

Protoplanetary dusts incorporated from the interstellar medium are generally considered to migrate inward from the outer region of disks accompanying the evolution of accretion disks for the timescale of ~1–10 Myr (Pascucci & Tachibana, 2010). Accordingly, I also consider that crystallization and phase transition behaviors of amorphous silicate and alumina dusts in evolving protoplanetary disks to understand dust reaction under more realistic conditions. I obtained the temperatures of reaction lines T_{line} for the crystallization/phase transition from their activation energies E_{a} and frequency factors ν_0 using an equation estimated by comparison between a reaction timescale and a diffusive timescale of dust particles (Ishizaki et al., 2022);

$$T_{\mathrm{line}} = \frac{E_a}{R}\left[\ln(0.659\times10^6) - \frac{10}{9}\ln\left(\frac{\alpha}{10^{-2}}\right) + \frac{2}{9}\ln\left(\frac{\dot{M}}{10^{-7}\ \mathrm{M_{Sun}yr^{-1}}}\right) + 2\ln\left(\frac{\Delta r}{r}\right) + \ln\left(\frac{\nu_0}{\mathrm{day^{-1}}}\right)\right]^{-1} \quad (4)$$

where α is the alpha (α-) viscosity, and represents the gas viscosity parameter which determines the particle diffusion strength (Chen & Lin, 2020) and is considered to be in the range of ~10^{-5}–10^{-1} (e.g., Nakamoto & Nakagawa, 1994). $\dot{M}$ is the mass accretion rates typically understood to be in the range of 10^{-6}–10^{-9} $\mathrm{M_{Sun}yr^{-1}}$ for early stage of accretion disks (Fiorellino et al., 2021), and $\frac{\Delta r}{r}$ is the diffusive transport scale and takes the value of 0.03. The reaction line represents the highest temperature experienced by the dust when the chemical reactions have progressed to some extent, which could refer to whether silicate and alumina dusts found by infrared spectroscopic observations and in chondrite matrices have been beyond temperature boundaries for the reaction or not.

4.1 Implication for enstatite crystallization in protoplanetary disks

Here I focus on crystallization temperatures of amorphous silicate dusts and the effects of ambient gases on crystallization of amorphous enstatite in protoplanetary disks to be compared with infrared spectroscopic observations of the disks around young stars. The extrapolation of

obtained kinetics data to temperatures lower than the experimental temperature range (1053–1123 K) is required to discuss the crystallization for the long disk lifetime (~1–10 Myr). As I mentioned above, forsterite does not crystallize from the ITP synthesized amorphous enstatite in the low-temperature crystallization experiments at 993 K in air for the extended period of time (240 h) (Fig. 2.2b and 2.4b), which is inconsistent with the results using a sol-gel synthesized amorphous enstatite reported by Roskosz et al. (2011). This discrepancy would be attributed to the difference in the synthetic method of amorphous enstatite because the sol-gel synthesized amorphous enstatite would still contain water molecules and hydroxyls (-OH) in the amorphous structure that induces the forsterite crystallization from the amorphous enstatite at low temperatures. The observation that forsterite crystallized from amorphous enstatite under high water vapor pressures (P_{H2O} of 0.18 MPa) would support this conclusion. Because amorphous silicate dust in protoplanetary disks is considered to be mainly formed through non-equilibrium condensation from hot disk gas and/or irradiation of energetic ions such as supernova shock fronts on crystalline silicate dust (e.g., Brucato & Nuth, 2010), it is present as nominally anhydrous dust and the extrapolation of the experimental data obtained in section 2 to lower temperatures would be valid.

Figure 4.1 shows the e-folding timescale (i.e., timescale required for x~ 0.99) for crystallization of amorphous enstatite dust with the grain diameter of ~72 nm due to in situ heating at various ambient gas conditions as a function of temperature. Crystallization timescales of amorphous forsterite with the grain size of ~80 nm in diameter at P_{H2O} of 0.3 Pa, P_{H2O} of 1×10^{-4} Pa and P_{H2O} of 5×10^{2} Pa calculated based on the data taken from Yamamoto & Tachibana (2018) are shown for comparison. It is clearly seen that crystallization timescale of amorphous enstatite more strongly on temperature than the case of amorphous forsterite due to its much higher activation energy for crystallization (~727–951 kJ/mol) than that of amorphous forsterite (~254–414 kJ/mol). Crystallization of amorphous enstatite proceeds at higher temperatures compared with that of amorphous forsterite for the same heating duration and occurs in the regions at temperatures higher than ~900 K within the lifetime of protoplanetary disk gas (1–10 Myr) as suggested by a previous study (Murata et al., 2009; Imai, 2012). This suggests that crystalline enstatite dust can be only present in the inner region of the disks. While ambient gas pressure clearly affects the crystallization behavior at the experimental temperature range, in contrast with crystallization of amorphous forsterite (Yamamoto & Tachibana, 2018), its effect is not significantly large under the disk conditions because of very high values of activation energy for enstatite crystallization. In conclusion, the presence of crystalline enstatite dust can be a good proxy for the temperature that silicate dust experienced in protoplanetary disks.

Figure 4.2 shows the temperatures of reaction lines for crystallization of amorphous enstatite dust at various ambient gas conditions for the reaction degree of 99.99% as a function of α-viscosity for different steady mass accretion rates of 10^{-6}, 10^{-7}, and 10^{-8} $M_{Sun}yr^{-1}$ in a viscous accretion disk. The temperatures for crystallization of amorphous forsterite dust at P_{H2O} of 500 Pa, 0.3 Pa and 10^{-4} Pa in Yamamoto & Tachibana (2018) are also shown for comparison. The crystallization temperatures of amorphous enstatite differ by only ~20 K depending on ambient gas conditions, while crystallization of amorphous forsterite occurs at a wide temperature range of ~110 K at different water vaper pressures (Fig. 4.2). Both crystallization temperatures of amorphous enstatite and forsterite are almost unchanged within ~10 K at different mass accretion rates. I can see that crystalline enstatite and forsterite observed in protoplanetary disks could have experience at temperatures higher than ~950–1000 K and ~700–850 K, respectively, for the typical α-viscosity of 10^{-4}–10^{-2} (Rafikov, 2017).

van Boekel et al. (2004) estimated the fractional abundance of crystalline silicate grains to amorphous/crystalline silicates and amorphous silica observed from protoplanetary disks around three Herbig Ae stars, which indicates the crystallinity of ~40–95 % in the inner disks (1–2 au) and that of ~10–40 % in the outer disks (2–20 au). Although a relationship between the radial distance and temperatures from the central star strongly depends on adopted disk models and physical parameters such as a mass accretion rate and α-viscosity, the formation region for crystalline enstatite and forsterite through thermal annealing (~700–1000 K) could be correspond to inner region of disks (~1–2 au) with an accretion rate of 10^{-6} $M_{Sun}yr^{-1}$ and α-viscosity of 10^{-3} (Ida et al., 2016). Additionally, the dust distribution of crystalline enstatite (>950–1000 K) and forsterite (>700–850 K) would have influence on the decrease of relative abundance of enstatite to forsterite with lager radii of disks (Bouwman et al., 2008). The radial mixing in protoplanetary disks have been necessary to explain the presence of crystalline forsterite in the outer part of disks (Okamoto & Ida, 2022), but because crystalline enstatite has been not almost observed in these cold regions, thermal processes are required for a spatial variation of an enstatite/forsterite distribution. While condensation from fractionated Mg-Fe-poor gas could produce enstatite-rich dust in the inner surface of the disks, and account for the enstatite/forsterite distribution (Pignatale et al., 2014), an annealing process can be also a candidate to explain the crystallinity and dominant phase of silicate dusts in protoplanetary disks.

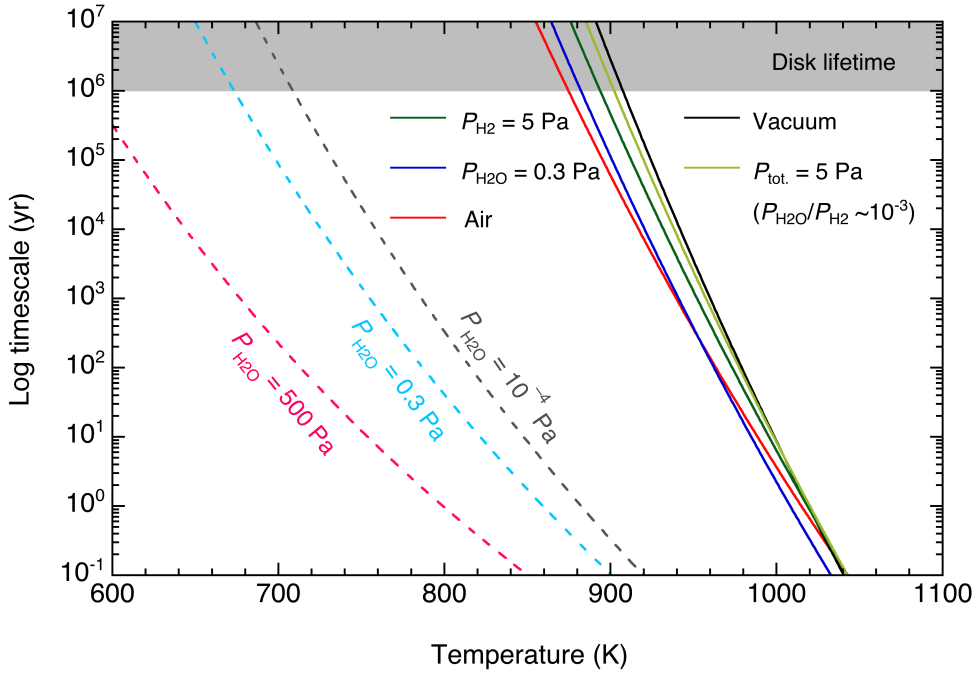

Fig. 4.1 E-folding timescales of in situ crystallization of ~72 nm-diameter amorphous enstatite dust in air (P_{H2O} ~10^{2} Pa), in vacuum (P_{H2O} ~10^{-4} Pa), at P_{H2O} of 0.3 Pa, at P_{H2} of 5 Pa and at $P_{tot.}$ of 5 Pa (P_{H2O}/P_{H2} ~10^{-3}). Timescales for crystallization of ~80 nm-diameter amorphous forsterite dust at P_{H2O} of 500 Pa, 0.3 Pa and 10^{-4} Pa in Yamamoto & Tachibana (2018) are also shown as comparison (dotted lines). The shaded region represents the estimated lifetime of protoplanetary disk gas.

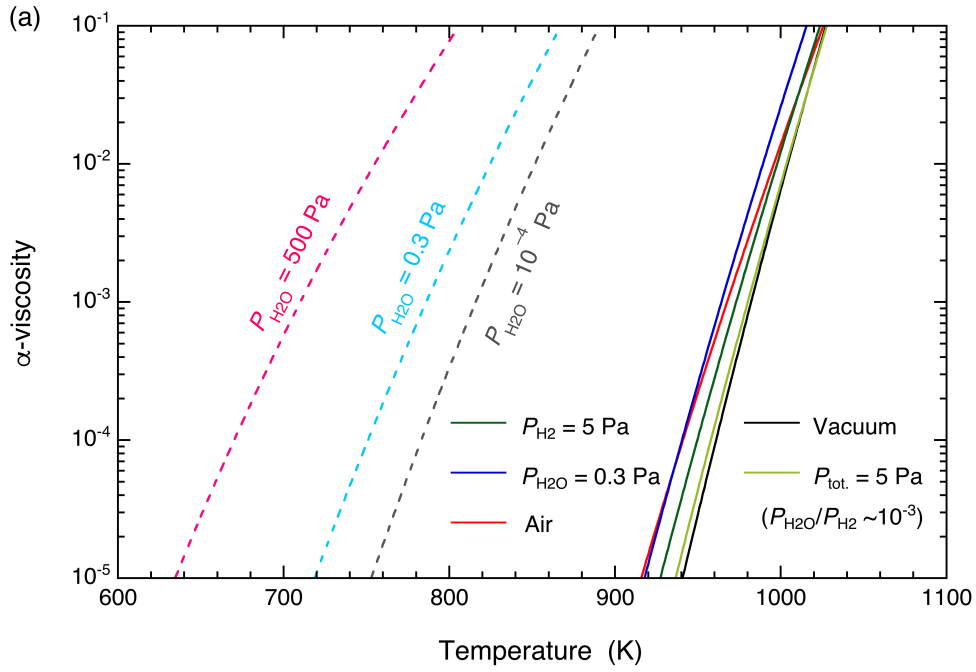

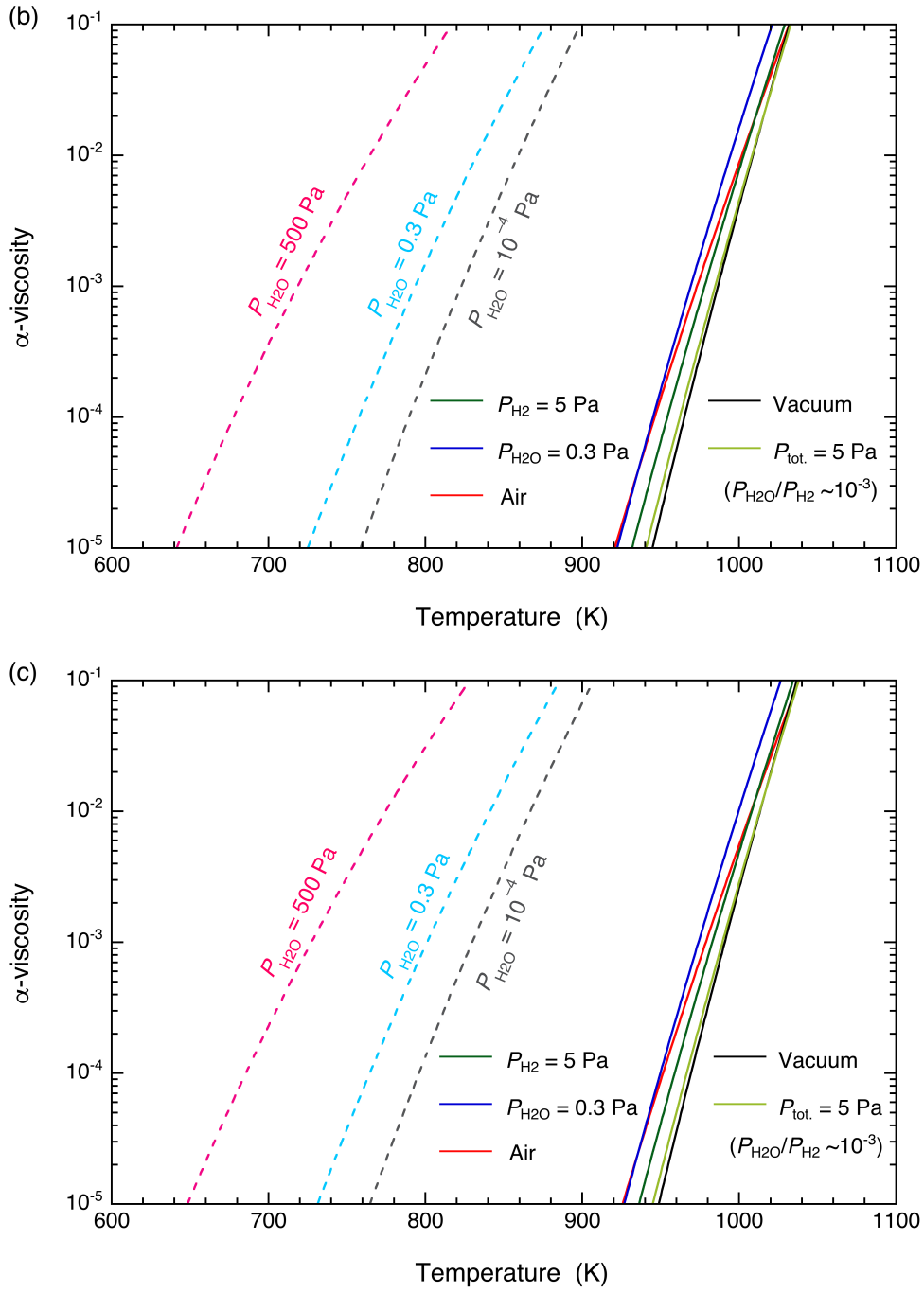

Fig. 4.2 Crystallization temperatures of amorphous enstatite dust in air (P_{H2O} ~10^2 Pa), in vacuum (P_{H2O} ~10^{-4} Pa), at P_{H2O} of 0.3 Pa, at P_{H2} of 5 Pa and at $P_{tot.}$ of 5 Pa (P_{H2O}/P_{H2} ~10^{-3}) as a function of α-viscosity, which were calculated using an equation derived from Ishizaki et al. (2022) for mass accretion rates of 10^{-6}, 10^{-7}, and 10^{-8} $M_{Sun}yr^{-1}$ (a~c; solid lines). The temperatures for crystallization of amorphous forsterite dust at P_{H2O} of 500 Pa, 0.3 Pa and 10^{-4} Pa in Yamamoto & Tachibana (2018) are also shown as comparison (dotted lines).

4.2 Implication for crystallization and phase transition of alumina dusts in protoplanetary disks and around evolved stars

Kinetics for crystallization of amorphous alumina and for phase transformation of transition alumina in protoplanetary disks has been poorly understood because these amorphous and transition alumina dusts are identified as minor phases in primitive meteorites (Stroud et al., 2004; Takigawa et al., 2014) and infrared spectroscopic observations around young stars do not strongly suggest the presence of these phases. However, it is also reported that amorphous and transition alumina are readily dissolved during acid treatments of meteorites (Takigawa et al., 2014). Therefore, it is unclear whether there could be a variety of presolar alumina phases not identified yet, or whether various alumina phases have existed in the protosolar disk, but such a variety could be lost by heating and/or isotopic homogenization in the disk. Here, I quantitatively evaluated the timescales for amorphous-γ and γ-α phase transitions in protoplanetary disks, which could help to understand the relative abundance of different alumina phases in chondrites due to thermal annealing in the disks and/or the chemical treatment of chondrites.

Figure 4.3 shows the e-folding timescale for crystallization of amorphous alumina and γ-α phase transition through in situ annealing as a function of temperature. Crystallization timescale of amorphous enstatite and forsterite dusts at P_{H2O} of 0.3 Pa as shown in Fig. 4.1 are shown for comparison. I found that crystallization of amorphous alumina dust occurred in almost the same timescale as that of amorphous forsterite in protoplanetary disks, and in the regions where the temperatures are higher than ~700 K, whereas the γ-α phase transition occurred only in the inner regions of disks at temperatures above ~900 K. This indicates that amorphous alumina can be present in a wide range of disk region at below ~700 K and γ-alumina can be present at temperatures ranging of 700–900 K. Alpha (α-) alumina dust can be formed at temperatures above ~ 900 K within the disk gas lifetime as in the case of crystalline enstatite, but γ-α phase transition would be more sluggish than crystallization of amorphous enstatite in the relatively short timescale (< 10^5 yr) due to the much higher activation energy for crystallization of amorphous enstatite compared with that for γ-α phase transition.

In an α-viscosity disk, the reaction lines for crystallization of amorphous alumina and γ-α phase transition are shown in Fig. 4.4. I can see that γ-alumina and crystalline forsterite have experienced the temperatures above ~750–850 K in protoplanetary disks, and crystalline enstatite and α-alumina have undergone the temperatures higher than ~950–1000 K and ~1000–1100 K, respectively, for α-viscosity of 10^{-4}–10^{-2}. These temperatures correspond with the timescale of ~1–10^3 yr required for crystallization of amorphous silicate and alumina dusts and the phase

transition of γ-alumina dust through in situ annealing at a constant temperature (Fig. 4.3). Crystallization and phase transition kinetics obtained from experimental results should be extrapolated to ~100–200 K lower temperatures to understand thermal evolutions for amorphous silicate and alumina dusts in accretion disks for α-viscosity of 10^{-4}–10^{-2}. Crystallization and phase transition temperatures for alumina dusts vary with mass accretion rates of 10^{-8}–10^{-6} $M_{Sun}yr^{-1}$ by only within ~20 K as is the similar case of crystallization of amorphous silicate dust.

Takigawa et al. (2014) reported that observations of amorphous and transition alumina particles in chondrites were much fewer than that of α-alumina particle because amorphous and transition alumina particles can be dissolved during the acid treatments to extract alumina grains from the meteorites. The timescales and reaction lines for the crystallization and phase transition in protoplanetary disks indicate that alumina dusts with the exception of α-alumina could survive below ~900–1100 K outside of the innermost regions in the disks, which could support the possible presence of the acid-soluble alumina phase in chondrites (Takigawa et al., 2014). Because amorphous and transition alumina dusts can be present extensively in the region of disks where amorphous silicate dust could exist, these grains could more abundantly survive in matrices of primitive chondrites.

Presolar alumina grains incorporated into the protosolar disk have been identified as origins from AGB stars and Supernovae (e.g., Choi et al., 1998; Nittler et al., 2008), and alumina dust is considered to be freshly formed around the evolved stars. The only alumina dust could be present around oxygen-rich AGB stars with low mass-loss rates, whereas those with higher mass-loss rates contain abundant silicates (Lorenz-Martins & Pompeia, 2000; Karovicova et al., 2013), which implies that alumina dust is a promising candidate to a first condensate around AGB stars. The ALMA observation of an oxygen-rich AGB star W Hydrae suggested that alumina dust was dominant in the dust shell near the star (2–3 R_{star}) because AlO molecules were present only at less than 3 R_{star} from the star, and matched with the dust distribution of aluminum oxide (Takigawa et al., 2017). The dust formation in the inner wind of an oxygen-rich Mira-type star IK Tau occurs through non-equilibrium processes induced by periodic shocks from the stellar pulsation (Gobrecht et al., 2016). The infrared observation of IK Tau indicates that its luminosity varies with a period of ~470 days (Wing & Lockwood, 1973) and the dust shells have been emitted at times separated by ~12 yr (Hale et al., 1997). The modeling for dust synthesis around IK Tau also represents that alumina grains could stay at ~2 R_{star} for 12 pulsations if alumina grains formed in the first oscillation are not destroyed by the periodic shocks at each shock passage (Gobrecht et al., 2016). The dynamical model for oxygen-rich AGB stars indicates that almost pure glassy

Al_2O_3 could exist near the inner radius (1.5–2 R_{star}) where the gas is cold at 700–900 K (Woitk, 2006). Therefore, I assumed the case that amorphous alumina dust formed by non-equilibrium condensation at close to the stars is present at the temperature range of 700–900 K for the timescale of 0.1–10 yr. Crystallization of amorphous alumina and γ-α phase transition would occur at temperatures above ~800 and 1050 K, respectively (Fig. 4.3), around the evolved stars. Both amorphous alumina and γ-alumina can survive in the inner dust shell at the temperature of ~700–800 K and 800–900 K, respectively. On the other hand, the formation of α-alumina (corundum) dust through annealing process hardly occurs around the evolved stars and requires alumina dust to stay in warmer regions at the temperature above ~1050 K or for much longer timescales than 10^5 yr at the temperature of ~900 K. Thus, amorphous alumina and γ-alumina dusts surviving around the evolved stars are ejected into interstellar medium, and could be disk materials as presolar grains.

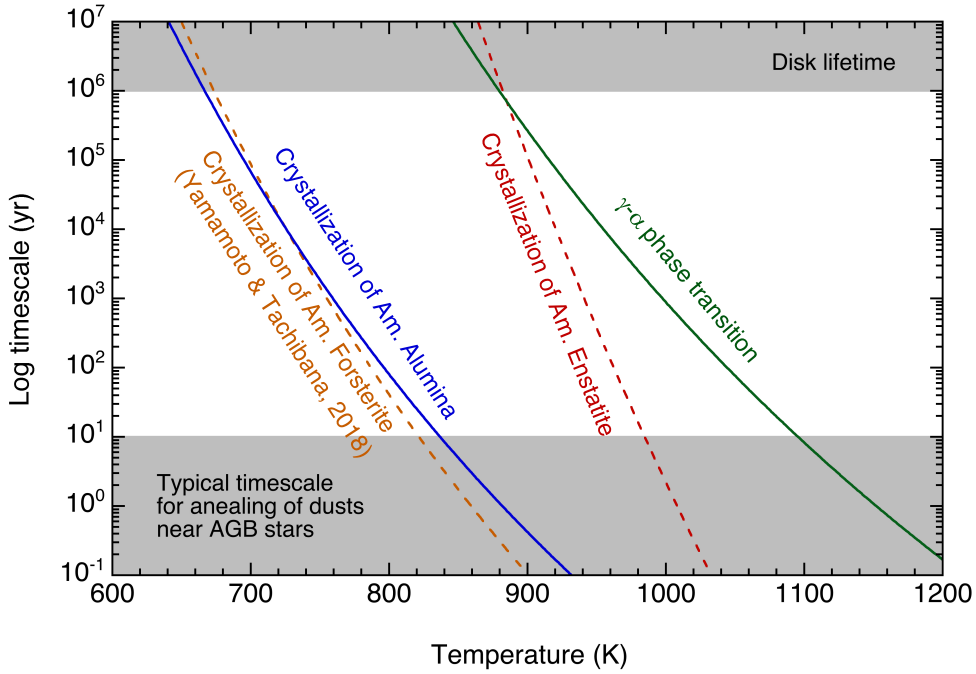

Fig. 4.3 E-folding timescales for in situ thermal evolutions of amorphous alumina and γ-alumina dusts with crystallization/phase transition degree of 0.99 in air (solid lines). Timescales for in situ crystallization of amorphous silicate dusts at P_{H2O} of 0.3 Pa with crystallization degree of 0.99 are shown as comparison (dotted lines). Upper and bottom shaded regions represent the estimated lifetime of protoplanetary disk gas (1–10 Myr) and a typical timescale (0.1–10 yr) for thermal annealing of dusts near AGB stars.

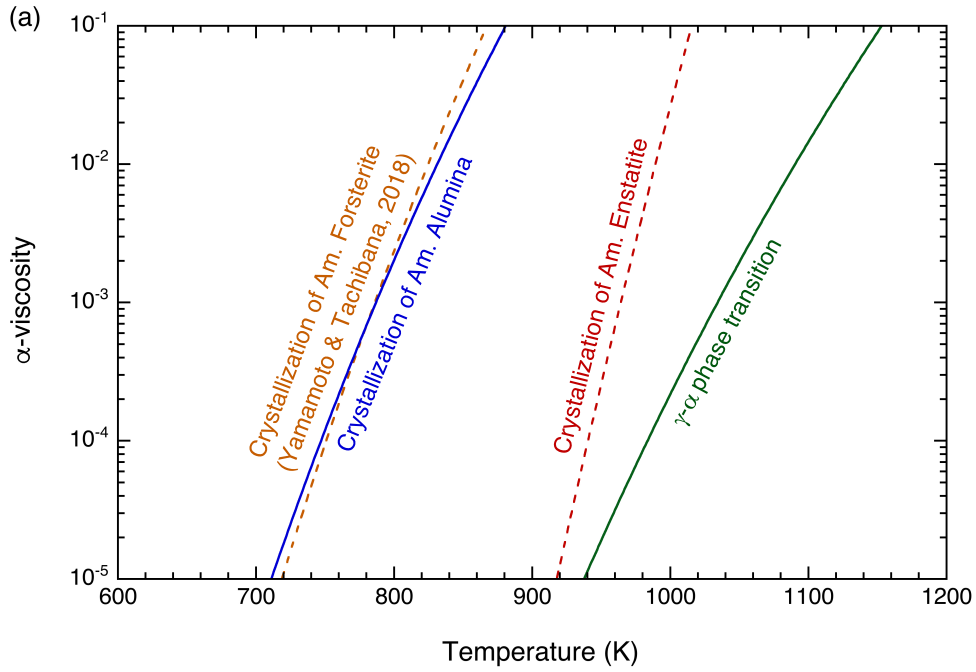
(a)
α-viscosity
Temperature (K)
Crystallization of Am. Forsterite
(Yamamoto & Tachibana, 2018)
Crystallization of Am. Alumina
Crystallization of Am. Enstatite
γ-α phase transition

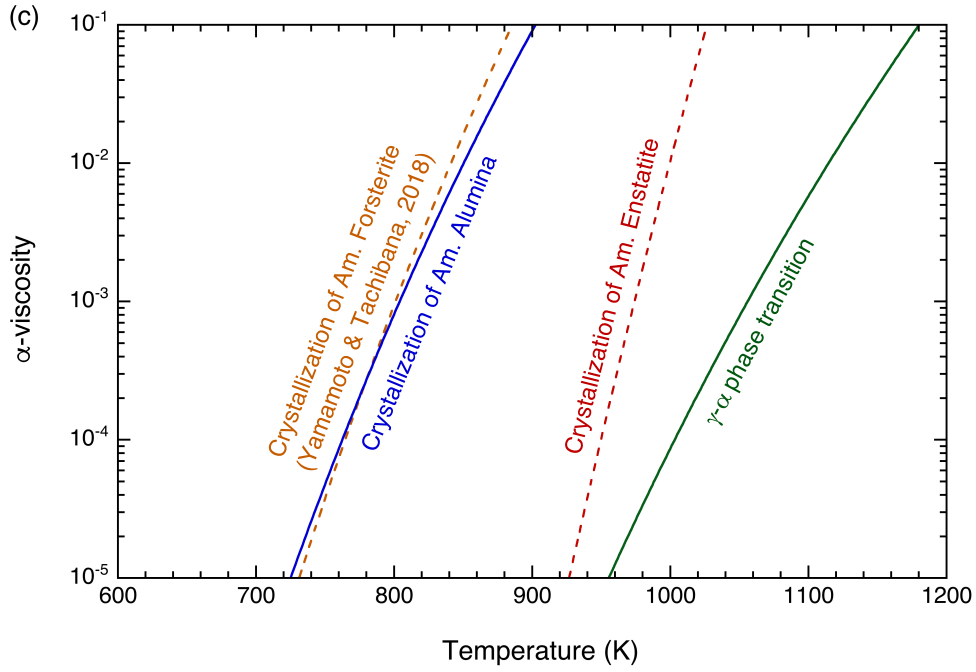
(c)
α-viscosity
Temperature (K)
Crystallization of Am. Forsterite
(Yamamoto & Tachibana, 2018)
Crystallization of Am. Alumina
Crystallization of Am. Enstatite
γ-α phase transition

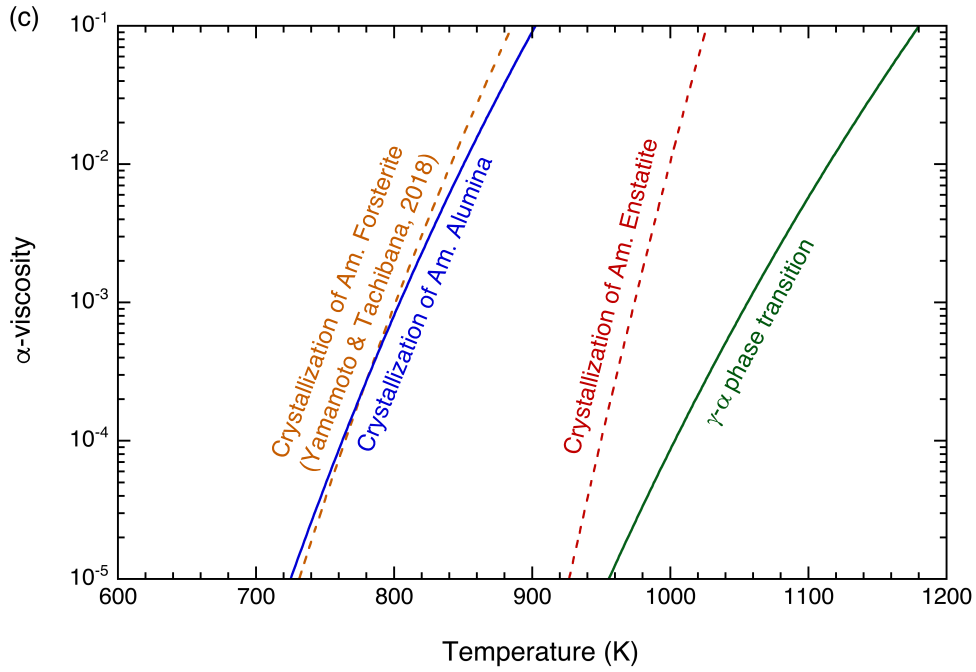

Fig. 4.4 Crystallization and phase transition temperatures of amorphous alumina and γ-alumina dusts as a function of α-viscosity, which were calculated using an equation derived from Ishizaki et al. (2022) for mass accretion rates of 10^{-6}, 10^{-7}, and 10^{-8} $M_{Sun}yr^{-1}$ (a~c; solid lines). The temperatures for crystallization of amorphous silicate dusts at P_{H2O} of 0.3 Pa are also shown as comparison (dotted lines).

4.3 Implication for survivability of presolar/solar silicate and alumina grains in pristine chondrites

Presolar grains such as amorphous silicates and aluminas formed around evolved stars and incorporated into the protosolar disk as discussed in section 4.2 would experience oxygen isotopic exchange, resulting in the disappearance of presolar isotopic signatures (Yamamoto et al., 2018, 2020). The relative kinetics of oxygen isotopic exchange to crystallization and phase transition of presolar amorphous alumina and γ-alumina dusts would determine the survivability of presolar dusts and the temperature regions where presolar or solar alumina dusts could exist in the protosolar disk, which could help to understand presolar and solar alumina phases found in chondrites during the chemical treatment.

Figure 4.5 describes reaction temperatures for crystallization of amorphous silicate and alumina dusts, and γ-α phase transition as shown in Fig. 4.4, and temperatures of reaction lines for oxygen isotopic exchange of amorphous silicate dusts with forsterite and enstatite compositions and of amorphous alumina and γ-alumina dusts estimated from oxygen diffusion

data (Yamamoto et al., 2018, 2020; Nabatame et al., 2003; Prot & Monty, 1996) are shown for comparison. I found that crystallization and phase transition temperatures of amorphous silicate and alumina dusts did not vary with a degree of particle diffusion in the disk (α-viscosity) as much as the temperatures for oxygen isotopic exchanges of these dusts because the relative values of frequency factors to activation energies for the crystallization and phase transition were much higher than their oxygen isotopic exchanges.

Crystalline enstatite is a product formed at the highest temperature through the crystallization of amorphous silicates with different chemical compositions. Amorphous silicate grains observed in primitive chondrites indicate that they would not experience thermal annealing process at least above ~1000 K. The matrices of highly pristine meteorites such as carbonaceous chondrites ALH A77397, MET 00426 and QUE 99177 consist of abundant solar amorphous silicate grains and some crystalline silicates (e.g., Abreu & Brealey, 2010), and are largely considered to be formed near the chondrule formation regions (Scott & Krot, 2005). Although various components in primitive chondrites are considered to be mixed by radial transport of the materials from diverse sources of the protosolar disk (e.g., Scott, 2007), most silicate dusts observed in chondrite matrices could be formed by non-equilibrium condensation from a nebular gas (~1000 K; Gail & Sedlmayr, 1999) and/or through oxygen isotopic exchanges of presolar silicate dusts incorporated from the interstellar medium (~600–800 K; Yamamoto et al., 2018, 2020), and would need to stay close to the regions where crystallization of amorphous silicates barely occurs (~750–1000 K).

The temperatures of reaction lines for oxygen isotopic exchange of alumina dusts for an accretion rate of 10^{-6} $M_{Sun}yr^{-1}$ derived from oxygen diffusion data in Nabatame et al. (2003) indicate that presolar grains with amorphous alumina and γ-alumina phases could transform into solar alumina grains at the temperatures higher than ~600–700 K and ~800–1100 K, respectively. Compared the crystallization and phase transition lines with the oxygen isotopic exchange lines, oxygen isotopic exchanges of amorphous alumina and γ-alumina mainly occurs at lower temperatures than their crystallization and phase transition, which indicates that presolar amorphous and γ-alumina dusts incorporated in the protosolar disk would not almost transform into γ-alumina and α-alumina, respectively, without the oxygen isotopic exchange. These could compatibly explain that the amount of presolar corundum is much smaller than that of solar corundum in primitive chondrites (e.g., Takigawa et al., 2014). On the other hand, in a part of a region for α-viscosity of close to 10^{-2}, the relation of reaction lines for γ-α phase transition and oxygen isotopic exchange of γ-alumina is reversed and presolar γ-alumina could transforms into

α-alumina at temperatures above ~1100 K without oxygen isotopic exchange of γ-alumina. While both reaction lines for crystallization/phase transition and oxygen isotopic exchange are shifted to high temperatures for only several tens of degree kelvin with decreasing accretion rates from 10^{-6} to 10^{-8} $M_{Sun}yr^{-1}$, a relatively large degree of line shift for oxygen isotopic exchange of γ-alumina to γ-α phase transition produces broader regions for the transformation from presolar γ-alumina to presolar α-alumina with α-viscosity of (0.3–1) × 10^{-2} for an accretion rate of 10^{-8} $M_{Sun}yr^{-1}$. Presolar α-alumina dust initially incorporated as interstellar dusts and transformed from presolar γ-alumina in these regions would survive thermal processes at least lower than ~1500 K (Prot & Monty, 1996) in the disk, and could contribute to a small amount of presolar corundum observed in primitive chondrites (e.g., Stroud et al., 2004; Nittler et al., 2008).

It has been noted that presolar silicate grains are preferentially lost their isotopic signatures through disk thermal processing or thermal/aqueous alteration on the meteorite parent bodies (Floss & Haenecour, 2016) because the relative abundances of presolar silicate to oxide grains in the CR2 chondrite NWA 852 (Leitner et al., 2012a) and the ungrouped carbonaceous chondrite Adelaide (Floss & Standermann, 2012) are much lower than those calculated for AGB stars (Leitner et al., 2012a) and observed in the most pristine carbonaceous chondrites (e.g., Floss & Standermann, 2009). The kinetic data from experimental results represent that the sequences and temperature regions where oxygen isotopic exchange and crystallization/phase transition of alumina dusts occur in the disk are similar to those of amorphous silicates, resulting that both presolar amorphous silicate and most presolar alumina dusts would experience the oxygen isotopic exchange at the almost same temperature range, and transform into solar dusts except for the possibility that presolar corundum remains at high temperature regions below ~1500 K under particular disk conditions. Therefore, assuming that presolar oxide dusts are almost presolar alumina, presolar silicate and oxide dusts could be almost equally lost their isotopic signatures thorough thermal annealing of the protosolar disk.

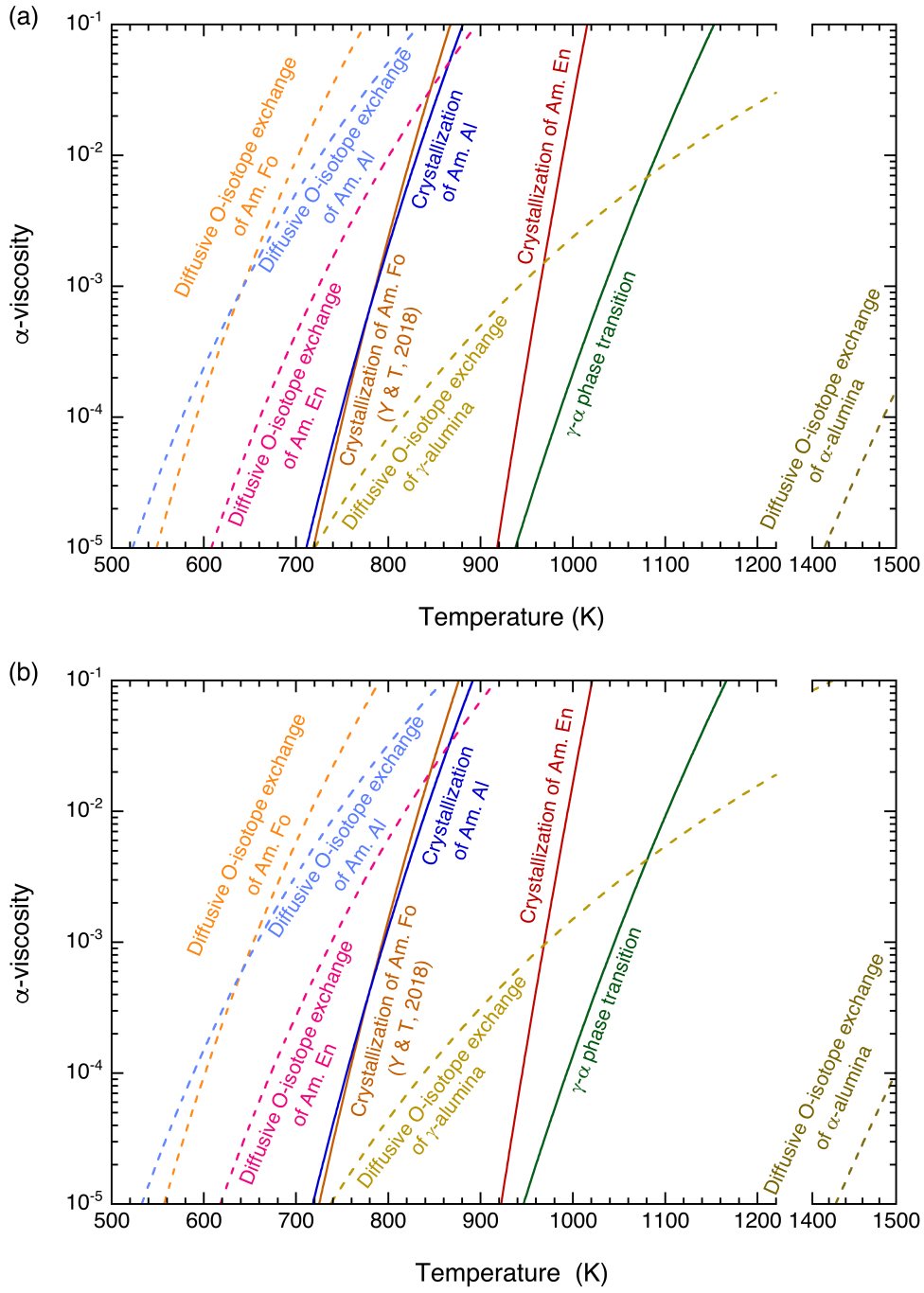
(a)
α-viscosity
Temperature (K)
Diffusive O-isotope exchange of Am. Fo
Diffusive O-isotope exchange of Am. Al
Diffusive O-isotope exchange of Am. En
Crystallization of Am. Fo (Y & T, 2018)
Crystallization of Am. Al
Diffusive O-isotope exchange of γ-alumina
Crystallization of Am. En
γ-α phase transition
Diffusive O-isotope exchange of α-alumina
(b)
α-viscosity
Temperature (K)
Diffusive O-isotope exchange of Am. Fo
Diffusive O-isotope exchange of Am. Al
Diffusive O-isotope exchange of Am. En
Crystallization of Am. Fo (Y & T, 2018)
Crystallization of Am. Al
Diffusive O-isotope exchange of γ-alumina
Crystallization of Am. En
γ-α phase transition
Diffusive O-isotope exchange of α-alumina

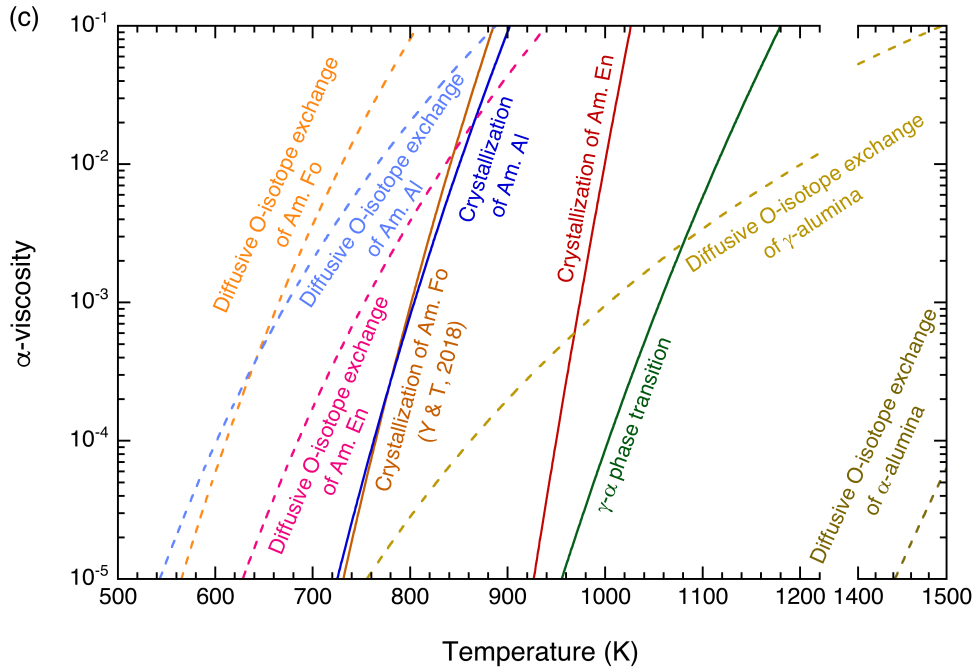

Fig. 4.5 Crystallization and phase transition temperatures of amorphous silicate and alumina dusts as a function of α-viscosity, which were calculated using an equation derived from Ishizaki et al. (2022) for accretion rates of 10^{-6}, 10^{-7}, and 10^{-8} $M_{Sun}yr^{-1}$ (a~c; solid lines). Temperatures required for oxygen isotopic exchange of amorphous silicate and alumina dusts (from oxygen diffusion data in Yamamoto et al., 2018, 2020; Nabatame et al., 2003; Prot & Monty, 1996) are also shown as comparison (dotted lines).

5
Conclusions

I determined crystallization and phase transition kinetics of amorphous silicate and alumina dusts to investigate thermal evolutions for amorphous silicate and alumina dusts in the early stage of solar system formation. The purpose of this thesis is to obtain experimental data to constraint the temperatures where silicate dust with enstatite composition and alumina dusts have experienced in protoplanetary disks, which would give an interpret for astronomical observations of the disks around young stars and for crystalline/amorphous silicate and alumina grains found in pristine chondrite matrices.

In section 2, I conducted crystallization experiments of amorphous silicate with enstatite composition (Mg/Si ~1) under the presence of water vapor and hydrogen gas to evaluate the effects of ambient gases on the crystallization kinetics. I obtained the activation energies ranged from 727 to 951 kJ/mol at each ambient gas pressure, and found that the activation energy for crystallization of amorphous enstatite decreased with increasing water vapor pressure as in the case of crystallization of amorphous forsterite (Yamamoto & Tachibana, 2018). While hydrogen gas has a small effect on crystallization of amorphous enstatite, the crystallization rates become larger with decreasing total pressures at the experimental temperature range. Crystallization at P_{H2O} of 0.18 MPa indicated that amorphous enstatite could transform into forsterite for the first crystalline phase under a very high pressure of water vapor, which could induce crystallization of amorphous enstatite at lower temperatures (973–993 K). However, I consider that forsterite does not crystallize from amorphous silicate with enstatite composition at the disk condition because protoplanetary dusts are present as anhydrous dusts and water vapor pressures in the disks are considered to be low (~$0.1–10^{-4}$ Pa) from the estimation of solar abundance ratio of H_2O/H_2.

In section 3, I conducted crystallization and phase transition experiments of amorphous alumina and γ-alumina in air to determine the kinetics for phase transformations of alumina dusts in protoplanetary disks. I obtained the activation energy of 314 ± 18 kJ/mol for crystallization of amorphous alumina. This crystallization kinetics of amorphous alumina is very consistent with that of forsterite at P_{H2O} of 0.3 Pa (Yamamoto & Tachibana 2018). Although a wide range of the activation energies of ~200–600 kJ/mol for transformation from γ-alumina to α-alumina have been reported (e.g., McArdle & Messing, 1993), I determined the activation energy of 427 ± 10 kJ/mol for the phase transition. The Arrhenius relations for crystallization of amorphous alumina

and γ-α phase transition indicated that amorphous alumina transformed into α-alumina through γ-alumina, one of the metastable phase of aluminum oxides, at all temperature conditions. The kinetics for γ-α phase transition was quantitatively estimated from phase transition experiments at lower temperatures of 1223–1323 K than previous studies, resulting that the extrapolation of Arrhenius relation in the present study to higher temperatures could fit well to Arrhenius plots in Yamaguchi et al. (1976) and McArdle & Messing (1993).

In section 4, I evaluated the timescales for in situ crystallization and phase transition of amorphous silicate and alumina dusts in the inner regions of protoplanetary disks and for thermal annealing of alumina dusts around the evolved stars. Although I can see different crystallization behaviors of amorphous enstatite under various ambient gas pressures at the experimental temperature range, the effects of ambient gases on the crystallization in protoplanetary disks are small because the activation energies for crystallization of amorphous enstatite take very high values. Crystalline enstatite dust would be present in the only regions of disks at temperatures higher than ~900 K irrespective of disk atmospheres, and consequently can be a good thermo-recorder for inner regions of disks. Crystallization of amorphous alumina occurs at temperatures above ~700 K and γ-alumina transforms into α-alumina at temperatures higher than ~900 K for the disk timescale (~1–10 Myr). Therefore, amorphous alumina and γ-alumina dusts could be present outside of the innermost region at temperatures less than ~900 K, which implies that alumina dusts except for corundum (α-alumina) could sufficiently survive thermal processes of protoplanetary disks as in the case of amorphous silicates. This would support the possible presence of the acid-soluble alumina phases in chondrites (Takigawa et al., 2014). On the other hand, around oxygen-rich AGB stars, both amorphous alumina and γ-alumina can survive in the inner dust shell at temperatures of ~700–800 K and 800–900 K, respectively while α-alumina (corundum) dust could not be produced through annealing process for the typical timescale of several periodic shocks (0.1–10 yr).

I also discussed the temperatures of reaction lines for crystallization and phase transition of amorphous silicate and alumina dusts in evolving protoplanetary disks for typical α-viscosity of 10^{-4}–10^{-2} and mass accretion rates of 10^{-8}–10^{-6} $M_{Sun}yr^{-1}$ using an equation calculated by Isizaki et al. (2022) to understand dust reaction under more realistic conditions. Crystallization of amorphous enstatite and alumina, and γ-α phase transition occur at temperatures above ~750–850 K, ~950–1000 K, and ~1000–1100 K in accretion disks, which are slightly higher than the temperatures estimated from the disk timescale of 1–10 Myr without an inward migration because the crystallization and phase transition would occur for relatively early stage (~1–10^3 yr)

of the disk timescale. The relation of crystallization/phase transition lines and oxygen isotopic exchange lines (Yamamoto et al., 2018, 2020; Nabatame et al., 2003) indicated that presolar amorphous and γ-alumina dusts incorporated in the protosolar disk would not almost transform into γ-alumina and α-alumina, respectively without the oxygen isotopic exchange. This could support that the amount of presolar corundum is much smaller than that of solar corundum in primitive chondrites (Takigawa et al., 2014). Comparing thermal evolution of presolar alumina dusts with that of presolar amorphous silicates in the protosolar disk, they would lose their isotopic signatures and transform into solar dusts at the similar temperature regions of the disk.

Thus, I consider that crystallization and phase transition kinetics for amorphous silicate and alumina dusts would provide a clue as to thermal annealing processes in protoplanetary disks around young stars and around evolved stars. On the other hand, because alumina dust is less abundant than silicate dust and has been not almost observed in the interstellar medium and protoplanetary disks, it would be necessary to carefully observe alumina grains in meteorites and to investigate the formation and thermal evolution of alumina dust around evolved stars in more detail, which would help to understand the thermal evolution of alumina dust in protoplanetary disks. Additionally, if the astronomical observation of less abundant dusts such as refractory oxides is made possible through further improvements of the observation technology, protoplanetary dusts other than silicate dust could directly contribute to an understanding of material evolutions for planetary formation in the early solar system.

Acknowledgements

This Ph.D thesis benefited from many people who have contributed to this thesis directly or have provided helpful advice and suggestions.

Above all, I would like to express my gratitude to Professor Hisayoshi Yurimoto (Hokkaido University), Professor Shogo Tachibana (University of Tokyo), and Dr. Daiki Yamamoto (Kyushu University) for giving me a great opportunity to realize such a study and helpful and continuous suggestions and comments. I also would like to express my gratitude to Dr. Aki Takigawa (University of Tokyo) for TEM observation and analysis of samples and related helpful suggestions and comments, and for kindly providing alumina gel.

I am grateful to Mr. Hideto Yoshida (University of Tokyo) for SEM observation of samples and related helpful suggestions and comments. I am also grateful to Professor Akira Tsuchiyama and Dr. Junya Matsuno for kindly providing amorphous silicate powder. I would like to thank Dr. Yuki Kimura (Hokkaido University) for TEM observation and analysis of samples and related helpful suggestions and comments. I also would like to thank Professor Takaya Nagai, Dr. Naoya Sakamoto, Dr. Kenichi Bajo, and Dr. Noriyuki Kawasaki (Hokkaido University) for insightful comments and suggestions.

Finally, I wish to give my thanks to all other staffs and students in the Geochemistry group in Hokkaido University and University of Tokyo. They were always giving me helpful support and advice.

References

- Abreu, N. M., and Brearley, A. J. (2010) Early solar system processes recorded in the matrices of two highly pristine CR3 carbonaceous chondrites, MET 00426 and QUE 99177, *Geochimica et Cosmochimica Acta*, 74, 1146–1171

- Avrami, M. (1939) Kinetics of phase change. I General theory, *The Journal of Chemical Physics*, 7, 1103

- Bouwman, J., Meeus, G., de Koter, A., Hony, S., Dominik, C., and Waters, L. B. F. M. (2001) Processing of silicate dust grains in Herbig Ae/Be systems, *Astronomy and Astrophysics*, 375, 950–962

- Bouwman, J., Henning, Th., Hillenbrand, L. A., Meyer, M. R., Pascucci, I., Carpenter, J., Hines, D., Kim, J. S., Silverstone, M. D., Hollenbach, D., and Wolf, S. (2008) The formation and evolution of evolution of planetary systems: Grain growth and chemical processing of dust in T Tauri systems, *The Astrophysical Journal*, 421, 640–650, 683, 479

- Brucato, J. R., Mennella, V., Colangeli, L., Rotundi, A., and Palumbo, P. (2002) Production and processing of silicates in laboratory and in space, *Planetary and Space Science*, 50, 829

- Brucato, J. R., and Nuth, J. A. (2010) Laboratory studies of simple dust analogs in astrophysical environments, *in Protoplanetary dust*: *Astrophysical and Cosmochemical Perspectives*, ed. D. Apai and D. S. Lauretta (New York: Cambridge Univ. Press), 128

- Chihara, H., Koike, C., and Tsuchiyama, A. (2001) Low-temperature optical properties of silicate particles in the far-infrared region, *Publications of the Astronomical Society of Japan*, 53, 2, 243–250

- Chihara, H., Koike, C., Tsuchiyama, A., Tachibana, S., and Sakamoto, D. (2002) Compositional dependence of infrared absorption spectra of crystalline silicates, I. Mg–Fe pyroxenes, *Astronomy and Astrophysics*, 391, 267–273

- Chen, K., and Lin, M. (2020) How efficient is the streaming instability in viscous protoplanetary disks? *The Astrophysical Journal*, 891, 132–154

- Choi, B., Huss, G. R., Wasserburg. G. J., and Gallino, R. (1998) Presolar corundum and spinel in ordinary chondrites: Origins from AGB stars and a supernova, *Science*, 282, 1284

- Christian, J. W. (2002) The theory of transformations in metals and alloys, *Pergamon Press*, 3rd ed., Oxford, U. K

- Dell'Agli, F., Garcia-Hernandez, D. A., Rossi, C., Ventura, P., Di Criscienzo, M., and Schneider, R. (2014) On the alumina dust production in the winds of O-rich Asymptotic Giant Branch stars, *Monthly Notices of the Royal Astronomical Society*, 441, 1115–1125

- Demyk, K., Carrez, Ph., Leroux, H., Cordier, P., Jones, A. P., Borg, J., Quirico, E., Raynal, P. I., and d'Hendecourt, L. (2001) Structural and chemical alteration of crystalline olivine under low energy He^+ irradiation, *Astronomy and Astrophysics*, 368, L38–L41

- Djouadi, Z., D'Hendecourt, L., Leroux, H., Jones, A. P., Borg, J., Deboffle, D., and Chauvin, N. (2005) First determination of the (re)crystallization activation energy of an irradiated olivine-type silicate, *Astronomy and Astrophysics*, 440, 179–184

- Dorschner, J., Begemann, B., Henning, Th., Jäger, C., Mutschke, H. (1995) Steps toward interstellar silicate mineralogy. II. Study of Mg-Fe-silicate glasses of variable composition, *Astronomy and Astrophysics*, 300, 503–520

- Fabian, D., Jäger, C., Henning, Th., Dorschner, J., and Mutschke, H. (2000) Steps toward interstellar silicate mineralogy V. Thermal evolution of amorphous magnesium silicates and silica, *Astronomy and Astrophysics*, 364, 282

- Feistel, R., and Wagner, W. (2007) Sublimation pressure and sublimation enthalpy of H_2O ice Ih between 0 and 273.16 K, *Geochimica et Cosmochimica Acta*, 71, 36–45

- Fiorellino, E., Manara, C. F., Nisini, B., Ramsay, S., Antoniucci, S., Giannini, T., Biazzo, K., Alcala, J., and Fedele, D. (2021) KMOS study of the mass accretion rate from Class I to Class II in NGC 1333, *Astronomy and Astrophysics*, 650, A43

- Floss, C., and Stadermann, F. (2009) Auger nanoprobe analysis of presolar ferromagnesian silicate grains from primitive CR chondrites QUE 99177 and MET 00426, *Geochimica et Cosmochimica Acta*, 73, 2415–2440

- Floss, C., and Standermann, F. J. (2012) Presolar silicate and oxide abundances and compositions in the ungrouped carbonaceous chondrite Adelaide and the K chondrite Kakangari: The effects of secondary processing, *Meteoritics and Planetary Science*, 47, 6, 992–1009

- Floss, C., and Haenecour, P. (2016) Presolar silicate grains: Abundances, isotopic and elemental compositions, and the effects of secondary processing, *Geochemical Journal*, 50, 3–25

- Gail, H.-P., and Sedlmayr, E. (1999) Mineral formation in stellar winds: I. Condensation sequence of silicate and iron grains in stationary oxygen rich outflows, *Astronomy and Astrophysics*, 347, 594–616

- Gobrecht, D., Cherchne, I., Sarangi, A., Plane, J. M. C., and Bromley, S. T. (2016) Dust formation in the oxygen-rich AGB star IK Tauri, *Astronomy and Astrophysics*, 585, A6

- Hale, D. D. S., Bester, M., Danchi, W. C., Hoss, S., Lipman, E., Monnier, J. D., Tuthill, P. G., Townes, C. H., Johnson, M., Lopez, B., and Geballe, T. R. (1997) Multiple dust shells and motions around IK Tauri as seen by infrared interferometry, *The Astrophysical Journal*, 490, 407–411

- Hallenbeck, S. L., Nuth, J. A., and Daukantas, P. L. (1998) Mid-infrared spectral evolution of amorphous magnesium silicate smokes annealed in vacuum: Comparison to cometary spectra, *Icarus*, 131, 198–209

- Henning, Th., Begemann, B., Mutschke, H., and Dorschner, J. (1995) Optical properties of oxide dust grains, *Astronomy and Astrophysics Supplement*, 112, 143–149

- Henning, Th. (2010) Cosmic Silicate, *Annual Review Astronomy and Astrophysics*, 48, 21–46

- Ida, S., Guillot, T., and Morbidelli, A. (2016) The radial dependence of pebble accretion rates: A source of diversity in planetary systems I. Analytical formulation, *Astronomy and Astrophysics*, 591, A72

- Imai, Y. (2012) Experimental study of circumstellar silicate dust evolution by crystallization processes using laboratory infrared spectroscopy, *PhD thesis*

- Ishizaki, L., Tachibana, S., Ida, S., Okamoto, T., and Yamamoto, D. (2022) Oxygen isotope exchange and crystallization of amorphous silicate dust in protoplanetary disks: 3D Monte Carlo simulation, *The 85th Annual Meeting of The Meteoritical Society 2022*, Abstract 6183

- Jackson, K. A. (2004) Kinetic Processes: Crystal growth, diffusion, and phase transitions in materials*, Arizona Materials Laboratory Department of Materials Science and Engineering*

- Jäger, C., Dorschner, J., Mutschke, H., Posch, Th., Henning, Th. (2003) Steps toward interstellar silicate mineralogy. VII. Spectral properties and crystallization behavior of magnesium silicates produced by the sol-gel method, *Astronomy and Astrophysics*, 408, 193–204

- Johnson, W. A., and Mehl, R. F. (1939) Reaction kinetics in processes of nucleation and growth, *Transactions of the American Institute of Mining and Metallurgical Engineers*, 135, 416

- Kaito, C., Miyazaki, Y., Kumamoto, A., and Kimura, Y. (2007) Exothermic chemical reactions can drive nonthermal crystallization of amorphous silicate grains, *The Astrophysical Journal*, 666, L57–L60

- Karovicova, I., Wittkowski, M., Ohnaka, K., Boboltz, D. A., Fossat, E., and Scholz, M. (2013) New insights into the dust formation of oxygen-rich AGB stars, *Astronomy and Astrophysics*, 560, A75

- Kim, T. H., Tsuchiyama, A., Takigawa, A., Matsuno, J., Enju, S., Kawano, H., and Komaki, H. (2021) Condensation of cometary silicate dust using an induction thermal plasma system I. Enstatite and CI chondritic composition, *Astronomy and Astrophysics*, 656, A42

- Kemper, F., Vriend, W. J., Tielens, A. G. G. M. (2004) The absence of crystalline silicates in the diffuse interstellar medium, *The Astrophysical Journal*, 609, 826

- Koike, C., Imai, Y., Chihara, H., Suto, H., Murata, K., Tsuchiyama, A., Tachibana, S., and Ohara, S. (2010) Effects of forsterite grain shape on infrared spectra, *The Astrophysical Journal*, 709, 983–992

- Kuroda, M., Tachibana, S., Sakamoto, N., Okumura, S., Nakamura, M., and Yurimoto, H. (2018) Water diffusion in silica glass through pathways formed by hydroxyls, *American Mineralogist*, 103, 412–417

- Kuroda, M., and Tachibana, S. (2019) Effect of structural dynamical property of melt on water diffusion in rhyolite melt, *ACS Earth and Space Chemistry*, 3, 2058

- Leitner, J., Vollmer, C., Hoppe, P., and Zipfel, J. (2012a) Characterization of presolar material in the CR chondrite Northwest Africa 852, *The Astrophysical Journal*, 745, 38

- Lodders, K. (2003) Solar system abundances and condensation temperatures of the elements, *The Astrophysical Journal*, 591, 1220–1247

- Lorenz-Martins, S., and Pompeia, L. (2000) Modelling of oxygen-rich envelopes using corundum and silicate grains, *Monthly Notices of the Royal Astronomical Society*, 315, 4, 856–864

- Levin, I., and Brandon, D. (1998) Metastable alumina polymorphs: Crystal structures and transition sequences, *Journal of the American Ceramic Society*, 81, 8, 1995–2012

- Macêdo, M. I. F., Bertran, C. A., and Osawa, C. C. (2007) Kinetics of the γ→α-alumina phase transformation by quantitative X-ray diffraction, *Journal of materials Science*, 42, 2830–2836

- Matsuno, J., Tsuchiyama, A., Watanabe, T., Tanaka, M., Takigawa, A., Enju, S., Koike, C., Chihara, H., and Miyake, A. (2021) Condensation of glass with multimetal nanoparticles: Implications for the formation process of GEMS grains, *The Astrophysical Journal*, 911, 47

- McArdle, J. L., and Messing, G. L. (1993) Transformation, microstructure development, and densification in α-Fe_2O_3-seeded boehmite-derived alumina, *Journal of the American Ceramic Society*, 76, 214–222

- Murata, K., Chihara, H., Koike, C., Takakura, T., Imai, Y., and Tsuchiyama, A., (2009) Crystallization experiments on amorphous magnesium silicate. I. Estimation of the activation energy of enstatite crystallization, *The Astrophysical Journal*, 697, 836–842

- Nabatame, T., Yasuda, T., Nishizawa, M., Ikeda, M., Horikawa, T., and Toriumi, A. (2003) Comparative studies on oxygen diffusion coefficients for amorphous and -Al_2O_3 films using ^{18}O isotope, *Japanese Journal of Applied Physics*, 42, 7205–7208

- Nakamoto and Nakagawa (1994) Formation, early evolution, and gravitational stability of protoplanetary disks, *The Astrophysical Journal*, 421, 640–650

- Newcombe, M. E., Brett, A., Beckett, J. R., Baker, M. B., Newman, S., Guan, Y., Eiler, J. M., Stolper, E. M. (2017) Solubility of water in lunar basalt at low pH_2O, *Geochimica et Cosmochimica Acta*, 200, 330

- Nishio, T., and Fujiki, Y. (1994) Phase transformation kinetics of precursor gel to α-Alumina, *Journal of materials Science*, 29, 3408–3414

- Nittler, L. R., Alexander, C. M. O'D., Gao, X., Walker, R. M., and Zinner, E. (1997) Stellar sapphires: The properties and origins of presolar Al_2O_3 in meteorites, *The Astrophysical Journal*, 483, 475–495

- Nittler, L. R., Alexander, C. M. O'D., Gallino, R., Hoppe, P., Nguyen, A. N., Standermann, F. J., and Zinner, E. K. (2008) Aluminum-, calcium- and titanium-rich oxide stardust in ordinary chondrite meteorites, *The Astrophysical Journal*, 682, 1450–1478

- Nguyen, A. N., Stadermann, F. J., Zinner, E., Stroud, R. M., Alexander, C. M. O'D., and Nittler, L. R. (2007) Characterization of presolar silicate and oxide grains in primitive carbonaceous chondrites, *The Astrophysical Journal*, 656, 1223–1240

- Nguyen, A. N., Nittler, L. R., Stadermann, F. J., Stroud, R. M., and Alexander, C. M. O'D. (2010) Coordinated analyses of presolar grains in the Allan Hills 77307 and Queen Elizabeth Range 99177 meteorites, *The Astrophysical Journal*, 719, 166–189

- Okamoto, T., and Ida, S. (2022) Monte Carlo simulation of dust particles in a protoplanetary disk: Crystalline to amorphous silicate ratio in comets, *The Astrophysical Journal*, 928, 171

- Ono, S., and Masuo, Y. (2004) Preparation of porous alumina using CO_2 laser firing of amorphous powder synthesized by chemical solution deposition, *Journal of materials Science*, 39, 4367–4369

- Pascucci, I., and Tachibana, S. (2010) The clearing of protoplanetary disks and of the protosolar nebula, *in Protoplanetary Dust*: *Astrophysical and Cosmochemical Perspectives*, Eds. D. Apai and D. S. Lauretta (New York: Cambridge Univ. Press), 263–298

- Prot, D., and Monty, C. (1996) Self-diffusion in α−Al_2O_3. II. Oxygen diffusion in 'undoped' single crystals, *Philosophical Magazine A*, 73, 899–917

- Rafikov, R. R. (2017) Protoplanetary disks as (possibly) viscous disks, *The Astrophysical Journal*, 837, 163

- Rietmeijer, F. J. M., Nuth, J. A., and Mackinnon, D. R. (1986) Analytical electron microscopy of Mg–SiO smokes: A comparison with infrared and XRD studies, *Icarus* 66, 211–222

- Roskosz, M., Gillot, J., Capet, F., Roussel, P., and Leroux, H. (2009) Surface temperature of protoplanetary disks probed by annealing experiments reflecting Spitzer observations, *The Astrophysical Journal*, 707, 174–178

- Roskosz, M., Gillot, J., Capet, F., Roussel, P., and Leroux, H. (2011) A sharp change in the mineralogy of annealed protoplanetary dust at the glass transition temperature, *Astronomy and Astrophysics*, 529, A111

- Sandford, S. A., and Walker, R. M. (1985) Laboratory infrared transmission spectra of individual interplanetary dust particles from 2.5 to 25 microns, *The Astrophysical Journal*, 291, 838–851

- Santos, P. S., Santos, H. P., and Toledo, S. P. (2000) Standard transition aluminas. Electron microscopy studies, *Materials Research*, 3, 104–114

- Scott, E. R. D., and Krot, A. N. (2005) Thermal processing of silicate dust in the solar nebula: Clues from primitive chondrite matrices, *The Astrophysical Journal*, 623, 571–578

- Scotto, E. (2007) Chondrites and the protoplanetary disk, *Annual Review of Earth and Planetary Sciences*, 35, 577–620

- Sieverts, A. (1929) Absorption of gases by metals, *Zeitschrift für Metallkunde*, 21, 37–46

- Signorile, M., Zamirri, L., Tsuchiyama, A., Ugliengo, P., Bonino, F., and Martra, G. (2020) On the surface acid–base properties of amorphous and crystalline Mg_2SiO_4 as probed by adsorbed CO, CO_2, and CD_3CN, *ACS Earth and Space Chemistry*, 4, 345–354

- Sloan, G. C., Kraemer, K. E., Goebel, J. H., and Price, S. D. (2003) Guilt by association: The 13 micron dust emission feature and its correlation to other gas and dust features, *The Astrophysical Journal*, 594, 483–495

- Stroud, R. M, Nittler, L. R., and Alexander, C. M. O'D. (2004) Polymorphism in presolar Al_2O_3 grains from Asymptotic Giant Branch stars, *Science*, 305, 1455–1457

- Takigawa, A., Tachibana, S., Huss, G. R., Nagashima, K., Makide, K., Krot, A. N., and Nagahara, H. (2014) Morphology and crystal structures of solar and presolar Al_2O_3 in unequilibrated ordinary chondrites, *Geochimica et Cosmochimica Acta*, 124, 309–327

- Takigawa, A., Tachibana, S., and Nakagawa, H., and Ozawa, K. (2015) Evaporation and condensation kinetics of corundum: The origin of the 13 μm feature of oxygen-rich AGB stars, *The Astrophysical Journal Supplement Series*, 218, 2–17

- Takigawa, A., Kamizuka, T., Tachibana, S., and Yamamura, I. (2017) Dust formation and wind acceleration around the aluminum oxide-rich AGB star W Hydrae, *Science Advances*, 3, eaao2149

- Takigawa, A., Kim, T., Igami, Y., Umemoto, T., Tsuchiyama, A., Koike, C., Matsuno, J., Watanabe, T. (2019) Formation of transition alumina dust around Asymptotic Giant Branch stars: Condensation experiments using induction thermal plasma system, *The Astrophysical Journal Letters*, 878, L7–L15

- van Boekel, R., Min, M., Leinert, Ch., Waters, L.B.F.M., Richichi, A., Chesneau, O., Dominik, C., Jaffe, W., Dutrey, A., Graser, U., Henning, Th., de Jong, J., Köhler, R., de Koter, A., Lopez, B., Malbet, F., Morel, S., Paresce, F., Perrin, G., Preibisch, Th., Przygodda, F., Schöller, M., and Wittkowski, M. (2004) The building blocks of planets within the 'terrestrial' region of protoplanetary disks, *Nature*, 432, 479

- Walker, R. (1955) Mechanism of material transport during sintering, *Journal of the American Ceramic Society*, 38, 187–197

- Waters, L. B. F. M., Molster, F. J., de Jong, T., Beintema, D. A., Waelkens, C., Boogert, A. C. A., Boxhoorn, D. R., de Graauw, Th., Drapatz, S., Feuchtgruber, H., Genzel, R., Helmich, F. P., Heras, A. M., Huygen, R., Izumiura, H., Justtanont, K., Kester, D. J. M., Kunze, D., Lahuis, F., Lamers, H. J. G. L. M., Leech, K. J., Loup, C., Lutz, D., Morris, P. W., Price, S. D.,

Roelfsema, P. R., Salama, A., Schaeidt, S. G., Tielens, A. G. G. M., Trams, N. R., Valentijn, E. A., Vandenbussche, B., van den Ancker, M. E., van Dishoeck, E. F., van Winckel, H., Wesselius, P. R., and Young, E. T. (1996) Mineralogy of oxygen-rich dust shells, *Astronomy and Astrophysics*, 314, L361–364

- Wilding, M. C., Benmore, C. J., Tangeman, J. A., and Sampath, S. (2004) Evidence of different structures in magnesium silicate liquids: coordination changes in forsterite- to enstatite-composition glasses, *Chemical Geology*, 213, 281–291

- Wilson, S. J., and Mc Connell, J. D. C. (1980) A kinetic study of the system γ-AlOOH/Al_2O_3, *Journal of Solid State Chemistry*, 34, 315–322

- Wing, R. F., and Lockwood, G. W. (1973) The period and spectral range of IK Tauri, *The Astrophysical Journal*, 184, 873–880

- Woitk, P. (2006) Too little radiation pressure on dust in the winds of oxygen-rich AGB stars, *Astronomy and Astrophysics*, 460, L9–L12

- Yamaguchi, O., Omaki, H., Takeoka, K., and Shimizu, K. (1976) Heating properties of boehmite (AlO(OH)) gel prepared by alkoxy-method, *Journal of the Japan Society of Powder and Powder Metallurgy*, 23, 143–148

- Yamamoto, D., and Tachibana, S. (2018) Water vapor pressure dependence of crystallization kinetics of amorphous forsterite, *ACS Earth and Space Chemistry*, 2, 778

- Yamamoto, D., Kuroda, M., Tachibana., S., Sakamoto, N., and Yurimoto, H. (2018) Oxygen isotopic exchange between amorphous silicate and water vapor and its implications for oxygen isotopic evolution in the early Solar System, *The Astrophysical Journal*, 865, 98

- Yamamoto, D., Tachibana, S., Kawasaki, N., and Yurimoto, H. (2020) Survivability of presolar oxygen isotopic signature of amorphous silicate dust in the protosolar disk, *Meteoritics and Planetary Science*, 55, 1281

・ Yamamoto, D., Kawasaki, N., Tachibana, S., Kamibayashi, M., and Yurimoto, H. (2021) An experimental study on oxygen isotope exchange reaction between CAI melt and low-pressure water vapor under simulated Solar nebular conditions, *Geochimica et Cosmochimica Acta*, 314, 108

・ Yamamoto, D., Kawasaki, N., Tachibana, S., Kamibayashi, M., and Yurimoto, H. (2022) Oxygen isotope exchange kinetics between CAI melt and carbon monoxide gas: Implication for CAI formation in the earliest Solar System, *Geochimica et Cosmochimica Acta*, 336, 104